Non-contact temperature measurement method integrated in the rotor of a rotating machine using fiber Bragg gratings

Rita Abboud

Par **Rita ABBOUD**

Méthode de mesure sans contact de la température intégrée au rotor d'une machine électrique tournante au moyen d'une fibre optique à réseaux de Bragg

Thèse présentée en cotutelle pour l'obtention du grade de Docteur de l'UTC

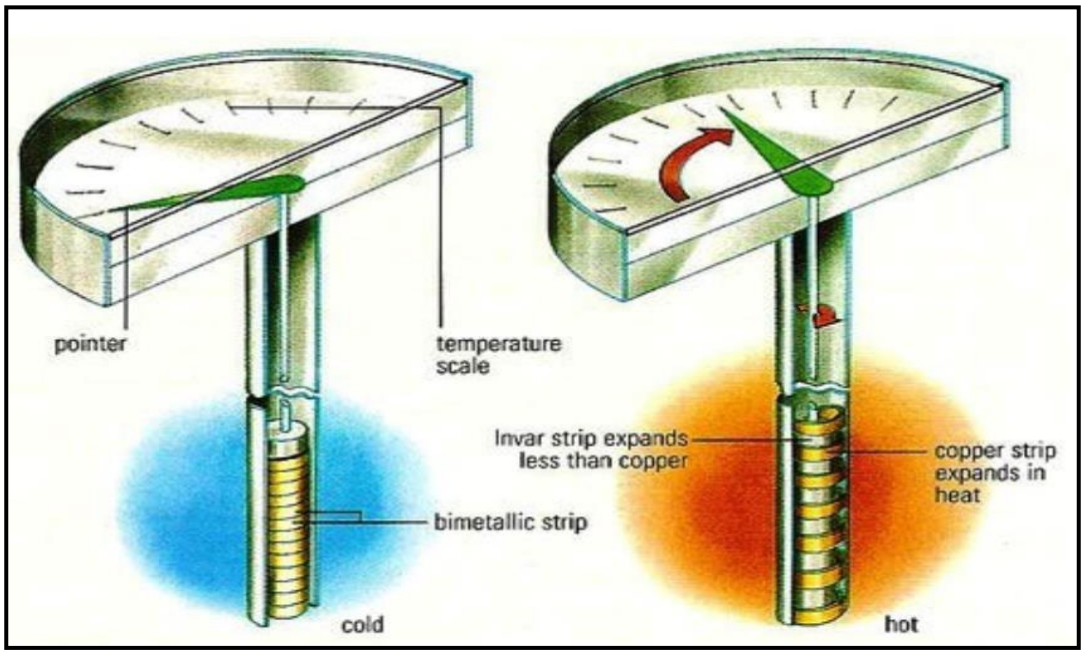

Soutenue le 18 novembre 2021
Spécialité : Mécatronique, Photonique et Systèmes : Unité de recherche en Mécanique - Laboratoire Roberval (FRE UTC - CNRS 2012)
D2645

Méthode de mesure sans contact de la température intégrée au rotor d'une machine électrique tournante au moyen d'une fibre optique à réseaux de Bragg

From the faculty of the Mechanical Engineering of the Université de Technologie de Compiègne at Compiègne, France and The Faculty of Sciences – Lebanese University

Spécialité : Mécatronique, Photonique et Systèmes

Dissertation written by

Rita ABBOUD

Defense date: 18.11.2021

Presented on before the Jury members:

Reviewers:	
Prof. Bruno FRACASSO	IMT Atlantique Bretagne, France
Assoc. Prof. Vinicius SILVA	Institut de télécommunications, Portugal
Examiners:	
Prof. Marie ABBOUD	Université Saint-Joseph, Liban
Prof. Reine TALJ KFOURY	CNRS, Laboratoire Heudiasyc, UTC, France
Asst. Prof. Ali AL ZEIN	Université de Balamand, Liban
PhD Co-supervisors:	
Asst. Prof. Jad ABOU CHAAYA	Université Libanaise, Liban
Asst. Prof. Hani Al HAJJAR (Invited)	Laboratoire Roberval, UTC, France
Asst. Prof. Alejandro OSPINA (Invited)	Laboratoire Roberval, UTC, France
PhD directors:	
Prof. Frédéric LAMARQUE	Laboratoire Roberval, UTC, France
Prof. Youssef ZAATAR	Université Libanaise, Liban

Non-contact temperature measurement method integrated in the rotor of a rotating machine using fiber Bragg gratings

Rita ABBOUD

November 18, 2021

ABSTRACT

In the transportation system domain, heating problems appear with the temperature increase in different types of electrical machines. In the classical design of electrical machines, thermal analysis should be considered in the initial design, control and monitoring of electrical machines. The measurement of local temperature especially in the rotor is important for several reasons such as extending the lifetime of the electrical machine components, and localizing the hot spots inside the machine which allows the development of appropriate cooling systems and protects the machine. Numerous approaches for temperature measurement can be used such as thermocouples, thermistors, infrared sensors or infra-red cameras.

This thesis presents a non-contact technique that measures the temperature of the rotor of a small machine using Fiber Bragg Gratings (FBGs) sensor. Monitoring local temperature especially inside the rotor is important in order to detect early thermal aging of the machine. Hot spot in the rotating parts can be localized by using this technique. The main originality of the proposed work is measuring high temperatures (70°C) with high speed of rotation (860 RPM) of rotating machines and most importantly integrating the FBG sensor into a geometrically small scale electrical rotor of vehicles. The FBG sensor response has been simulated using Transfer matrix method (TMM). After that, the FBG has been calibrated from 20 °C to 70 °C using a heating furnace fabricated at our laboratory. A small rotating machine with embedded FBG has then been designed and fabricated. The temperature of the rotor has been changed while rotating the machine and wavelength shifts due to temperature variations have been experimentally measured up to 860 RPM. A temperature sensitivity of 4.7 pm/°C have been experimentally reached. The ability of this sensor to monitor real time temperature variations of the rotor has been experimentally validated.

Keywords: Fiber Bragg Grating, Dynamical temperature measurement, Rotor, Rotating machine, Optical sensor.

RESUME

Dans le domaine des systèmes de transport, des problèmes de chauffage apparaissent avec l'augmentation de la température dans différents types de machines électriques. Dans la conception classique des machines électriques, l'analyse thermique doit être prise en compte dans la conception initiale, le contrôle et la surveillance des machines électriques. La mesure de la température locale, en particulier dans le rotor, est importante pour plusieurs raisons telles que l'extension de la durée de vie des composants de la machine électrique et la localisation des points chauds à l'intérieur de la machine, ce qui permet de développer des systèmes de refroidissement appropriés et de protéger la machine. De nombreuses approches pour la mesure de la température peuvent être utilisées telles que les thermocouples, les thermistances, les capteurs infrarouges ou les caméras infrarouges.

Cette thèse présente une technique sans contact qui mesure la température du rotor d'une machine tournante en utilisant un capteur à réseaux de Bragg (FBGs). La surveillance de la température locale, en particulier à l'intérieur du rotor, est importante afin de détecter le vieillissement thermique précoce de la machine. Les points chauds dans les parties rotatives peuvent être localisés en utilisant cette technique. L'originalité principale du travail proposé est de mesurer des températures élevées (70°C) avec une vitesse de rotation élevée (860 RPM) des machines tournantes et surtout d'intégrer le capteur FBG dans un rotor électrique de véhicules à petite échelle géométrique. La réponse du capteur FBG a été simulée en utilisant la méthode de la matrice de transfert (TMM). Ensuite, le FBG a été calibré en utilisant un four de chauffage fabriqué dans notre laboratoire et la température a été modifiée de 20 °C à 70 °C. Une machine rotative avec un FBG intégré a ensuite été conçue et fabriquée. La température du rotor a été modifiée pendant la rotation de la machine. Les décalages de longueur d'onde dus aux variations de température ont été mesurés expérimentalement jusqu'à 860 RPM. Une sensibilité à la température de 4.7 pm/°C a été atteinte expérimentalement. La capacité de ce capteur à surveiller les variations de température du rotor en temps réel a été validée expérimentalement.

Mots Clés : Fibre à réseau de Bragg, Mesure dynamique de la température, Rotor, Machine tournante, Capteur optique.

ACKNOWLEDGMENT

My deepest gratitude goes to PhD supervisors, Prof. Frederic Lamarque and Prof. Youssef Zaatar, for having welcomed me in their laboratories and having offered me quality working conditions, both from the point of view of the equipment and the scientific environment. I sincerely thank you for the continuous support on my PhD study and research. Your guidance helps me all the time throughout my PhD journey. I could not have imagined having a better advisor and mentor for my thesis.

I would like to express my sincere thanks to my Co-Supervisors Asst. Prof. Hani Al-Hajjar, Asst. Prof. Alejandro Ospina and Asst. Prof. Jad Abou Chaaya, for their presence and their patience. I would like to express my gratitude for their help and support during these four years. Furthermore, I was able to work with them in an environment of mutual trust, knowing that I would always find an open door to discuss and questions.

I would like to express my sincere thanks to Phillippe Pouille, engineer at the Roberval, for his availability, his considerable technical help and the precious advices he generously gave me throughout this work.

It is my pleasure to express my sincere thanks to all the members of the M2EI group of the Roberval Laboratory Christine, Muneeb, Laurent and Erwan, for their support and their encouragement.

My thanks also go to all the staff members of the Roberval Laboratory at UTC for their immense support during my thesis period, for their collaboration, their help, their advice and their time.

I thank my dear colleagues Simon, Ajynkia, Rachel, Saly, Racha, Santiago, Stéphane, Aurélien, Gabriel, Marcel, Iman, Célien, Xong Yung who welcomed me with open arms and who brought me the necessary moral support to the completion of this work. I was happy to have you guys around for a nice and cheerful environment.

Finally, I owe my deepest gratitude to my family and especially my parents Aline and Khalil and my two sisters Mireille and Nadia for their support and encouragement throughout the years.

TABLE OF CONTENTS

LIST OF FIGURES

LIST OF TABLES

LIST OF ABBREVIATIONS

CAD	Computer Aided Design
CMT	Coupled Mode Theory
CMEs	Coupled Mode Equations
CCD	Charged Coupled Device
DC	Direct Current
FBGs	Fiber Bragg Gratings
FOS	Fiber Optic Sensor
FWHM	Full Width at Half Maximum
IEA	International Electrical Agency
EMI	Electromagnetic Interference
IR	Infrared
IC	Integrated Circuit
FOCS	Fiber Optic Current sensors
NTC	Negative Temperature Coefficient
PT100	Platinum with a value of 100 Ohms
PTC	Positive Temperature Coefficient
PMMA	PolyMethyl Methacrylate
POF	Plastic Fiber Optic
POFBG	Plastic Optical Fiber Bragg Grating
RMS	Root Mean Square
RTDs	Resistive Temperature Devices
SAW	Surface Acoustic Wave
SLD	Super-luminescent Diode
TC	Thermocouple
TOC	Thermo-optic coefficient
TEC	Thermal expansion coefficients
TDM	Time Division Multiplexing
TMM	Transfer Matrix Method
UTC	Université de Technologie de Compiègne
UV	Ultraviolet
WDM	Wavelength Division Multiplexing

INTRODUCTION

The global warming is due to the high consumption of primary sources of energy [1]. One of the primary sources of energy is the petroleum source. In the next decades, the primary sources of energy will be replaced progressively by secondary renewable sources of energy produced by solar cells, wind or marine turbines. This is called the energy transition. The consumption of petroleum energy is very high in many fields especially in the transportation systems. Therefore, in automotive industry, energy transition from petrol powered engines to performing electrical machines is required. In fact, the energy transition involves a very strong use of electrical machines. According to the IEA source [2], electrical motors represent between 43 and 46 percent of all global electricity consumption. Renewable energies will grow and new electrical systems will arrive. Hence, the use of these machines will only increase. In this new era, electrical machines occupy a main position. This change in primary source of energy (oil to electric) will be accompanied by the integration of new smart electrical systems that are efficient and compact. Additionally, their integration in mechanical systems involves the consideration of constraints and mechanically complex environments. In this type of environment, the motor and its control system must be chosen to obtain high power, while limiting the size of the system (compactness). Better performances of electrical components are required since the electrification will widely attack a lot of systems inside the vehicle such as on board computers. Therefore, the temperature of these components should be monitored due to the heating problems.

In automotive industry, electrical machines will be strongly used in the next decades. In this new era, the integration of rotating electrical machines and compact electrical systems into mechanical systems leads to the problems of hot temperature spots and thermal evacuation. The rotating parts in mechanical systems, such as the rotor of electrical machine are important elements in high-power as well as low-power electrical systems. These rotating parts are subjected to failures due to hot temperature spots and overheating problems. In the transportation system domain, the loss of magnetization appears in permanent magnet machines and the electrical insulators and the magnetic materials heating problems appear with the temperature increase in the other types of machines. Under these conditions, thermal analysis, considered secondary and approached indirectly for a long time, becomes crucial in the design and diagnosis of electrical machines.

Thermal stresses of rotary components become one of the main design criteria in many industries. In fact, they play a factor of competitiveness in the construction of machines in terms of minimal use of the materials. Therefore, it is of high importance to localize the hot spots in these machines especially in the rotating parts. Temperature monitoring of electrical machines can have a direct influence on the lifetime of its components (insulators of conductors, magnets, etc.), namely by allowing access to predictive information. It also protects the machine by stopping its operation due to a heat peak. Besides, localizing the hot spots inside the machine will allow the development of appropriate cooling systems. A mapping of the temperature inside an electrical machine can also give information on

different losses (rotor and stator) and help to improve the energy efficiency of the electrical motors and generators at the same time, as well as optimizing their control (identification of the variation of the parameters as a function of the temperature). Therefore, the mapmaking of the temperature can allow rapid monitoring and diagnosis techniques. However, getting temperature information of some critical locations of rotating components is difficult because these locations are not accessible to ordinary sensors, which must be attached to the surface. Adding sensors to the rotor of the electrical machine is not yet commercialized because of their difficult instrumentation and integration on the rotating part which give poor reliability. Nevertheless, temperature monitoring can avoid the destruction of the conductors and insulating materials of the electrical machine. Therefore, it is truly important to detect the thermal degradation problems of the rotor to avoid the end of life of the electrical machine.

Optical fiber sensors are regularly used for measuring temperature, pressure, stress or other physical quantities, especially where the fiber is close to the measurement area and where the systems of transmission, reception and data processing are deported [3]. Moreover, they are used for monitoring internal system parameters in operation following the position of fibred probes in certain areas during manufacture or assembly. Fiber Bragg grating sensor allows local or distributed measurements on the area of interest and it is developed by exploiting the different components of a signal passing through the fiber such as intensity, wavelength, frequency or phase [4]. It has the following properties: immunity to electromagnetic interference (EMI), low weight for easy integration and ability to resist harsh environments [5]. Moreover, it has the advantage of decreasing the number of copper wires. FBGs have gained a strong interest among researchers due to their numerous applications and many highly active fields such as biomedical sensing, respiration monitoring, structural health monitoring, civil engineering, aeronautics, railways systems and nuclear environments [6],[7],[8],[9]. Therefore, using FBG sensors is a good solution to monitor rotors during their operation in order to detect early thermal aging of electrical machines.

Among the work that has been published on this subject, relatively few of them deal with the so called distributed FBG sensors taking into account temperature monitoring in electrical machines. The use of thermal mappings of electrical machines, obtained by direct measurement, can allow a rapid monitoring and diagnosis technique. This technique is still poorly exploited compared to methods conventionally used in mechanics (vibratory signatures and acoustic emissions). In particular, rotor temperature mapping can provide a robust temperature monitoring system to diagnose and predict the behavior of the parameters that are critical to ensure the proper functioning of the machines.

The originality of this work, in comparison to other methods, will be the non-contact measurement of temperature of the rotor by using an FBG sensor integrated into a geometrically small scale rotating system. The other originality will be the measurement of high temperatures (~ 70°C) with high speed of rotation (> 800 RPM) of rotating machines. Furthermore, there are less limitations on rotational speed because no contact exists between the rotary and the stationary part.

From the literature survey as presented in Chapter 1 it follows: no existing work has been done integrating FBGs in rotating parts of rotating machines for temperature measurements. No existing work has yet taken into account the problem of temperature

measurement inside the rotor of the electrical machine. The existing solutions measure temperature on stationary parts.

In this project, we are going to propose the use of FBG for measuring temperature in of the rotor of a rotating machine during its operation. This will give an accurate idea of the temperature value in real time at different rotor locations unlike what currently exists by measuring the average value of the temperature using a thermal camera or other similar technique. Moreover, this solution will extend the life of a rotating electrical machine which may fail due to a localized heat spike during operation. Besides, it will optimize the energy consumption of a rotating machine which performance fall due to an increase in its temperature in one or more places of the rotor.

Consequently, this thesis presents two major challenges: the first is the temperature measurement, which is difficult to setup because of the rotation of the mechanical parts and the second is the positioning of sensors inside the rotating machine.

In this context, this study was born from the collaboration between the Lebanese University and the University of Technology of Compiègne with a main thesis objective which is the development of an innovative and relatively low cost detection technique that visualize the variations of the rotor temperature of rotating machines.

The thesis is organized into four chapters and the contents of each chapter are briefly described as follow:

In the introduction the background of the topic is introduced, the overall importance of the main problem is identified, our research goals and approaches are defined and a summary on the organization of the report is included.

In Chapter 1, temperature sensors are first reviewed. Then, literature review of the temperature measurement techniques in the electrical machines is done followed by review of different methods for measuring temperature using FBG sensors in electrical machines. The state of the art of the FBG interrogation techniques is also presented.

After the literature review in Chapter 1, the theory of FBGs is presented in Chapter 2. This chapter will explain sufficient fundamental background information about the FBGs theory to support our objectives. In addition, modelling and simulation will be carried out to study the effect of external changes on FBG in order to compare them with the experimental work. Then, the simulation of the FBG reflection spectrum will be realized. The simulation of the temperature response of the FBG, as well as the longitudinal and local transverse strain sensing will be carried out.

In chapter 3, the experimental characterization and calibration of the static FBG temperature sensor is described. The principle of functioning of the main optical components forming our experimental system will be detailed. The thermal characterization of the FBG measurement system will be discussed and the calibration method will be detailed. Finally, the relationship between the measured wavelength and the temperature will be established and the optical performances of the sensor will be analyzed.

Chapter 4 is dedicated to the method of the dynamical temperature measurement in the rotating machine. Further, the concept demonstration of the realized design is explained. The mechanical system architecture including the rotating machine design and fabrication

and the rotor instrumentation are detailed. Finally, the prototype is validated and the rotor temperature is calculated.

The manuscript closes with a summary of the work and the results of the research. An evaluation is included where limitations are being discussed. In addition, perspectives are also given on opportunities for expanding the work done in this thesis to improve the results of this research and the remaining questions to be answered.

CHAPTER 1

LITERATURE REVIEW ON FBG TEMPERATURE SENSORS AND ITS APPLICATION IN THE ELECTRICAL MACHINE DOMAIN

1.1 INTRODUCTION

The development of low loss optical fibers based sensors started in the early 1970s. Since then, a range of optical fiber based sensors have been developed and the field of optical fiber based sensor has seen a continuous progress [3]. Fiber optic sensor is defined as a sensor that uses optical fiber either as the sensing element or as an element that relays signals from a remote sensor to a processing electronic unit. In the 1970, optical devices were very expensive. However, during the 1980's, optoelectronic devices became less expensive and used in optical fiber sensors (OFS). Optical fiber sensors are applied in fields, such as the electrical power industry as well as many other branches. They are used to monitor some important physical parameters such as strain, vibration, temperature, pressure and others [10].

In electrical power industry, the presence of high voltage and electromagnetic interference are two main obstacles for using electronic sensors. The use of optical fiber sensor in the electrical power industry is a good option instead of the use of an electronic sensor [11]. It is safe to place them close to high voltages potentials and there is no need for electric energy to power them [12].

There are many types of optical fiber sensors. At the beginning of optical fiber sensors era, the light amplitude based sensors were very common. They depend on losses due to connectors, macro bends or laser/LED drifts [13]. However, they were gradually substituted by wavelength based sensors, which are more stable. The advantages of the FBG sensors offer over other types of OFS sensors are the main reasons that drives research in optical fiber sensors for a wide range of applications. For example, they are small sized and lightweight. They can be used for remote sensing because no electrical power is needed at the desired location. They are in general minimally invasive and can be multiplexed on a single fiber optic network, which allows sensing in multiple points [14]. They are also intrinsically passive and immune to electromagnetic interference and most of all they can be used in places where there is high explosive atmosphere areas or electric fields since they do not need nor conduct electrical power [5].

This chapter gives a general introduction on temperature sensors and a summarized description of optical fibers based sensor technologies, their characteristics and their classification.

A literature review of the different techniques for measuring temperature in the electrical machines is provided. Special emphasis is on a very special type of OFS, which are Fiber Bragg Gratings sensor (FBGs) and the advantages of using FBGs will be discussed. Then a review of different methods for measuring temperature using FBG sensors in the rotor of the electrical machines proposed in the literature are presented.

Finally, the state of the art of the interrogation techniques using FBG and FBG interrogators providers are summarized before concluding the chapter.

1.2 TEMPERATURE SENSORS

The tremendous advances in electrical engineering in the past century led to the capability of transforming a wide range of measurand into electrical signals. The temperature sensor is a physical device or transducer which is capable of transforming the temperature into an electrical signal, no matter how tiny the amount of this signal might be [15].

In different branches of the industry, it's required to know the temperature of the environment, inside a reactor (chemical, nuclear, gas), the winding of an electrical machine and so on. Different technologies have been invented to do this for different applications. There are two different types of industrial temperature measurement system. The first one is the mechanical temperature measurement system and the second one is the electrical temperature measurement system.

In the mechanical temperature measurement such as bimetallic temperature gauge, gas filled temperature gauge, bimetallic thermometer, compensated thermometer, gas filled thermometer etc., the physical aspects such as the time and the temperature are directly proportional to the change in length or in structure that can be expansion or contraction [16]. However, in the electrical temperature measurement such as Resistive Temperature devices, thermocouples, etc., we have to deal with some of the electrical parameters such as the change in resistance or conductance (RTDs) or Seebeck effect (thermocouples).

There are different ways to measure temperature: traditional contact thermometers or non-contact techniques such as infrared thermometers and thermal images.

Some of the contact temperature measuring devices have a lot of functionality. They could have multiple input channels, display multiple information and trend readings over time. The contact type temperature instruments have the disadvantage of the necessity of making contact in order to take a reading. However, sometimes there is areas where getting close to a certain region to measure its temperature is very difficult. Therefore, these devices potentially pose certain challenges in these cases and that's where the non-contact IR-thermometers come into play.

The alternative is non-contact temperature sensing in order to monitor the temperature of objects. The main disadvantage of the non-contact IR thermometer, is that the place where to take a reading and what the target is should be known. However, the thermal camera gives the ability to get a quick understanding of where are the potential heat sources that can cause damages to an electrical machine or a mechatronic system.

The basic types of temperature measurement sensors discussed here are the non-contact type such as bimetallic devices, pyrometers, thermal camera, surface acoustic wave and the contact type like resistive temperature devices (RTDs, thermistors), thermocouples, and semiconductor based sensors.

1.2.1 Bimetallic Devices

Bimetallic devices expand when they are heated. In these devices, two metals are bonded together and mechanically linked to a pointer. When heated, one side of the bimetallic strip will expand more than the other as shown in Figure 1 [17]. When geared properly to a pointer, the temperature measurement is indicated.

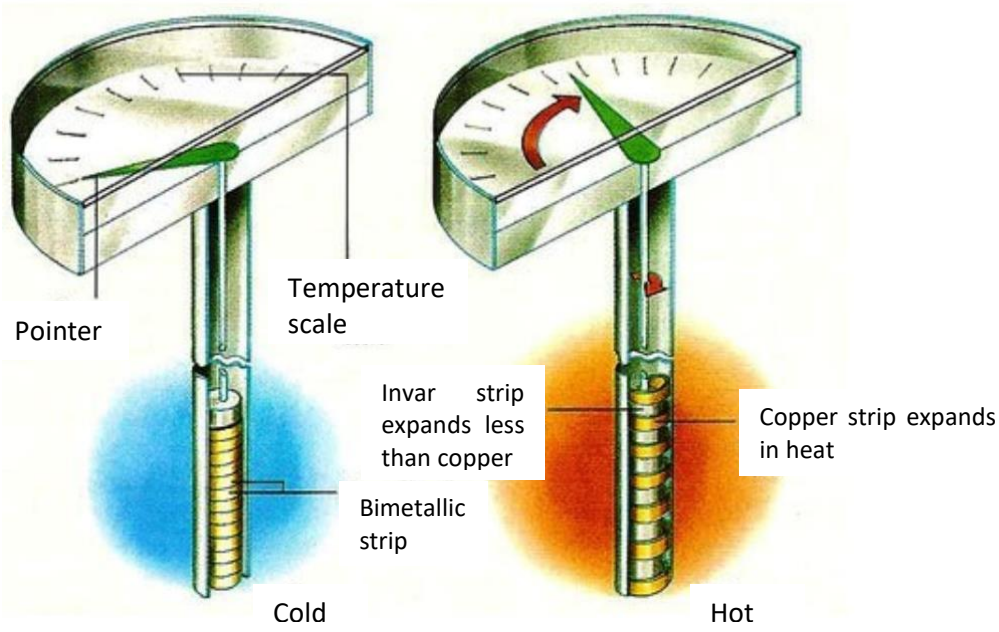

Figure 1: Principle of temperature measurement using bimetallic device

The definite advantages of bimetallic devices are the portability and their independence from a power supply when used for the right application. However, they are not usually as accurate as electrical devices and recording the temperature value is not easy as with electrical devices like thermocouples or RTDs.

1.2.2 Non-contact IR-thermometers

Infrared sensors are non-contacting sensors. As an example, infrared sensor will give the temperature of the object by utilizing the radiation of its material without any contact, as indicated in Figure 2 [18]. A non-contact infrared thermometer is useful for measuring temperature under circumstances where thermocouples or other contact probe-type sensors cannot be used or do not produce accurate data. Some typical circumstances are where the object to be measured is moving, surrounded by an electromagnetic field, contained in a vacuum or other controlled atmosphere or in applications where a fast response is required [19]. In addition, non-contact sensors are used in conditions where the contact with the

sensor would damage or introduce a significant temperature gradient on the surface of the object or the temperature of the object is higher than the maximal recommended working temperature of the contact sensor [20].

Infrared thermometers can be used to serve a wide variety of temperature monitoring functions. Some examples are monitoring materials for heating or cooling processes, checking the temperature and hot spots for mechanical or electrical equipment, checking heater or furnace temperature for calibration and control, checking for hot spots in fire-fighting [21].

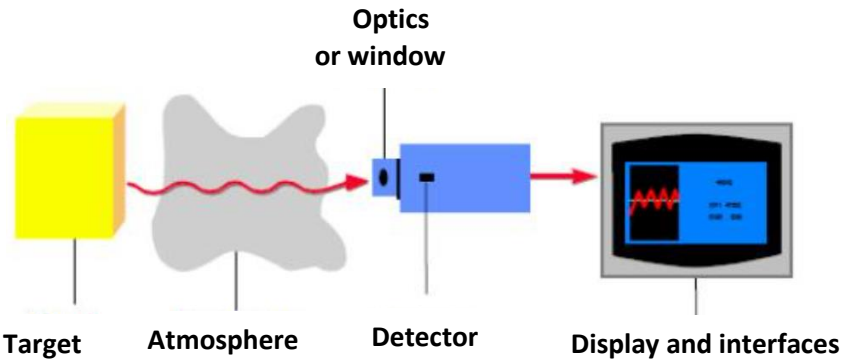

Figure 2: A typical IR temperature sensor consists of optical components, IR detector, electronic and a display output stage

The non-contact IR-thermometers can take a temperature reading from remote location. A laser beam can target the area of interest. They have a certain range in temperature and working distance. They also have a distance to spot that have to be taken into account: the larger the remote distance and potentially the less accurate the reading is going to be. Some of the more expensive IR thermometers, will give the ability to select the emissivity, which is a setting that allows the thermometer to take accurate readings on different types of surfaces [22].

The spot infrared pyrometer or infrared pyrometer is the most common infrared thermometer. It measures the temperature at a spot on a surface that is a relatively small area. A visible red dot is projected onto the center of the area being measured, which identifies the measuring location as shown in Figure 3 [23].

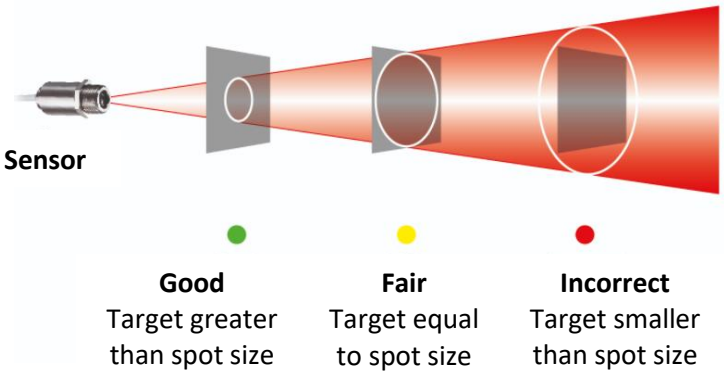

Figure 3: Measurement of spot diameter

The pyrometer is a non-contact small Infrared thermometer and is suitable for measuring extreme hot temperature. It measures accurately the temperature range from -18 °C to 870 °C [22]. It provides high accuracy with a fast response time.

Some pyrometers are equipped with dual laser beam for high performance industrial application and can measure temperature from greater distance. Applications could be in the food and beverage industry, carpet manufacturing, glass and automotive industries [24].

Pyrometers are used for two main reasons taking in consideration important factors. First, thermocouples are not sufficient because they are not accurate enough or the object that they're measuring is moving or rotating and they just can't make physical contact with that. As well as, in order to increase the overall measurement accuracy of any material that is being heated in terms of better product quality, better yield or better throughput.

1.2.3 Thermal camera

Infrared cameras or infrared thermal imaging cameras are essentially infrared radiation thermometers. They measure the temperature at different points over a large area to generate a two-dimensional image. Each pixel of the thermal image represents a temperature location. This technology is used for monitoring large areas. Infrared thermal imaging cameras are used in many applications such as military or security personnel (perimeter monitoring), process quality monitoring of manufacturing processes and equipment, monitoring enclosed space hot or cold spot for safety maintenance purposes [25]. A visual IR thermometer provides a visual representation and a heat map of the measured object.

This IR thermometer combines the ability to overlay a normal digital visual representation with the heat map as seen in Figure 4 [26] [27]. Therefore, a better understanding of the target area is achieved. In a thermal camera a thermal image has a high resolution, a large field of view and a good sensitivity to temperature in its field of view. It allows to diagnose problems which might not be detected by a low resolution thermal camera. It is able to detect hot spot from a component inside an object.

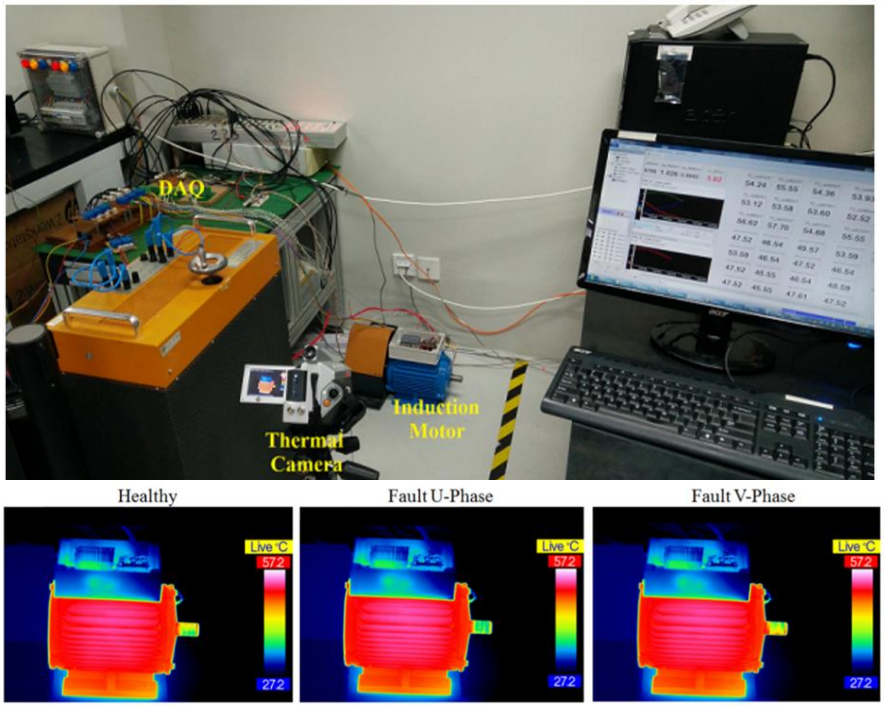

Figure 4: IR camera working principle

1.2.4 Surface acoustic wave sensor SAW sensors

The Surface Acoustic Wave (SAW) sensor is known since several years as a sensing element for different physical parameters such as temperature, pressure and force. Surface Acoustic Wave (SAW) devices are used as resonators and filters for high frequencies in electronic circuits since many years. Sensing elements based on SAW devices are used because of the dependencies of the surface acoustic wave to the environmental influences.

For SAW based temperature sensing the operation shown in Figure 5 is as follow: First, an electromagnetic impulse signal is sent via wired connection or wireless antenna to the device. Then, the interdigital transducer (IDT) transduces the electromagnetic signal into a surface acoustic wave. The surface acoustic wave (SAW) propagates along the surface of the substrate into a piezoelectric material. After that, the acoustic impulse response wave is transduced back into an electromagnetic signal (influenced by the temperature to which the sensing element is exposed). The electromagnetic response signal is then transmitted for processing [28].

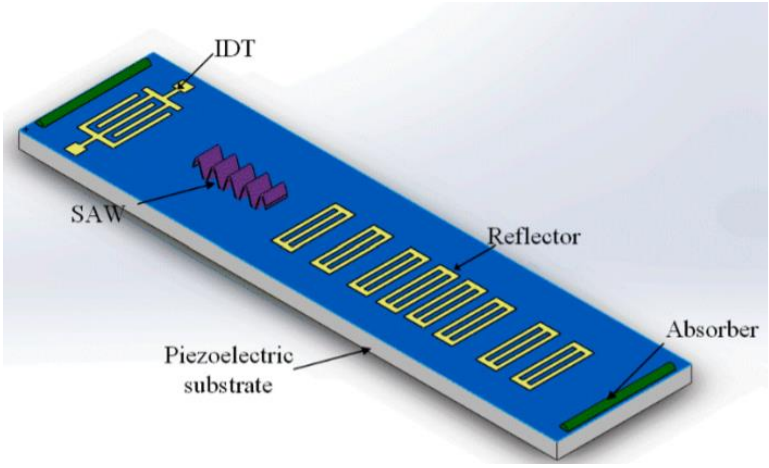

Figure 5: Schematic of a typical SAW device

The advantages of the SAW sensors are as follow: SAW sensors can handle high frequencies, therefore, the sensor signal can be transmitted wirelessly. The physical parameters are converted into a change in frequency, delay or phase. In addition, the Surface Acoustic Wave sensor is a wireless passive sensor. Therefore, no need to cables, batteries or maintenance and continuous monitoring. It has a small design and dimensions that enables applications on rotating parts. There is no need for electronic components because the change of the substrate where the SAW is propagating along is responsible of the conversion from the physical parameter to the signal response of the sensor. Therefore, SAW sensors can be used in hot and aggressive environments because there are no restrictions on the maximum temperature.

The SAW sensor can be used in rotating equipment monitoring, real time temperature monitoring, operates in motion up to 5000 RPM for applications such as temperature, pressure, or strain/torque measurements [29]. In addition, it can be used in remote control electrical equipment, switchgear wind turbine generator monitoring, bearing temperature control, wireless temperature control on rotating parts, automation, production line monitoring [30].

1.2.5 Resistive temperature sensors

Resistive temperature measuring devices also are electrical [31]. They take advantage of a characteristic of matter which is the resistance that changes with temperature, rather than using a voltage as the thermocouple does. The two types of resistive devices are metallic resistive temperature devices (RTDs) and thermistors.

1.2.5.1 Resistance Temperature Detector (RTD)

In general, RTDs are more linear than thermocouples. They increase in a positive direction, with resistance going up as temperature rises [32]. There are different temperature transducer technologies. The resistance of this device varies with the temperature. It is a passive device that needs external current (or voltage) source. An external electrical current should be applied to it and then the voltage drop across it can be measured. This voltage is an indication of the temperature. However, a big amount of external current can cause power

dissipation in the resistor of RTD and lead to excess heat. In order to avoid this type of error, the current should be kept at a minimum level, in general it is 1 mA.

They are used in a two-wire configuration. More accurate reading comes in three-wire or four-wire configurations. Three-wire and four-wire solutions are developed to remove some measurement errors coming from cables. In the circuit, the change of resistance is converted into the change of output voltage as shown in Figure 6 [33].

Figure 6: Resistance Temperature Detector scheme

In the industry, different RTD types are suitable for various applications. One of the most common RTDs is PT100 which consists of a thin film of Platinum on a plastic film and shows a resistance of 100 Ω at 0 °C.

Platinum is usually used because it is retardant to corrosion. Its resistance varies with temperature and it can typically measure temperatures from -165 °C to +848 °C. The relationship between resistance and temperature of PT100 is relatively linear over a wide operating range as seen in Figure 7 [34]. RTDs have very good accuracy. However, they have a relatively low sensitivity.

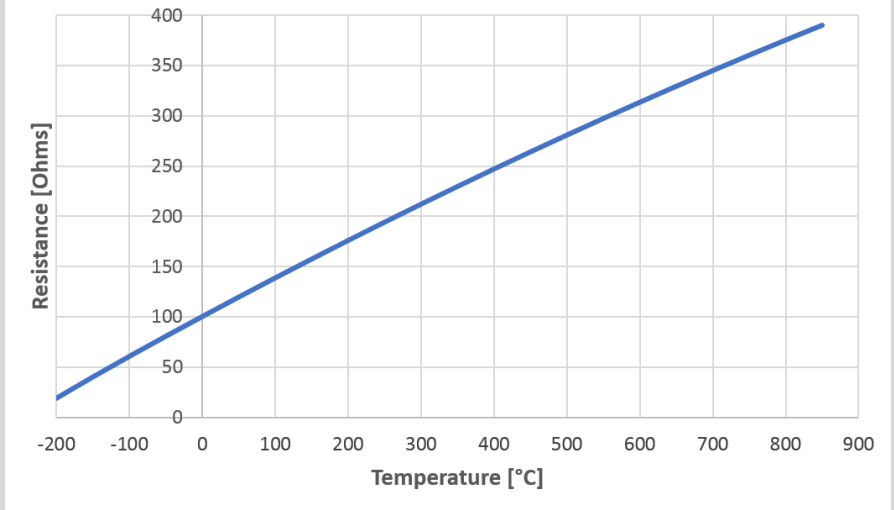

Figure 7: Relationship between the electrical resistance and the temperature of a Pt100

1.2.5.2 Thermistors

Thermistors are temperature dependent resistors. Thermistors have a temperature stability up to 300 °C. The self-heating effect in thermistors is great because of the reduced size that decreases the heat dissipation capability. On the other hand, the thermistor is an extremely nonlinear semi-conductive device. The thermistor operates usually as an alarm that switches when the temperature exceeds a certain limit as shown in Figure 8 [35].

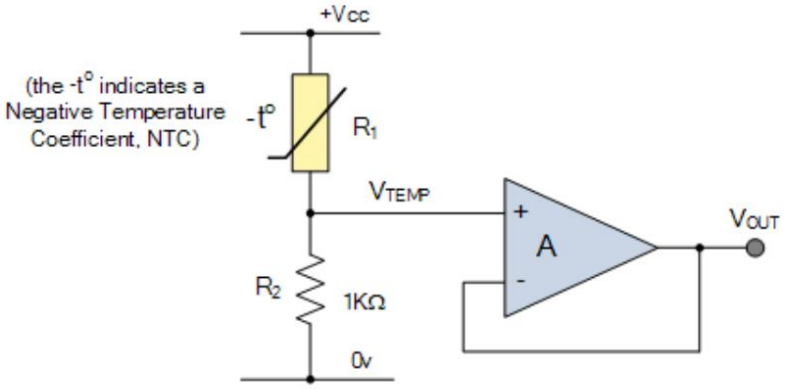

Figure 8: Thermistor used in an electrical circuit

They are widely used in industrial purposes, such as self-regulating heating elements, over-current protection, inrush current limiters and so on [36]. Thermistors can have Negative Temperature Coefficient (NTC) or positive Temperature Coefficient (PTC) as seen in Figure 9 [37].

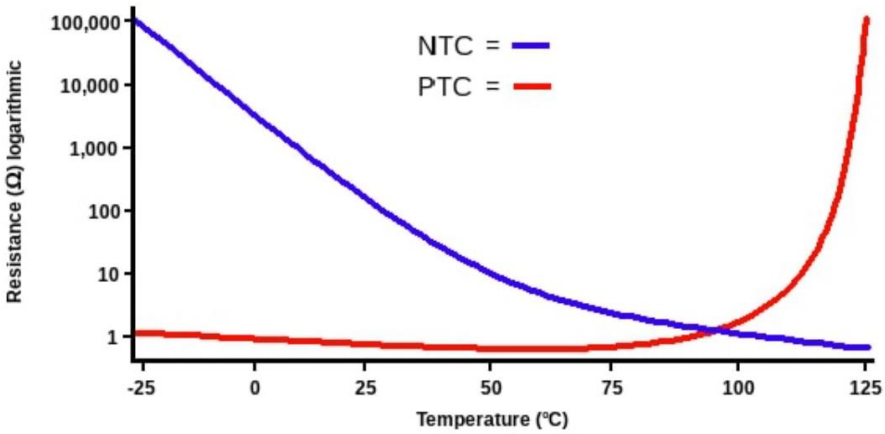

Figure 9: Relationship between the resistance and the temperature of a thermistor

In NTC thermistors, the resistance decreases as the temperature rises. NTC thermistors are commonly used as inrush current limiters. However, with PTC thermistors, the resistance increases as the temperature increases. PTC thermistors are commonly used as overcurrent protection and in resettable fuses. Thermistors have a very sensitive response.

They also have the advantage of high stability, fast response and small physical size. Thermistors devices have low cost.

1.2.5.3 Semi-conductor

Semi-conductor temperature transducers have found more applications in the form of integrated circuits, in recent years [38]. The semiconductor diodes (p–n junctions) have temperature sensitive voltage-current characteristics as shown in Figure 10 [39].

Transistors in the integrated circuit produce an output current or voltage that is

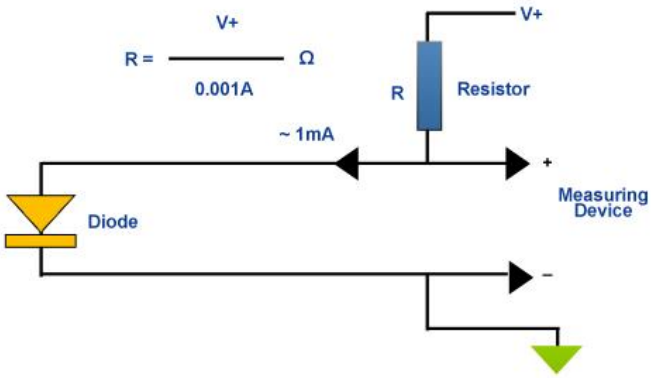

Figure 10: Semi-conductor diode as a temperature sensor

proportional to the absolute temperature by using external power supply and internal feedback mechanisms. This technology is vastly used in electronic devices and IC technologies [32]. The advantages of this technology are its linear characteristic, low cost and small size. Integrated circuit temperature sensors are suitable for specific applications where the temperature is within a −40 °C to 120 °C range.

1.2.6 Thermocouples

Thermocouples can measure temperature based on the Seebeck effect. The physical dimensions of the junction's materials and the working temperature determine the working life of thermocouples. Copper/constantan (T type) and chromel/alumel (K type) are most widely used in electrical machine condition monitoring and can survive for many years. A good quality of the signal conversion circuit leads to a better performance of the transduction. However, it is relatively expensive. Different types of thermocouples are available, for example E, J, K, T and so on, based on the range of temperature measurement and the sensitivity.

In general, the thermocouple is located inside a metal or ceramic shield, which protects from exposure to a variety of environments. Metal sheathed thermocouples also have outer coatings, such as Teflon for more protection when used in acids or strong caustic solutions [40]. A thermocouple (TC) is comprised of a couple of specific dissimilar wires joined together, forming the junction or the sensing point [41]. When this junction is placed at different temperatures, different millivolt signals are generated. This can be interpreted as an

indication of the temperature, which based on the physical characteristics called thermoelectric effect as seen in Figure 11 [42].

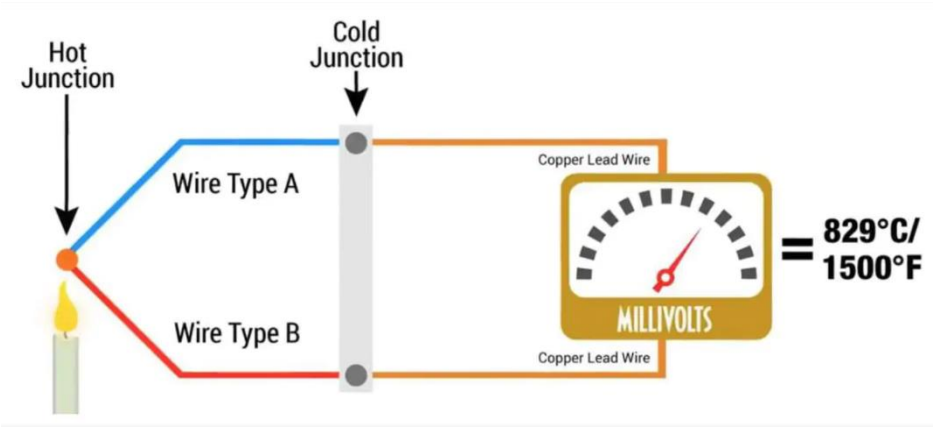

Figure 11: Thermocouple temperature measurement

Thermocouples indicate temperature measurement with a change in voltage. They are voltage devices in which when temperature goes up, the output voltage of the thermocouple rises as indicated in Figure 12 [43].

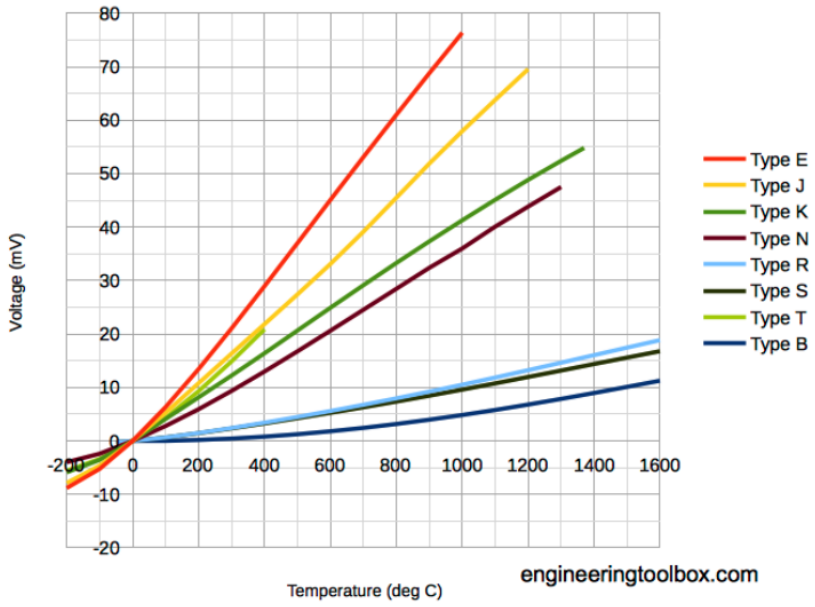

Figure 12: Voltage difference versus temperature characteristic curve of a thermocouple

Thermocouples are self-powered and do not require external excitation current source, in comparison with RTDs. They are commonly used for furnaces, high-temperature exhaust ducts, Gas Turbine combustion chamber, etc. The main restriction of the thermocouples is their accuracy, which does not make it the best solution for precise applications. Also, they need a reference measurement point called the cold junction. For

instance, type J is made up of Iron-Constantan combination with a -4 °C to 748 °C operating range and sensitivity of approximately 27.8 µV/°C. Type K is made up of Chromel-Alumel combination is one of the most common general purpose thermocouples with a sensitivity of about 22.8 µV/°C with a range of -165 °C to 1348 °C. Type K is inexpensive and a wide variety of probes are available in its range.

The electrical industry has relied on the use of thermocouples, thermistors, infrared cameras. However, their usefulness is limited because they are installed on fixed parts. The main problems are difficult installation, heavy weight, low signal to noise ratio, etc. In addition, electrical noise can corrupt the collected data. However, it is difficult to obtain temperature information from certain critical areas of rotating components because these areas are not accessible to ordinary sensors, which must be attached to the surface.

1.2.7 Fiber optic sensors

The core radius and the indices of a single mode fiber optic allows one mode at a given wavelength to propagate along the fiber. The core diameter is small in a single mode fiber compared to multimode fiber. In single mode fibers, the light travels along its axis, which eliminates intermodal dispersion. Light is not totally confined into the core; an important part is found in the cladding [45]. The low optical loss in optical fiber for communication is due to material properties. Germanium and silicon are among the most used core dopants. These materials constitute a limit to the attenuation characteristics of the waveguide. However, the presence of impurities causes significant absorption loss [46].

1.2.7.1 Fiber optic sensor classification

Fiber optic sensor are classified as intrinsic or extrinsic, which depends on how the optical fiber is used in the sensing scheme. An intrinsic sensor is a sensor that uses an optical fiber as the sensing element as indicated in Figure 13.

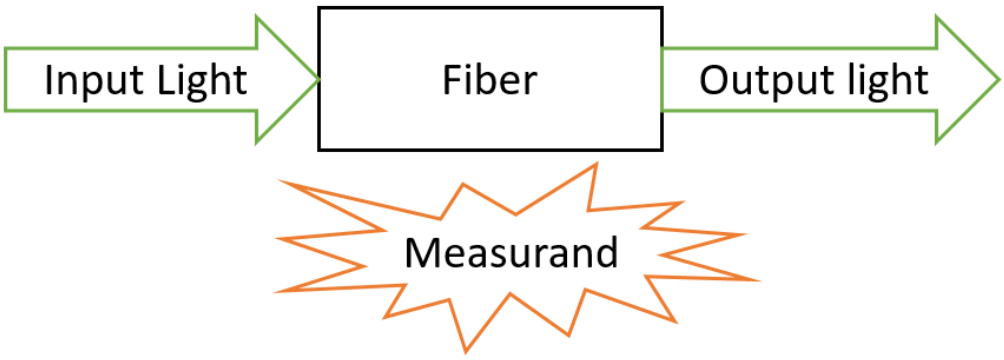

Figure 13: Intrinsic fiber optic sensor

The interaction between the light and the quantity to be measured occurs into the fiber optic sensor. Optical fiber sensors can mainly measure strain, temperature and pressure. The measurand modulates the intensity, phase, wavelength or polarization of the light that

propagates into the fiber. When the FOS is intrinsic it can be classified into two categories: a direct or indirect sensor. In a direct sensor, the measurand influences the fiber itself. For instance, a fiber optic current (FOCS) measures uni or bidirectional DC currents up to 600 KA by using a single-ended fiber optic around the current conductor that utilizes the Faraday effect [47].

However, when the measurand can be locally transduced to another quantity, then this quantity influences the optical fiber the sensor is called an indirect sensor. In extrinsic fiber optic sensors optical fiber cables are used to transmit modulated light from source to detector but modulation occurs outside the optical fiber transducer. In this case, the interaction between the measurand and the light takes place outside of the fiber optic as shown in Figure 14.

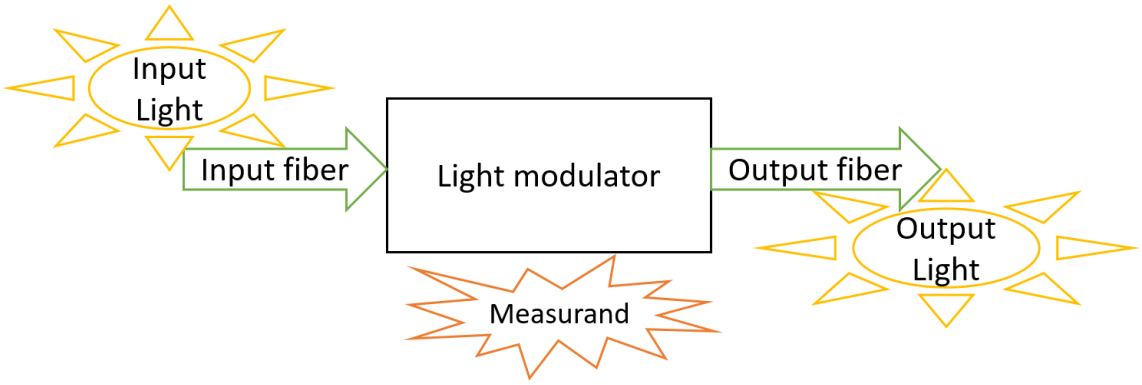

Figure 14: Extrinsic fiber optic sensor

In this work, an intrinsic sensor fiber is used for temperature measurement. The variations in temperature will induce a change in the wavelength of the light and by measuring the changes in wavelength, temperature variations would be measured. This principle will be detailed later on.

For a proof of concept in our thesis work, fiber Bragg grating will be used as a point sensor. Temperature variations measurement will be first measured at a specified point of the fiber. This will enable us to determine the sensitivity and check with the specifications. In the next section, we will explain the fabrication methods of FBGs and the advantages of using these optical fibers.

1.2.7.2 FBG fabrication methods and types of FBG

In 1978, the photosensitivity of optical fiber was discovered by Kenneth O. Hill et al [48]. The fiber photosensitivity is the capability of a fiber to locally change its refractive index when it is irradiated by a UV light. Spatially irradiating a fiber leads to a periodic variation of the refractive index, which allows the realization of FBG. The photosensitivity depends on several factors such as the irradiation source, the fiber core composition, the technique and condition of manufacturing of the fiber before the irradiation.

Different methods exist for writing gratings into the core of the optical fiber. There are few externally written fabrication techniques such as the phase mask technique [49][50], interferometric technique [51][52], on-tower FBG inscription [53] and the point-by-point technique [54]. The grating is obtained by illuminating the fiber core using a UV light, which altered locally the properties of the material of the fiber.

In the phase mask technique, the interference pattern along the core of the fiber is created by the ±1 diffraction order of the UV light. The grating is written into the fiber core by the periodic fringe pattern. The corresponding scheme is depicted in Figure 15 [49].

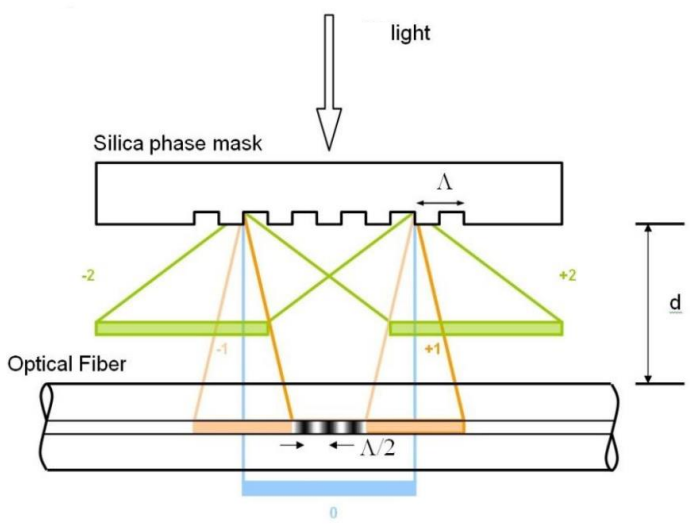

Figure 15: Schematic of the phase mask technique

The grating period Λ_{pm} depends on the pattern of the fringes. The fringe pattern is determined by the angle of diffraction Ø and the wavelength of the light λ_{UV} [50]:

$$\Lambda_{pm} = \lambda_{UV}\sin(Ø) \tag{1-1}$$

The phase mask is a robust and simple technique. Long writing times are achieved because the setup is stable. One limitation of this system is that for a given mask, the Bragg wavelength is fixed. In addition, the phase mask can be easily damaged because they are very fragile.

The main advantage of the interferometric technique [51][52] is that the Bragg wavelength can be changed. In addition, few components are necessary. This system shown in Figure 16 is less sensitive to alignment errors and vibrations because of the small difference between the two arms of the interferometer. One disadvantage is the limited coherence length because the half of the beam is folded on the other half.

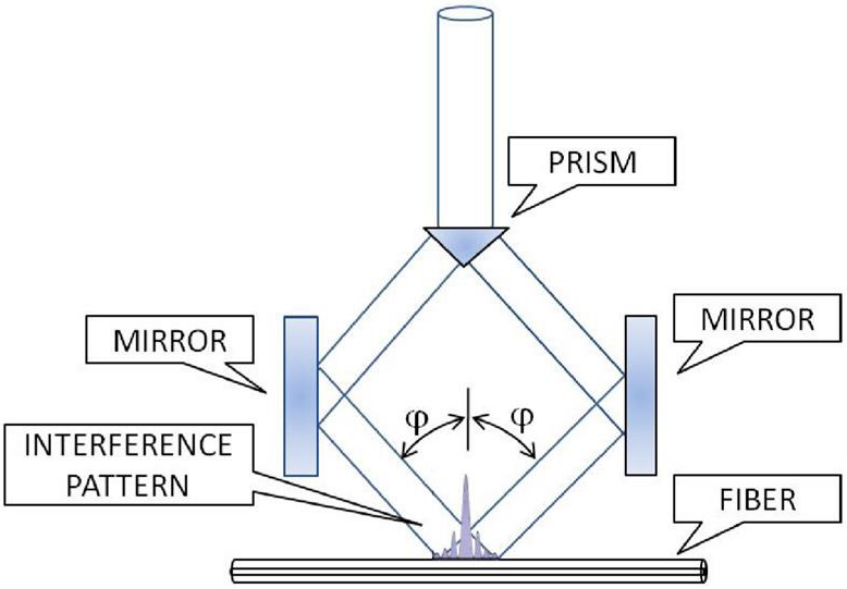

Figure 16: Schematic of the interferometric technique to FBG inscription.

Inscribing grating can be done using the on-tower inscription method as shown in Figure 17 [55]. One advantage for the mechanical strength of the grating is the application of the coating on the fiber after the inscription of the grating. In addition, the speed of this technique is another advantage. One disadvantage is the low efficiency of this technique. A steady continuous illumination is not often possible because of the use of a single short pulse for the inscription.

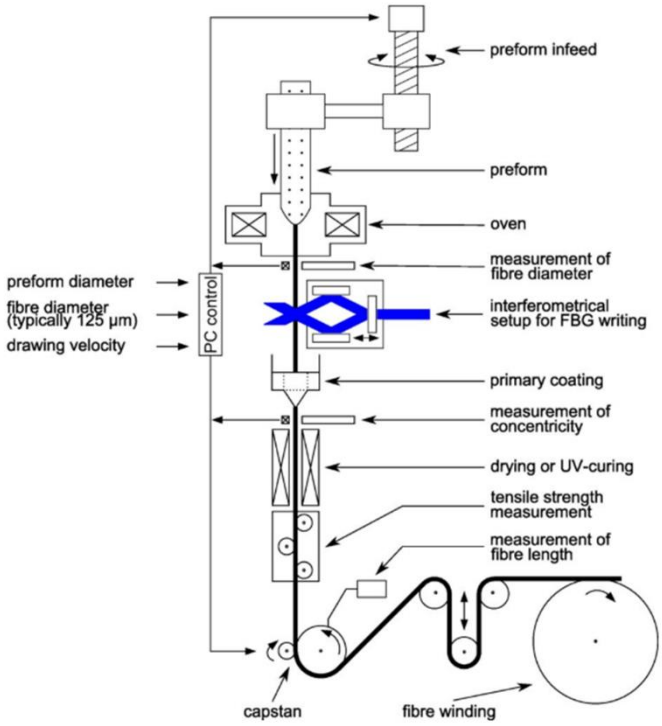

Figure 17: Schematic of the point-by-point approach to FBG inscription

A very stable and precise translational system is essential to the point-by-point fabrication technique as shown in Figure 18 [56][57]. One advantage of the point-by-point technique is that its flexibility to alter the Bragg Grating parameters because the grating structure is built up a point at a time [58] [59].

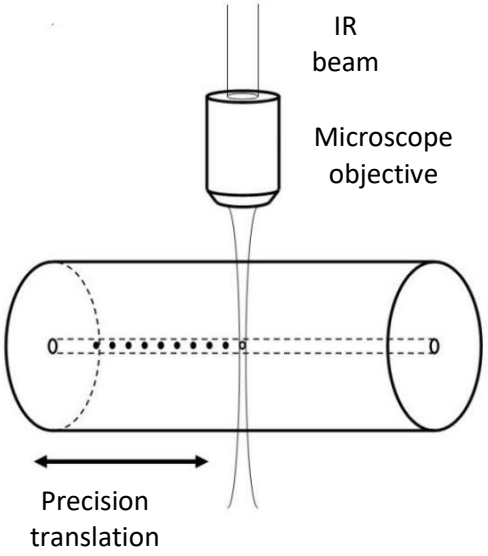

Figure 18: Schematic of the on-tower inscription method

The main drawback of the point-by-point technique lies in the tedious process. This method takes a relatively long process time because the step-by-step process.

Several types of Fiber Bragg grating exist such as the uniform Bragg reflector, the chirped Bragg grating and the blazed Bragg grating [52]. They are distinguished by their grating pitch, tilt angle or spacing between grating planes and fiber axis. The Bragg reflector that has a constant pitch is the most common fiber Bragg grating [56]. This Bragg reflector can function as a reflection filter with a narrow-band transmission or as a broadband mirror, which depends on the parameters such as the grating length and magnitude. When combined with other Bragg reflectors, these devices function as a band pass filters. FBGs are considered as excellent strain and temperature sensing devices because of the wavelength measurements.

The chirped grating is realized by axially varying either the index of refraction of the core or the period of the grating or both. The chirped grating has a pitch that is aperiodic, which corresponds to a monotonic increase in the spacing between the grating planes. Various method for writing chirped grating exists. The double exposure technique has been used in forming a long chirped grating of 1.5 cm [60]. Another technique for producing chirped gratings is based on the phase mask. In this technique, the linear chirp is approximated by a step chirp. A cascade of multiple gratings with increasing period was used in order to simulate a long chirped grating [61].

For the blazed grating, the angle between the grating planes and the fiber axis is less than 90°. Its phase fronts are tilted with respect to the fiber axis. Blazed Bragg gratings are obtained by tilting the grating planes at angles to the fiber axis [62]. As a result, the light is coupled out of the fiber core into a loosely bound guided cladding modes or outside the fiber into radiation modes. The coupling efficiency and bandwidth of the light is determined by the tilt of the grating planes and the strength of the index modulation.

Different types of gratings are produced by varying the conditions of the UV irradiation. The transmission and reliability properties of a grating are affected by the intensity or time of UV exposure required for the writing of the gratings [63]. This results in the formation of different types of gratings that have different characteristics such as the formation of type I at low fluence, type IA [64], type II gratings [65] or type IIA gratings [66].

Type I Fiber Bragg grating are generally formed at low intensities. Type I is a standard grating written into a fiber with or without H2 loading. These FBGs are erased at ≈ 200 °C. They are most used in telecommunication and sensing applications in the temperature range of -40 °C to +80 °C.

Type IA grating is regenerated after an erasure of a type I grating in a hydrogenated fiber [64]. This type of grating is better for strain sensing due to its small temperature coefficient. It also has a better thermal stability compared to type I gratings.

Type II grating is formed by the damage of the fiber core due to the increasing of the energy density. One important thing is the thermal history of the fiber. This grating is characterized by a damaged core-cladding interface caused by a high fluence UV irradiation. These FBGs can resists up to 700 °C. When the energy of the writing beam is increased above 30 mJ the grating is damaged, which forms the type II Bragg gratings. Physical damage is caused in the core of the fiber on the side of the writing beams. This grating tends to have an irregular reflection spectrum due to the hot spots in the laser beam profile. Gratings have

been generated with better reflection profiles but with a much reduced reflectivity, by spatially filtering the beams. These gratings are stable up to ≈ 700 °C.

The type IIA gratings are formed at low power densities. Type IIA is written by a prolonged UV irradiation in a photosensitive fiber [66]. The writing process is slow (30 min). The grating is regenerated after an erasure of a type I grating in a non-hydrogenated Ge-doped fiber. They are erased at ≈ 500°C. This grating is strong and withstand a high temperature and used for sensing at high temperature.

The difference between type I and type IIA gratings is due to the erasure of the first-order and the onset of second-order gratings. The long exposure erases completely the initial first-order grating while the second-order grating forms [65].

1.2.7.3 Sensing with Bragg Grating: Advantages and drawbacks

Standard based electronics sensors are not immune to electromagnetic interference; thus the privilege is given to glass or polymer optical fibers and optical fibers were used in sensing applications. Besides, fiber Bragg Grating sensors are wavelength encoded because it uses the change in the refractive index. However, disadvantages such as bending increases the noise of the signal.

It is evident that material properties of glass and plastic are function of temperature, pressure, vibration and strain. Thereby, it is not surprising to find that the waveguide itself is sensitive to its environment. Bragg grating is a special type of a distributed Bragg mirror constructed into an optical fiber. According to the specifications of the FBG, when a broadband light is coupled into the FBG a portion of the incident spectrum is transmitted, whereas the other portion is reflected. Fibre Bragg Grating were researched principally for sensor applications as the refractive index of a waveguide is function of temperature, humidity and strain [67].

FBG has gained a strong interest among researchers due to their applications in numerous fields such as respiration monitoring, biomedical sensing, civil engineering, structural health monitoring, railways systems, aeronautics, and nuclear environments the electrical power industry and specialized industrial sectors [5],[6],[7],[8],[9]. FBG sensors have the following properties, which enables them to gain wide application in electrical machine due to their advantages [68][69] over other temperature sensors:

- They are small and lightweight, highly compact and used in airborne and space-based sensing applications. They offer high accuracy and sensitivity compared to typical mechanical based sensors.
- Silica fibers can be used in harsh environment [70], also in high temperature and rugged environments. They are immune to electromagnetic interference and chemically passive material, which are not affected by corrosive factors present in the environment.
- Flexibility for customized applications: Single mode fibers provide loss-less transmission and collection of optical signals properties. This property can be used for remote sensing operations.
- The possibility of multiplexing: the advantage of distributed sensing capabilities is the use of a common source and detection system to interrogate multiple sensors placed

at different locations at the same time. Different multiplexing arrangement can be used such as wavelength division multiplexing (WDM) that exploits the bandwidth of source in order to interrogate a series of sensor points that are written along an optical fiber, the time division multiplexing (TDM) which utilizes the ability to separate in time the response of one sensor from another by a length of fiber optic that acts as a delay line.

These very specific characteristics of FBG sensors enables them to be the solution to monitor rotors during their operation. This allows detecting early thermal aging of electrical machines. The fiber optic sensors are costly and need trained personnel for their installation and data analysis. These are limitations to fiber optic sensors in comparison to conventional electronic, mechanical or chemical sensors. Over the last 30 years, the prices of fiber optic and optoelectronic components such as laser diodes and single-mode fibers have decreased by a factor of around hundred. As the technology mature further, this downward trend in prices will continue, which may open up newer possibilities for the technology of the optical fiber sensor.

1.3 ELECTRICAL MACHINE TYPES

The basic types of Electric Machines in electrical vehicles are expected to have some important requirements. These requirements are essential regardless of machine type such as high efficiency, high rated torque, high starting torque, wide speed range, high overload capacity, high power at cruising speeds, high specific power and power density, fast dynamic response and high reliability. In addition, the cost of the machine that meets all of these requirements have to be acceptable. The basic types of machines used in electric vehicles are: induction machines Figure 19 [71], switched reluctance machines Figure 20 [72][73], permanent magnet synchronous machine Figure 21 [74], synchronous reluctance machines and DC machines.

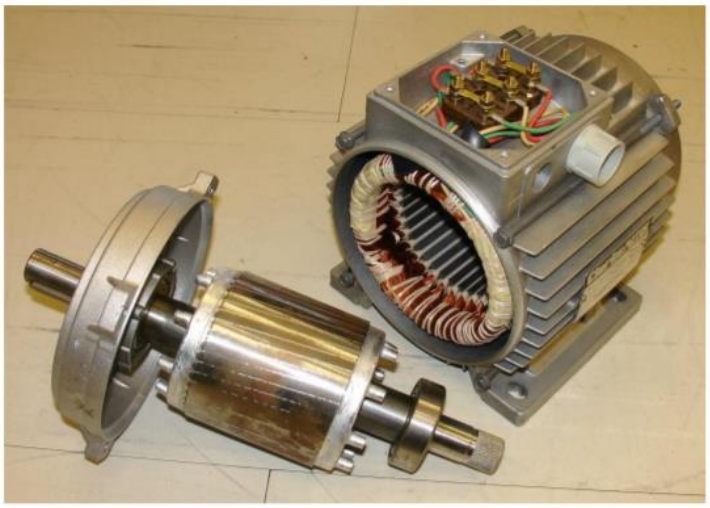

Figure 19: Induction machine components showing: motor cut-out; copper rotor

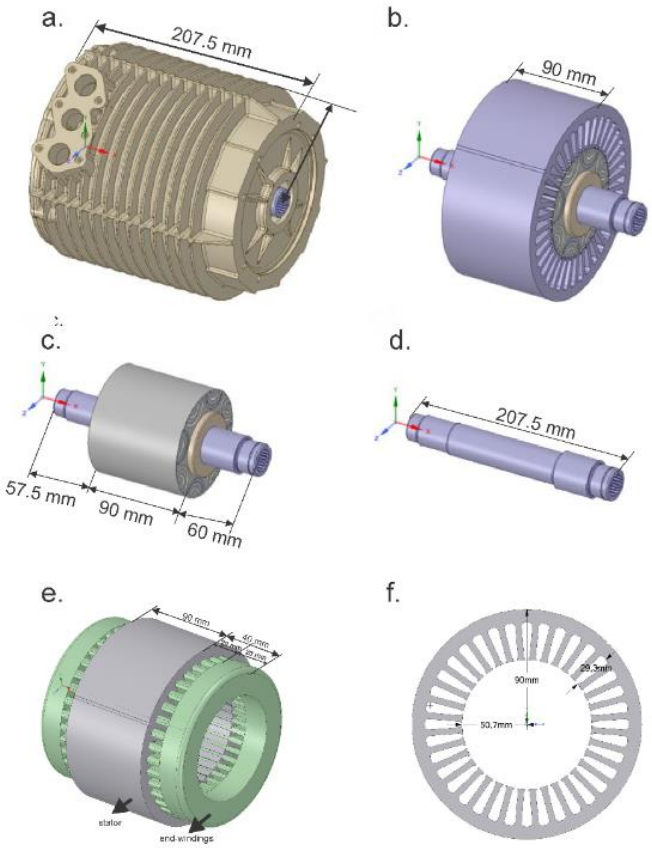

Figure 20: The 3D geometry of the interior permanent magnet IPM motor: (a) stator, rotor and shaft with the housing; (b) stator, rotor with magnets and the shaft; (c) rotor with magnets and shaft; (d) shaft only; (e) stator with windings; (f) dimensions of the stator lamination

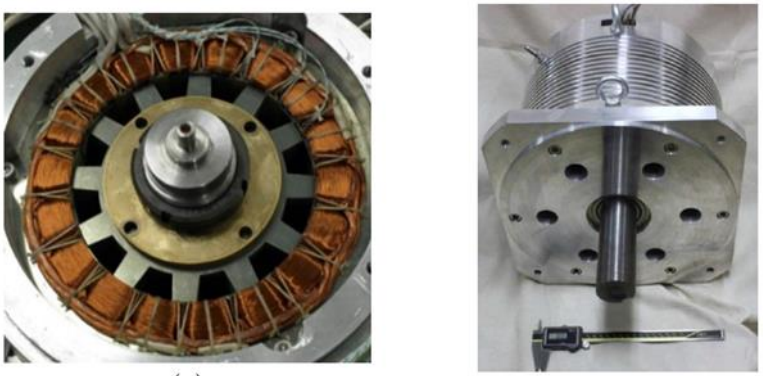

(a) (b)

Figure 21: Switched reluctance machine (SRM): (a) rotor inside the stator; (b) assembled motor

1.4 REVIEW OF THE TEMPERATURE MEASUREMENT TECHNIQUES IN THE ELECTRICAL MACHINES

The temperature is widely monitored in generators and electrical drives. Temperature monitoring of specific areas of the stator or the cooling fluids of large electrical machine is common [75]. These measurements can only give indications about the big changes that takes place within the machine. However, when they are mounted and monitored in carefully selected sites, they are very effective [76].

Temperature measurement provides valuable monitoring information especially when combined with information about other conditions of the machine. There are three principal methods of measuring electronically the temperature by using resistance temperature detection, thermistors and thermocouples whose characteristics were described in section 1.2.

Techniques such as fiber optic temperature sensor, IR thermometer and quartz thermometers achieve high accuracy, fast response and provide non-contact solutions. They are more expensive than the other techniques described earlier. However, they have not been widely used in condition for monitoring electrical machines. For example, fiber optic temperature sensors have been applied to identify hot spot in transformers and more recently in synchronous machines [77][78].

The measurement of temperature therefore has an important place in monitoring electrical machines. There are three different approaches to temperature monitoring: measuring local temperatures at points in the machine using embedded temperature detectors and using a thermal image fed with suitable variables to monitor the temperature of what is perceived to be the hottest spot in the machine. In addition, measuring distributed temperatures in the machine or the bulk temperature of the coolant fluid.

These approaches demonstrate the fundamental difficulty of thermal monitoring, which is resolving the conflict between point temperature measurements that are easy to make but give only local information and bulk temperature measurements that are more difficult and run the risk of overlooking local hot-spots. The following three sections show how these approaches can be applied practically.

1.4.1 Local temperature measurement

The local temperature measurement is done using thermocouple, RTD or embedded detectors. In order to detect hot spot temperatures, detectors are usually located in the bearings. They can also be embedded in the stator winding or core in order to monitor the active part of the machine.

In fact, during the specification stage of the machine, the choice of location should be considered carefully. For example, the temperature detectors should be located close to the hottest part [79] (slot portion or end-winding portion) when embedded in the stator winding. This depends on the thermal design of the machine.

RTDs and thermocouples detectors are metallic devices and the disadvantages of these methods is that they need electrical insulation. Therefore, they cannot be located on the hottest active component such as the winding copper. These devices should be embedded

in the insulation of a winding at some distance from the copper. As a consequence, the temperature that is measured will be an estimate of the winding temperature.

An alternative is the development and the use of a temperature-monitoring device that gives electrical isolation and can also be attached to a high voltage winding. Fiber optic techniques are modern methods that measure temperature in high voltage components [80].

For many machines, the hottest spot is located on the stator considering its thermal design. However, for other machines the hottest spot is located on the rotor and all the temperature measurements described so far have been on stationary parts of the machine. For example, larger induction motor is rotor critical in which the rapid rise of the temperature could produce damage to the rotor. A weakening of the rotor bars and the end rings is caused by an apparent deterioration. As a result, a premature mechanical failure is produced if this occurs repeatedly to such machines.

Various experimental methods for measuring rotor temperatures have been proposed in the past by using thermocouples connected through slip rings or heat-sensitive papers [81]. However, there has not been a sufficiently reliable method to use for temperature monitoring purposes until recently.

1.4.2 Hot-spot measurement using thermal imaging

Knowing the operating temperature of the hottest point in the machine is not always sure because temperature detectors may not be located at the key points. This create suspects about local temperature measurements by machine operators. It is difficult to obtain winding temperatures in components where high voltage isolation and high thickness of electrical insulation is necessary such as in transformers. Therefore, thermal images of the hot spots are used for motor monitoring and protection purposes as proposed by [82], [83]. They proposed a technique that configures a thermal model of the machine in a digital signal processor. The digital signal processor is fed with a signal proportional to the ambient air and the stator winding current. This is done for small totally enclosed forced induction motors. This model can calculate several predicted temperatures at the hottest points. The instrument produces an analogue voltage that is proportional to temperatures at a variety of key points in the machine. In Mellor et al. [84], the stator end winding is the hottest point in this design of the machine. They compared the predictions of the thermal image with the actual measured temperatures in the hottest point. This device provides the thermal protection to a motor. In addition, it could be used for operational purposes when monitoring a machine. For instance, the device could be a part of a machine and located in an accessible location to measure some hot spots that may be difficult to obtain directly by the thermal imaging measurement.

1.4.3 Bulk measurement

An indication of the thermal state of the electrically active part in the machine is needed even when hot spot temperature or locations are measured by using a thermal imager. The internal and external coolant temperature are obtained from the located thermocouples. However, it is rare to give directly the temperature rise values. When the machine is overloaded or the performance of the coolant circuits is not as it should be, the temperature rise increases. An alternative to this method is the use of optical fibers that give

single indications of high temperature from a device that is embedded in the bulk of the machine [85], [86].

1.4.4 Techniques for measuring temperature in the rotating part of the electrical machines

Rotor temperature are not usually monitored because the installation of the sensor on the rotor is difficult. Therefore, it is truly important to detect thermal degradation problems of the rotor to avoid the end of life of the electrical machine. Adding sensors to the rotor of an electrical machine is not yet commercialized because of the difficult instrumentation on the rotating part and reliability. Nevertheless, temperature monitoring can avoid the destruction of the conductors and insulating materials. Therefore, using FBG sensors is a solution to monitor rotors during their operation in order to detect early thermal aging of electrical machines. Moreover, it has the advantage of decreasing the installation cost and the number of copper wires. Different methods for measuring the temperature in the electrical machine have been proposed. Contact temperature sensors (thermocouples, thermistors, etc.) can be inserted directly into the stator structure. The problem of contact measurement methods consists in the installation of the recovery system, either by slip rings connected by brushes to the temperature reading system [81], or via a wireless radio link, which can be very complex or expensive. However, the usefulness of these method is limited because of their installation on the stationary parts. The main problems are the heavy weight, difficult installation, the low signal-to-noise ratio, etc. [87]. Adding to this the fact that the electrical noise can corrupt the collected data.

The main problem in telemetry systems is their susceptibility to electromagnetic interference. In addition the implementation of the electronic systems in high temperature environment is difficult as indicated in Figure 22 [88]. In their scheme, the digital telemetry system is able to manage the output of as many as 88 sensing devices at the same time. It digitizes the information and transmits it back to a receiver.

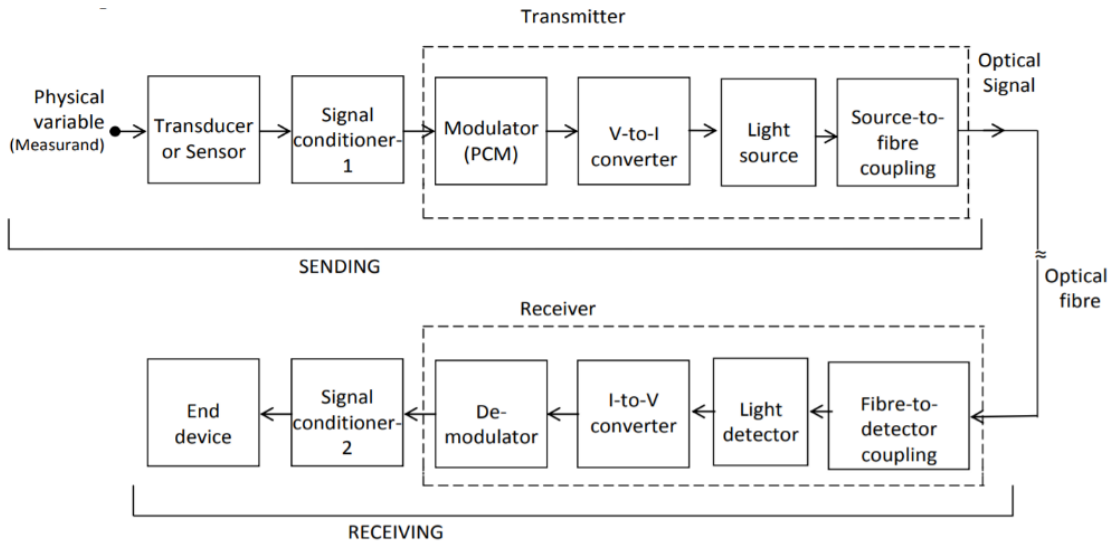

Figure 22: Block diagram of an optical fiber telemetry system

Fiber optic rotary joint (Princetel MJX series) has been used on rotating parts in order to measure temperature between 20 °C and 50 °C as shown in Figure 23 [89] but there is no place for implementing a rotary joint, in some engines.

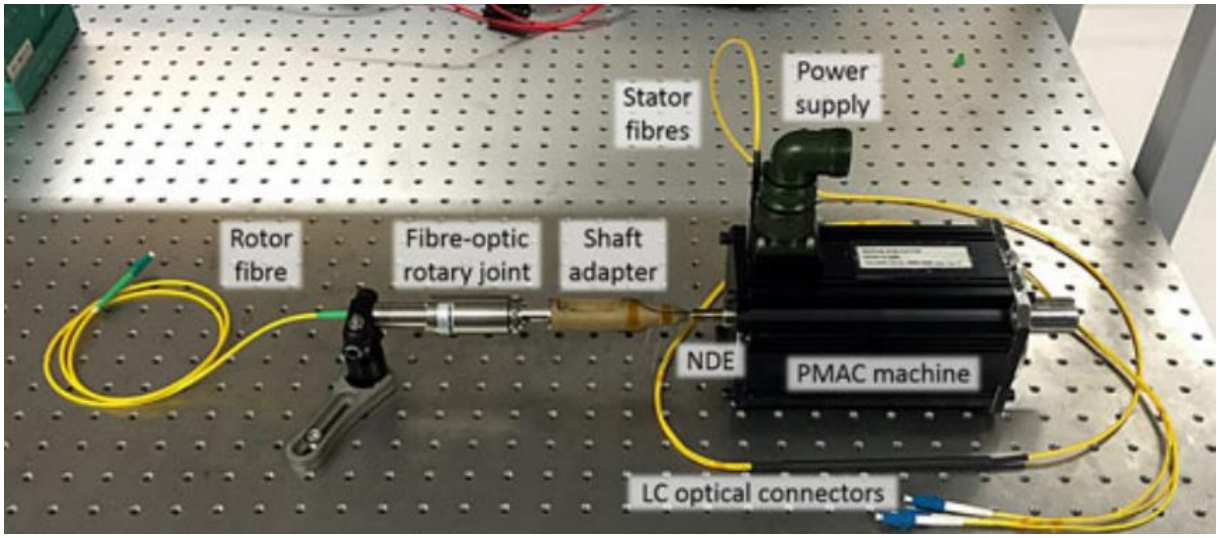

Figure 23: Fiber optic rotary joint used in the PMAC machine

On the other hand, non-contact measurements via infrared sensors (point measurement) or infra-red cameras (temperature field) have been developed. The main problem of these measurement techniques lies in the determination of the emissivity of the different surfaces composing the rotor.

In the late 80's, optical measurement based on phosphor excitation was developed to access the temperature information at the surface of the rotor, as shown in Figure 24 [90][91]. However, this method is limited due to decreasing phosphor's intensity and faster decaying response with increasing temperature. In addition, it is difficult to access some location of rotary components.

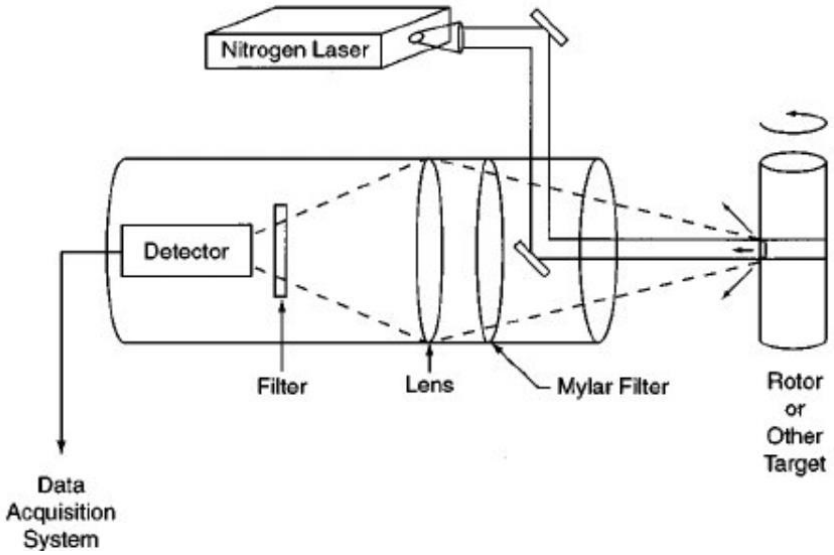

Figure 24: The fundamental elements of a remote fluorescence thermometry system

In temperature sensing, most studies of the evolution of temperature in electrical machines try to estimate because direct measurements are technically difficult. The temperature is obtained from a model with localized semi-empirical constants. The problem of these models lies on the determination of the heat exchange coefficients (mainly conduction and convection), hence the recourse to a calibration of the model from measurements on different points of the machine in particular the temperature measurement of the external casing or the hot spots (windings heads) of the stator [92].

Therefore, all these problems lead to the use of non-contact temperature sensor Fiber Bragg Grating. A number of studies have been carried out in order to measure the temperature using FBG sensors in high power electrical machines.

1.4.5 FBG techniques for measuring temperature in the rotating part of machines

C. Hudon et al. have measured rotor temperature between 20 °C and 120 °C by using commercialized FBG sensors with mechanical decoupling on a 74.75 MVA generator as indicated in Figure 25 [93]. They have compared their FBG temperature measurements with average temperature calculated from voltage and current. In their proposed scheme, the hottest spots of the field winding were 24 °C higher than the calculated average rotor temperature. In addition, localizing optimum locations of FBGs was discussed.

Figure 25: Fans and poles of the unit under investigation (left) and FBG sensor installed on a pole-to-pole connection (right)

Werneck M.M et al. monitored temperature variations of a 216 MW UHE-Samuel Hydro-electric power generator which operates at 95 °C at full load, using FBGs as seen in Figure 26 [94].

Figure 26: Box containing the optical fiber with the FBG inside the U-shape copper tubing (left) and installed inside the generator (right)

They inserted the FBG sensor inside a copper tubing having a U-shape, which guarantees the good heat transfer between the optical fibre and the cooling air and ensures the protection of the sensor from strain effects. They have measured temperature between 20 °C and 85 °C with a 0.08°C uncertainty and an FBG average sensitivity of about 13 pm/°C, which is quite acceptable in the domain of electric power industry. Therefore, the use of FBG sensor in temperature monitoring of generators that has high repeatability, reliability and accuracy was demonstrated.

R.C. Leite et al. proposed the use of FBG sensors to measure the field winding temperature between 40 °C and 100 °C as shown in Figure 27 [95]. In their scheme, they compared these results to FBG readings. The difference of 4.5 °C was found between the FBG and the thermistor readings used as reference.

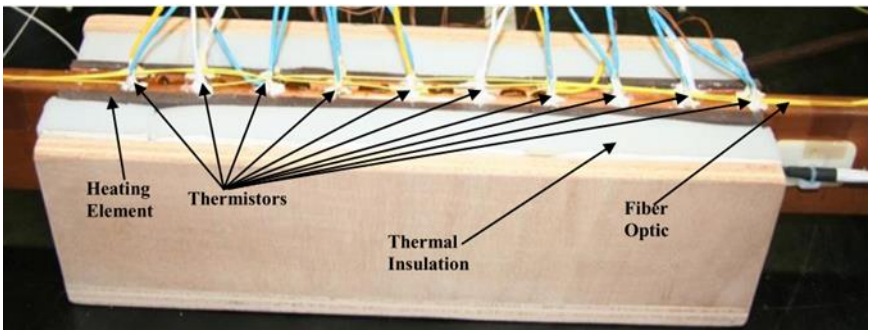

Figure 27: Experimental setup of the FBG installation in the electrical machine

The main limitation of these methods is the integration of FBG in high power (MW) and large-size (meters) electrical machines such as hydro-generators, which is much easier than low power and small size machines.

In the research of Hind et al., the method used is suitable for systems where enough space exists for the interrogator. One should add to this, the low speed of the rotor (< 500 RPM) and the limited temperature range (< 45 °C) [96]. The main challenge is the cabling that enables transmitting accurate signals from the FBG sensors on the rotary side to the stationary side where lies in the interrogation system as seen in Figure 28 [96].

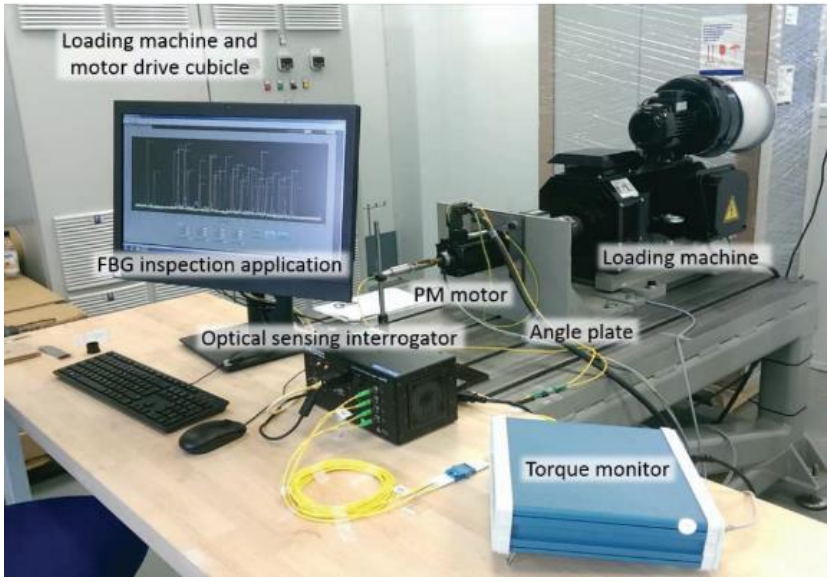

Figure 28: The experimental setup used to experiment the FBG

1.4.6 Conclusion

Temperature measurement has repeatedly been effective as a global monitoring technique for electrical machine. Temperature measurements give indications about the condition of the electrical machine by using simple sensors. Temperature is a valuable monitoring parameter because the high temperature could limit the functioning of a machine. Temperature detection is usually done in traditional ways. The application of FBG sensors should be exploited. These advances will allow temperature measurements to be made as close as possible to some active parts of the machine.

1.5 LITERATURE REVIEW OF THE FBG INTERROGATION SCHEMES

1.5.1 Introduction

Being a reflective device, the FBG sensor must therefore be used in conjunction with a wavelength discriminating system like spectrum analyser or other interrogation methods such as interferometric techniques. Choices of the measurement techniques should be done by taking into account requirements including cost and complexity. Since their first demonstration in 1980, different demodulation schemes have been presented with different techniques. FBG interrogation techniques transform the wavelength modulation into an optical intensity modulation and then into a corresponding electrical signal. The market of

fibre Bragg grating began to emerge only in the nineties. Since then, the interrogation unit of FBG sensors noticed significant evolutions.

In fact, evolution of methods for interrogating FBG optical sensors, have started with interferometers devices (passive homodyne [97], active homodyne [98]). In addition, wavelength-position conversion, which is the use of charge-coupled device (CCD) and a fixed dispersive element, were developed to improve the existing ones. After this stage, the introduction of interrogators based on Fabry-Perot tunable filter laser methods have marked a new era in the array of optical sensing field since such methods offer high optical power that enables measurements over longer fibre lengths.

So far, there are four categories of interrogation technique for wavelength-shift detection, which are passive edge filtering, active band-pass filtering, interferometric interrogation and laser sensing.

1.5.2 FBG sensors interrogation techniques

The following literature review recaps the research interrogation techniques that had been done until now.

Different methods for measuring wavelength-shift of FBG sensors have been proposed in the literature. For Passive edge filtering, Davis et al. proposed a scheme to detect the wavelength shift using a wavelength division coupler and processing electronics [99]. Measurement of both static and dynamic strains were achieved. Also Shung et al. proposed a simple passive demodulation system that involves the use of a polarization maintaining fibre loop mirror and interference phenomenon. In spite of that, this technique is stable compared to Michelson interferometers or conventional Mach-Zhendr [100].

The active band-pass filtering group contains all the techniques based on the use of Band-pass filters with a spectral width of equal or less than the spectrum of the Bragg Grating. We can find in this category Fabry-Perot cavity, which resolution is very high for relatively wide measured range, as well Bragg Grating Tunable filter that have the same properties as the Bragg Grating of the sensor. Francisco et al. reported a technique that relies on the principle of optical fiber filters using the receiving Bragg Grating configuration [101]. In their scheme, active control of a fused biconical WDM is used to tune the spectral characteristics of a WDM over 15 nm ranges in order to analyze wavelength shifts from FBG sensors. In addition, Kang et al. proposed an interrogation scheme to detect the wavelength shift of a dual head sensor [102]. The proposed technique uses a tilted FBG demodulator with the temperature-independent property. Furthermore, another interrogation scheme was proposed by [103] to detect wavelength shifts from the FBG sensor. This detection technique uses a matched grating array to filter and track wavelength shifts.

The wavelength shift induced by the temperature can be measured by interferometric scanning. This method has shown its effectiveness for dynamic and quasi-dynamic measurements using interferometer. However environmental factors significantly increase noise for the lowest frequencies. Donghui et al**.** reported a new sensor interrogation scheme for extracting the strain information [104]. In their letter, linear wavelength response was achieved by using a linearly chirped FBG incorporated with a fiber Sagnac loop. Moreover, A.D. Kersey et al. have demonstrated a high resolution dynamic strain sensor using the

unbalanced interferometer wavelength discriminator approach [105]. Their concept can be configured to multiplex several grating element and also to provide high resolution absolute strain sensing.

Other approaches were demonstrated by T.A. Berkoff et al. that rely on interferometric interrogation such as high resolution sensor system over a high dynamic range, which was coupled to a band pass wavelength division multiplexer to discriminate and detect strain-induced wavelength shifts [106].

1.5.3 FBG interrogators

Spectrometers can be used as Bragg grating interrogators. Spectrometers could be classified onto dispersive or filtering methods depending on their principles of operation.

1.5.3.1 Dispersive spectrometer

This spectrometer disperses the incoming optical signal into its frequency or spectral components as shown in Figure 29 [107]. The dispersive spectrometers are monochromators or spectrographs [108]. The monochromators use narrow slits to select a particular wavelength which depends on the incident angle of the beam on the grating, a single detector and a rotating dispersive element to select a range of wavelength. The monochromators output narrow monochromatic light through the slit.

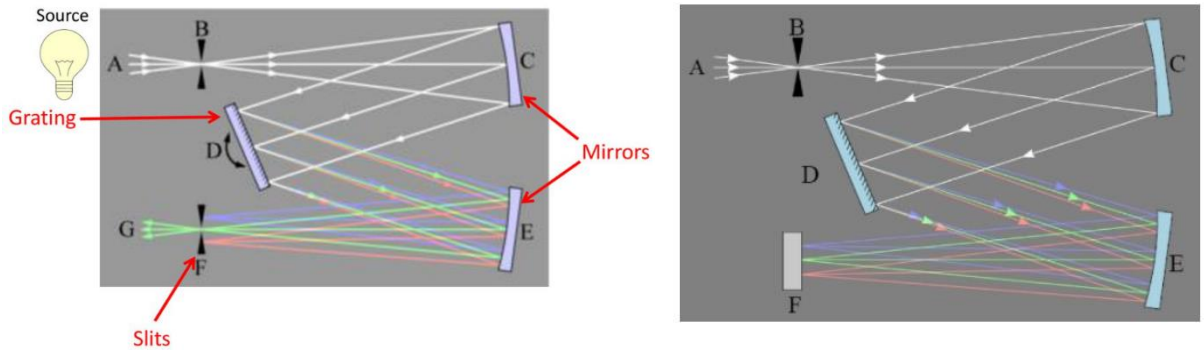

Figure 29: Schematic of a monochromator: A. Source, B. Entrance slit, C. Collimating mirror, D. Grating, E. Focusing mirror, F. Exit slit, G. Single channel detector (left) and a spectrograph: A. Source, B. Entrance slit, C. Collimating mirror, D. Grating, E. Focusing mirror, F. Multichannel detector(right)

Spectrograph uses a stationary dispersive element and instead of using a slit on the exit slit, there will be an array of detector elements. It provides fast but more expensive detection system. The spectrograph will cover spectral elements over a wide range of wavelengths.

1.5.3.2 Filter based spectrometers

Filter based spectrometers transmit a selected range of wavelength by using one or more interference or absorption filters [109]. The absorption or the interference filters block some wavelengths of the incident beam and transmit the desired wavelength as shown in Figure 30 [108].

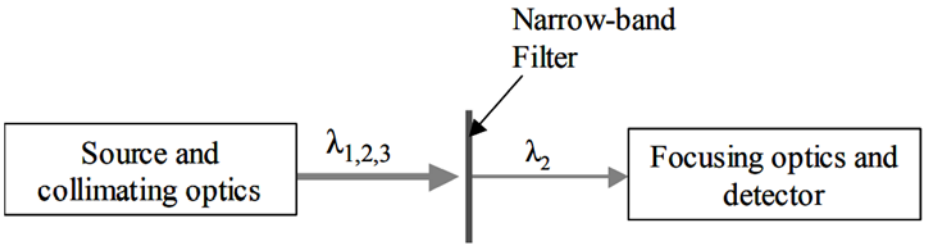

Figure 30 : Schematic of a filter-based spectrometer. The filter selects the transmitted wavelength range through an absorption or interference process

The filter wheel system configuration is commonly used in filter spectrometers. A number of filters are placed near the circumference of the rotating wheel. The wheel is positioned to select a spectral band in such a way the beam is incident on a particular filter. A limited number of discrete wavelength can be selected using this configuration. The tilting-filter element is a variation of the system in which the incident angle of the beam on the filter changes in order to select a spectral band. The range of wavelength is limited.

An important number of companies produce interrogators suitable for interrogating FBG sensors. The specifications of their interrogators are shown in Table 1.

Table 1: Specifications of some FBG interrogators in the industry

Company	Wavelength range	Optical resolution	Measurement frequency	Number of optical lines	Max. number of sensors per optical line	Application	Dynamic range:
MICRON (si155 or sm130)	1500-1580 nm	2 pm	5000 Hz			Dynamic analysis 1529-1598.2	17 dB peak
Scaime (MDX-400T-X or MDX-8000)	1528-1565 nm	<1 pm/3pm	100 Hz / 1-2 KHz	3-4/4-8	16	Harsh environment/high speed acquisition	~0.02-8.4 nm FWHM
Smart Fiber (SmartScan Aero Mini or SmartScan)	1528-1568	1 pm	2.5-25 KHz	4	16	Harsh environment(aerospace flight)/dynamic measurements	27 dB
Idil fiber (FBGuard 1550 FAST)	1510-1590	<1 pm	125 Hz -11 kHz	1,2,4 or 8	40	Dynamic measurement	30 dB
Cementys (Bragglogger)	1520-1580	16 1 pm	16 1.25-5 KHz	40 1-4	16		
Femto Fiber (FAZT I4G)		1 pm	250 Hz-8 KHz	16	1-30		

1.6 CONCLUSION

Temperature sensors were reviewed in this chapter. Temperature sensors based on optical fiber showed that they play a key role in sensing and they are a main asset in different areas. They offer several advantages over conventional sensors, which open way for specific applications where conventional electrical or mechanical sensors fail. The main drawback to their industrial invasion is their cost rather than the technology. Their cost will be continuously reducing since the prices of opto-electronic components and fiber optic drops over time. We showed the different fabrication methods and types of such FBGs. FBGs are used in many potential applications in different fields but it is not possible to offer Fiber Bragg Grating systems without the interrogation unit.

We researched existing methods in the literature for measuring temperature in the electrical machines. Fiber Bragg Gratings sensors were presented with a focus on their use as a sensing elements and pointed out the advantages of using Fiber Bragg gratings (FBGs). Fiber Bragg grating as a sensing element is intrinsic in the fiber, which is an added to all the advantages of fiber optic sensors avoiding therefore the insertion losses. Then, we reviewed different methods for measuring temperature using FBG sensors in the electrical machines proposed in the literature.

A summary of the state of the art of the interrogation techniques using FBG. We elaborated on the different techniques of the FBG interrogation systems such as optical filter methods that include interferometer, scanning Fabry-Perot filter or paired matched grating detection and fibre optic interferometric sensor such as Mach-Zehndr, Sagnac and Michelson interferometers. An optical spectrum analyser or monochromator can be used to measure the spectral shift with limited resolution. However, these devices are often bulky and expensive. Moreover, they are not fast enough or sensitive for current applications. Interferometer has many disadvantages, such as the need of pulsed source, appropriate fibre lengths between sensor element, high speed photo detection and switching element. Scanning Fabry-Perot filter has some inconvenience because it is limited in bandwidth and sensitivity and it relies on wavelength multiplexing a number of FBG elements. Fibre optic interferometric sensor such as Mach-Zehndr, Sagnac and Michelson interferometers are extremely sensitive, but their high cost and overall bulk optics militate against their use as detection system in complex environments.

Besides, many of these techniques used to detect wavelength shift have been shown to provide very high sensitivity, most of them are only used in the laboratory environment.

Last in this chapter, we presented the FBG interrogators providers. It can be concluded that the solution to monitor rotor temperature in electrical machines could be the use of fiber Bragg grating sensors.

In the next chapter the FBG sensor will be modelled using TMM method to find its sensitivity. Then in chapter 3, the temperature measurement with FBG sensor will be experimentally validated and compared to the simulated one. After that in chapter 4, we will install the FBG sensor in the electrical machine in order to make dynamical temperature measurements. The interrogation system will consist of only one spectrometer. Temperature

measurements will be done between 20 °C and 70 °C for a maximum rotating velocity of 860 rpm.

CHAPTER 2

MODELING AND SIMULATION OF FIBER BRAGG GRATING

2.1 INTRODUCTION

From the previous chapter, we showed the need for a temperature sensor that can operates at high temperatures and in the presence of electromagnetic fields for applications such as electrical motors, power stations and others. A possible solution to this problem can be the use of FBG sensors.

First, this chapter gives a general introduction about the technology of sensing with Bragg Grating and a summarized description of its theoretical background. Then, a literature review of the different methods for grating simulation proposed in the literature is presented.

Secondly, in this thesis, special emphasis is on the Coupled mode theory (CMT) and the transfer matrix method (TMM) to model and analyze the light propagation and interaction with materials in an optical fiber.

Then, the simulation of uniform FBG using transfer matrix is presented. After that, the spectral reflectivity of the uniform FBG is simulated. The spectral reflectivity dependence on grating length and on index change is analyzed. The bandwidth FWHM dependence on grating length and refractive index change is also simulated and analyzed.

Last in this chapter, we will present the results of the simulation of the temperature and strain response before concluding the chapter.

2.2 FIBER OPTIC SENSORS

The optical fiber consists of a core and a cladding. The core and the cladding have a refractive index n_{core} and $n_{cladding}$, respectively. The light is guided into the core by total internal reflection at the cladding core interface if the refractive index of the core is slightly larger than the refractive index of the cladding. The surrounding cladding material that is made from silica has a lower refractive index than the core region. Therefore, the light is trapped in the core of the fiber by total internal reflection at the core-cladding interface. Numerical Aperture is the acceptance angle of the fiber, which is defined by the two refractive indices as:

$$NA = \sqrt{n_{core}^2 - n_{clad}^2} \tag{2-1}$$

The total internal reflection of light inside an optical fiber is depicted in Figure 31.

Light is guided into the core if the angle of incidence is smaller than the critical angle θ. However, the light will leave the core of the fiber into the cladding if the angle of incidence of the light is larger than the critical angle.

$$NA = nsin\theta \tag{2-2}$$

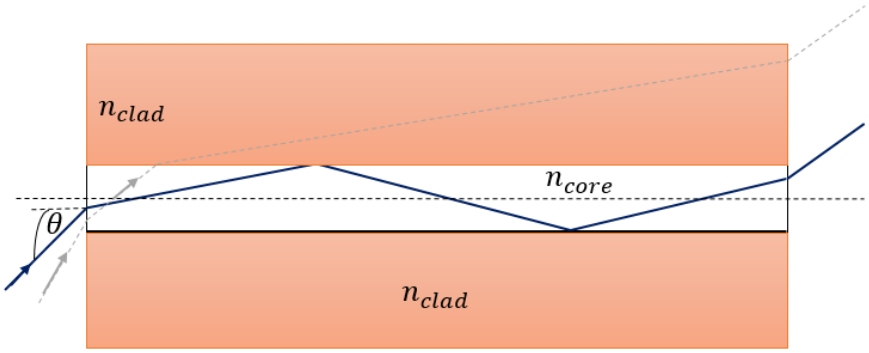

Figure 31: Total internal reflection into the fiber core

One or more confined transverse modes of the light propagates along the fiber. The normalized frequency v determines if the fiber is multimode ($v > 2.045$) or single mode ($v < 2.045$), v is given by [44]:

$$v = \frac{2\pi r}{\lambda}\sqrt{n_{core}^2 - n_{clad}^2} = \frac{2\pi r}{\lambda}NA \tag{2-3}$$

Where λ is the propagated wavelength and r is the core radius.

2.3 SENSING WITH BRAGG GRATING

Standard based electronics sensors are not immune to electromagnetic interference; thus the privilege is given to glass or polymer optical fibers. Therefore, fields of sensing applications were opened to optical fibers, which are based on light intensity encoding schemes. Fiber Bragg grating sensors are wavelength encoding because it uses the change in the refractive index. However, disadvantages such as bending or interactions with the fiber increase the noise of the signal.

It is evident that material properties of glass and plastic are function of temperature, pressure, vibration and strain. Thereby, it is not surprising to find that the waveguide itself is sensitive to its environment and its cladding's refractive index as well. In fact, Bragg grating is a special type of a distributed Bragg mirror constructed in an optical fibre. When a broadband light is coupled into the FBG a portion of the incident spectrum is transmitted, whereas the other portion is reflected. Fibre Bragg Grating were researched principally for sensor applications as the refractive index of a waveguide is function of temperature, humidity and strain [67].

2.3.1 Bragg wavelength shift with temperature changes

The FBG is used for sensing as following: The Bragg wavelength reflection λ_b is dependent on temperature, which is the external parameter to be sensed as shown in Figure 31. Moreover, the Bragg wavelength is functionally dependent on this parameter and it is calculated as:

$$\lambda_b = 2n_{eff}\Lambda \tag{2-4}$$

where n_{eff} is the effective index of the core mode and Λ is the spatial period of the grating.

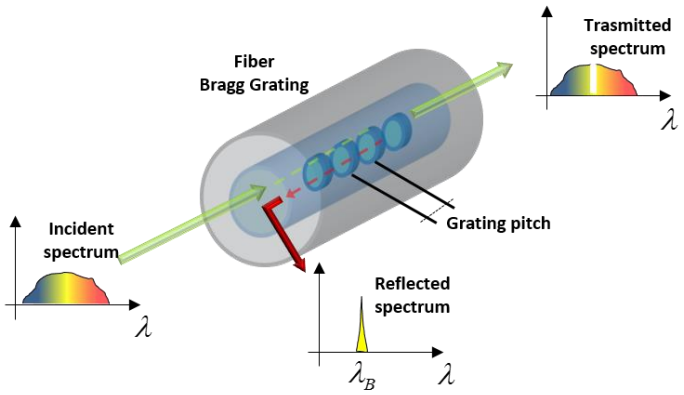

Figure 32: Principle of temperature sensing with Fiber Bragg Grating (FBGs)

Using equation (2-4), the shift in the Bragg wavelength due to temperature changes is caused by the thermal expansion that changes the physical length of the grating period and the change in the effective refractive index of the optical fibre, as shown in Figure 33 [110]. This change in the Bragg wavelength due to temperature perturbation is defined as:

$$\Delta\lambda_{B0} = \lambda_b \tilde{\xi}\, \Delta T \tag{2-5}$$

where λ_b is the Bragg wavelength, $\tilde{\xi}$ is the thermo-optic coefficient (TOC) and ΔT is the temperature change.

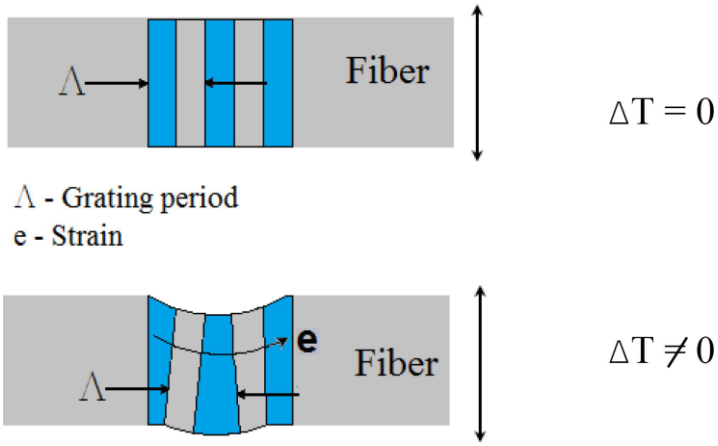

Figure 33: Grating change in the optical fiber induced by a change of the temperature

The thermo-optic coefficient $\tilde{\xi}$ is the summation of the thermally induced refractive index change ${n_{eff}}^{-1}\ dn_{eff}\ /\ \mathrm{dT}$ and the thermal expansion coefficient α, therefore the wavelength shift can be given as [111]:

$$\Delta\lambda_{B0} = \lambda_b(\alpha + {n_{eff}}^{-1}\ dn_{eff}\ /\ \mathrm{dT})\ \Delta T \tag{2-6}$$

As can be seen in the effective index and the grating pitch are the only factors that can change the Bragg wavelength. The change in the reflected wavelength due to the change in temperature, assuming no strain, is given by:

$$\mathrm{d}\lambda_b = 2n_{eff}\,\mathrm{d}\Lambda + 2\Lambda \mathrm{d}n_{eff} \tag{2-7}$$

$$\frac{\mathrm{d}\lambda_b}{\mathrm{dT}} = 2\left(\frac{dn_{eff}}{dT}\right)\Lambda + 2\left(\frac{d\Lambda}{dT}\right)n_{eff} = \lambda_b\left(\frac{1}{n_{eff}}\left(\frac{dn_{eff}}{dT}\right) + \frac{1}{\Lambda}\left(\frac{\mathrm{d}\Lambda}{\mathrm{dT}}\right)\right) = \lambda_b(\tilde{\xi} + \alpha) \tag{2-8}$$

For example, a grating at 785 nm the shift in the Bragg wavelength corresponds to:

$$\frac{\mathrm{d}\lambda_b}{\mathrm{dT}} = 785\ \mathrm{nm}\ .\ (9.2 + 0.55).\ 10^{-6}\ °\mathrm{C}^{-1} = 7.65\ \mathrm{pm/°C}$$

With $\alpha\ = 0.55\ .\ 10^{-6}\ °C^{-1}$ the thermal expansion coefficient and $\tilde{\xi} = 9.2\ .\ 10^{-6}\ °C^{-1}$ the thermal expansion coefficient.

2.3.2 Bragg wavelength shift with axial strain changes

As can be seen in (2-9) axial strain change the n_{eff} and the Λ:

$$\frac{\mathrm{d}\lambda_b}{\mathrm{d}\varepsilon} = 2\left(\frac{dn_{eff}}{d\varepsilon}\right)\Lambda + 2\left(\frac{d\Lambda}{d\varepsilon}\right)n_{eff} = \lambda_b\left[\frac{1}{\mathrm{n_{eff}}}\left(\frac{\mathrm{d}n_{eff}}{\mathrm{d}\varepsilon}\right) + 1\right] \tag{2-9}$$

A change in the applied strain gives rise to a different index of the fiber material, as can be seen from (2-10) for n_{eff} :

$$\Delta n_{eff} = -\frac{n_{eff}^3}{2}[\varepsilon(1-\nu)p_{12} - \nu\varepsilon p_{11}] \quad (2\text{-}10)$$

where p_{11} and p_{12} are the coefficients of the stress-optic tensor.

A change in the Bragg wavelength can be related to both a change in the refractive index as in the grating spacing, according to (2-1).

The change in the period of the grating is given by: $\Delta\Lambda = \varepsilon\Lambda$ (2-11)

Inserting (2-11) into (2-10) and filling in (2-1) gives (2-12):

$$\Delta\lambda_b = \varepsilon\lambda_b - \frac{\varepsilon\lambda_B n_{eff}^2}{2}[p_{12} - \nu(p_{12} + p_{11})] = \varepsilon\lambda_b(1 - p_{eff}) \quad (2\text{-}12)$$

With $p_{eff=}\ \frac{n_{eff}^2}{2}[p_{12} - \nu(p_{12} + p_{11})]$ (2-13)

Where p_{eff} is the effective photo-elastic coefficient.

From (2-9) the change in the Bragg wavelength can be related to the strain applied to the fiber grating. At constant temperature, the strain response using $p_{11} = 0.113$ and $p_{12} = 0.252$ [112] is given by:

$$\frac{1}{\lambda_b}\frac{\mathrm{d}\lambda_b}{\varepsilon} = 0.798\,.10^{-6}\,\mu\varepsilon^{-1} \quad (2\text{-}14)$$

The corresponding shift in the Bragg wavelength is 0.622 $\mathrm{pm}/\mu\varepsilon$ for a grating at 785 nm.

2.3.3 Analytical modeling of the thermal sensitivity of the FBG

POFBG have lately emerged. In 1999, Peng et al. wrote the first FBG in POFs [113], nevertheless FBG in POF have not ripened in commercial applications yet. POFBG have showed several applications such as temperature, pressure, humidity [114] and strain measurements, however different materials properties of the POFBG lead to different sensitivities and measurement ranges for the same applications.

Polymeric materials show the same thermo-optic coefficient and thermal expansion coefficient order of magnitude, which is not the case of fused silica where the TOC is higher than the TEC, as shown in Table 2 [115].

Moreover, as reported in [116], thermal expansion coefficients (TEC) do not vary significantly. For instance, these coefficients are 70 × $10^{-6}\ K^{-1}$ and 65–70 × $10^{-6}\ K^{-1}$ for polystyrene and polycarbonate, respectively.

Table 2: Thermal and optical properties of PMMA and Fused Silica

	Thermal expansion coefficient (TEC)	**Thermo-optic coefficient (TOC)**
Fused Silica	5.5-6 × 10^{-7} °C^{-1}	9.9-10.5 × 10^{-6} °C^{-1}
PMMA	3.6 – 6.5 × 10^{-5} K^{-1}	-10.5 × 10^{-5} K^{-1}

2.3.3.1 Thermal sensitivity of Plastic FBG

Due to the high thermal expansion coefficient of different polymer materials, the thermal sensitivity of the POF Bragg Grating sensor is greater than with glass fibers, as seen in Figure 34 [117].

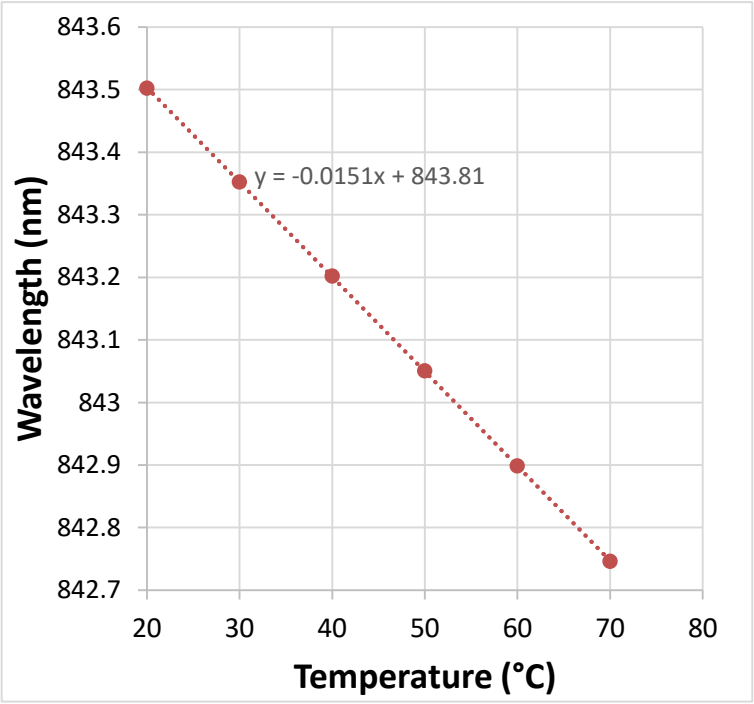

Figure 34: Shift in the Bragg wavelength as a function of temperature for polymethylmethacrylate

2.3.3.2 Thermal sensitivity of Silica FBG

In case of fused silica, $\Delta\lambda_{B0}$ is considered linear to temperature changes since the sum of coefficients is significantly higher than their product. As a consequence, λ_{B0} reveals positive shift with increasing temperature. In contrast, the prominent dependence of POFBG on the negative thermal expansion coefficient of the material makes its thermal behavior significantly more complex compared to glass fiber. Therefore, λ_{B0} shifts towards shorter wavelengths with increasing temperature as depicted in Figure 35.

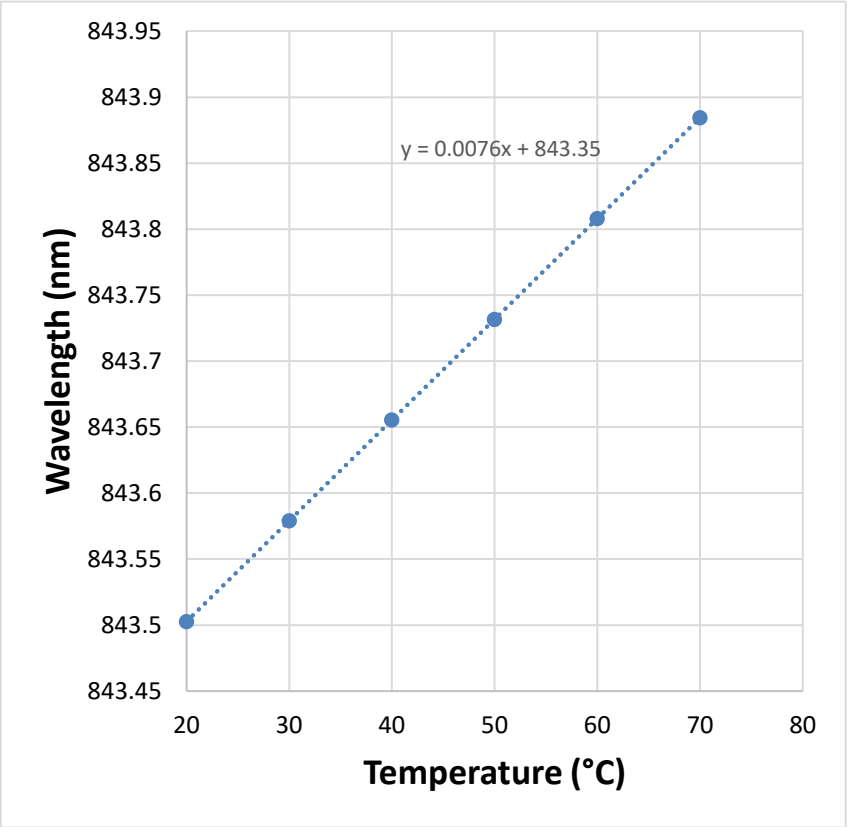

Figure 35: Shift in the Bragg wavelength as a function of temperature for Silica

2.4 MODELING OF FBG

2.4.1 Methods for grating simulation in the literature

Bragg grating modeling is a procedure that describes the interaction of guided modes in the fiber with the periodic structure by knowing the behaviour of the transmitted or reflected signal. Bragg grating fibres can be modeled using the methods developed to calculate the transmitted or reflected intensity by a multilayer structure. In general, the modeling of a Bragg grating inscribed by UV or IR laser is done using several techniques: mode

coupling theory, matrix method or Rouard's method [118]. The Bragg grating reflection can be calculated using these techniques.

The straightforward numerical integration of the coupled mode equations is simple but it is not the fattest. Inverse scattering method is a powerful technique based on integral coupled mode equations which allows the design of a grating with particular characteristics. Another method, proposed by Rouard and applied by Weller-Brophy and Hall, divides the waveguide into subwavelengths thin films [118]. It accurately simulates the characteristics of the grating periods. However, it has the disadvantage of being slow and laborious. Another method, the Block theory has been used to analyses complex grating, which leads to a deeper physical insight into the dispersion characteristics of the gratings. A more recent approach taken by Peral et al. exactly solves the inverse scattering problem for the design of a desired filter. Other theoretical tools such as Variational [119] and effective index [120] method has been developed for solving the transfer function of the FBG.

In this work, the matrix method is applied to the different structures of the grating in order to calculate the reflected wavelength. We will describe the matrix calculation in detail. In order to obtain the spectral response of the FBG, the transfer matrix approach is used to solve the coupled mode equations. It is the most commonly used method for simulating FBGs.

2.4.2 Modeling of the FBG using transfer matrix approach

In order to understand the optical properties of the Fiber Bragg Grating, the coupled mode theory (CMT) [121],[122] is used. In this work, the analytical solutions of the coupled mode theory are used without demonstrating the whole steps. In our work, we used a single mode FBG and we assume the fiber is weakly guiding and no energy is coupled to radiation modes.

TMM is a fast and accurate technique for analyzing complex structure and calculating the input and the output fields for a section of the grating. This method simulates accurately weak and strong gratings with or without apodization and chirp. In this work, the T-matrix method will be presented for simulating gratings of fiber optic. The straightforward TMM allows high accuracy for modelling in the frequency domain, which enables analyzing if the different types and forms of realizable gratings.

TMM is a powerful modelling approach which concatenate several sections in order to discretize the grating structure. The TMM method divides the Grating structure into many uniform blocks [123]. The signal that is simulated from each block is added to the total reflected signal. TMM is based on coupled mode theory, which considers the interaction of the forward and backward propagating optical waves inside the fiber.

In this work, the matrix method is applied to the different structures of the grating in order to calculate the reflected wavelength. We will describe the matrix calculation in detail. In order to obtain the spectral response of the FBG, the transfer matrix approach is used to solve the coupled mode equations. It is the most commonly used method for simulating FBGs.

The analytical results of the coupled mode equations are the starting point of this method. The elements of the transfer matrix are obtained by solving the coupled mode theory equations and applying the appropriate boundary conditions.

The uniform grating is a special case that have an analytical solution. In this method, the grating structure is discretized into N cascaded sections and each section is described as a 2×2 matrix. Thus, the matrix outputs of one section are used as the matrix inputs of the following section. The number of sections N used in the analysis determines the accuracy of TMM. The analytical results of the coupled mode equations are the starting point of the TMM method. The elements of the transfer matrix are obtained by solving the coupled mode theory equations and applying the appropriate boundary conditions.

Two counter-propagating plane waves are confined into the fiber optic core. A uniform Bragg grating of length l and uniform period is inscribed inside the fiber. Figure 36 shows how the TMM is applied to uniform grating:

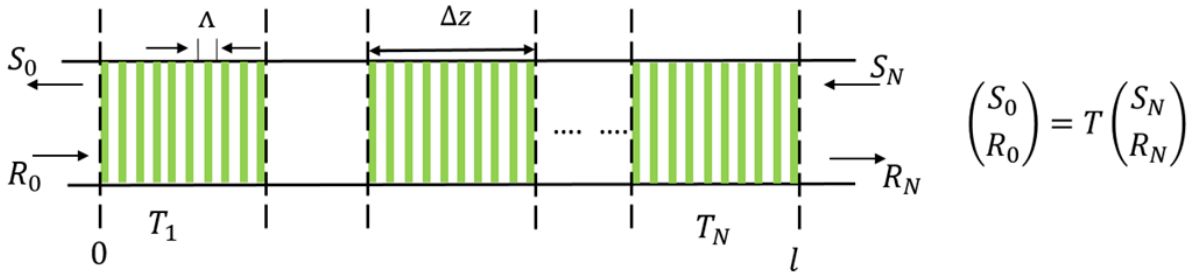

Figure 36: Illustration of T-matrix model for a uniform Bragg grating

The electrical fields of the forward and backward-propagating waves are expressed as:

$$\mathrm{E_a(z,t)} = \mathrm{R(z)}\exp[\mathrm{i}(\omega \mathrm{t} - \beta \mathrm{z})] \tag{2-15}$$

$$\mathrm{E_b(z,t)} = \mathrm{S(z)}\exp[\mathrm{i}(\omega \mathrm{t} + \beta \mathrm{z})] \tag{2-16}$$

respectively, where β is the wave propagation constant.

The coupled mode equations determines the complex amplitude $\mathrm{R(z)}$ and $\mathrm{S(z)}$ of these electric fields and are used to describe the reflection spectrum of the fiber Bragg Grating. They are expressed as follows:

$$\frac{\mathrm{dR(z)}}{\mathrm{dz}} = \mathrm{i}\hat{\sigma}\mathrm{R(z)} + \mathrm{ikS(z)} \qquad 0 \le \mathrm{z} \le l \tag{2-17}$$

$$\frac{\mathrm{dS(z)}}{\mathrm{dz}} = -\mathrm{i}\hat{\sigma}\mathrm{R(z)} - \mathrm{ikS(z)} \qquad 0 \le \mathrm{z} \le l \tag{2-18}$$

Where R(z) and S(z) are the amplitudes of forward-propagating and backward-propagating modes respectively, defined by:

$$\mathrm{R(z)} = \mathrm{A(z)exp(i\delta z - {\varphi}/{2})}$$

$$\mathrm{S(z)} = \mathrm{B(z)exp(i\delta z + {\varphi}/{2})}$$

$\widehat{\sigma}$ is the dc self-coupling coefficient given by $\delta + \sigma - \frac{1}{2}\frac{\mathrm{d}\varphi}{\mathrm{dz}}$

δ is the wave vector detuning is equal to zero for light at the Bragg grating center wavelength and is given by $2\pi \mathrm{n_{eff}}(\frac{1}{\lambda} - \frac{1}{\lambda_B})$

σ is the dc coupling coefficient given by $\frac{2\pi}{\lambda}\bar{\delta}\mathrm{n_{eff}(z)}$

φ is the phase; for unchirped FBG the parameter $\frac{1}{2}\frac{\mathrm{d}\varphi}{\mathrm{dz}} = 0$

K is the ac coupling coefficient given by $\frac{\pi}{\lambda}\upsilon\bar{\delta}\mathrm{n_{eff}(z)}$

Quantitative information about the spectral response of the FBG are obtained by using CMT. In order to get the spectral response of the FBG, we used in this work the transfer matrix method (TMM) to solve the CMEs.

Closed form solutions for $\mathrm{R(z)}$ and $\mathrm{S(z)}$ are obtained from (2-15) while assuming that both are forward and backward inputs to the Bragg grating. The boundary conditions are $\mathrm{S(0)} = \mathrm{S_0}$, $\mathrm{R}(l) = \mathrm{R_1}$.

The elements in the transfer matrix are as follows:

$$\begin{bmatrix} S_i \\ R_i \end{bmatrix} = T_i \begin{bmatrix} S_{i-1} \\ R_{i-1} \end{bmatrix} = \begin{bmatrix} T_{11} & T_{12} \\ T_{21} & T_{22} \end{bmatrix} \begin{bmatrix} S_{i-1} \\ R_{i-1} \end{bmatrix} \quad (2\text{-}19)$$

The matrix of the form T_i is a 2×2 matrix and contain information specific to one section. This matrix represents the amplitudes of forward and backward-propagating modes and is defined by [67]:

$$[T_i] = \begin{bmatrix} \cosh(S\Delta z_i) - i\frac{\Delta\beta}{S}\sinh(S\Delta z_i) & -i\frac{k}{S}\sinh(S\Delta z_i) \\ i\frac{k}{S}\sinh(S\Delta z_i) & \cosh(S\Delta z_i) + i\frac{\Delta\beta}{S}\sinh(S\Delta z_i) \end{bmatrix} \quad (2\text{-}20)$$

The elements of the transfer matrix for the i-th section are the solutions to the coupled mode equations and given by [124]:

$$\mathrm{T_{11}} = \mathrm{T^*_{22}} = \cosh(\mathrm{S\Delta z_i}) - \mathrm{i}\frac{\Delta\beta}{\mathrm{S}}\sinh(\mathrm{S\Delta z_i}) \quad (2\text{-}21)$$

$$T_{12} = T^*_{21} = -i\frac{k}{S}\sinh(S\Delta z_i) \quad (2\text{-}22)$$

where $\Delta\beta$ and k are the local values of the i-th section, Δz is the length of the section and S is defined by $\sqrt{k^2 - \Delta\beta^2}$.

In the transfer matrix, input and output fields are connected to each other. The grating structure consists of N Bragg grating segments. The N multiplied 2×2 matrices are replaced by a single 2×2 matrix. Thus, the product of all individual section transfer matrices gives the transfer matrix for the whole grating of length l.

The total grating structure can be expresses as:

$$\begin{bmatrix} S(L) \\ R(L) \end{bmatrix} = [T] \begin{bmatrix} S(0) \\ R(0) \end{bmatrix} \quad (2\text{-}23)$$

where $T = T_N * T_{N-1} * \ldots . T_i \ldots . T_1$

$S(0)$ is the boundary condition and normalized to 1 and $R(N)$ the reflected amplitude at the output of the grating is zero.

The reflection coefficient is then calculated by the relation

$$R = \frac{T_{21}}{T_{11}} \quad (2\text{-}24)$$

And the reflectivity is defined by the following equation:

$$R(L,\lambda) = \frac{k^2 \sinh^2(S\Delta)}{k^2\cosh^2(S\Delta) + i\Delta\beta^2\sinh^2(S\Delta)} \quad (2\text{-}25)$$

The reflectivity becomes

$$R(L,\lambda_B) = \tanh^2(S\Delta) \quad (2\text{-}26)$$

2.5 SIMULATION OF THE FBG REFLECTION SPECTRUM

The simulation of the spectral response of a uniform FBG is obtained by using Matlab (complete details of the code are included in Appendix B). The parameters that were chosen for the construction of FBG model and used in the simulation are listed in Table 3.

The index of refraction of the single mode fiber has a value of 1.4485 and 5.5×10^{-4} for the index difference. The length of the grating was fixed as 1 mm under unperturbed conditions.

Table 3: Parameters of the simulation

Parameters	Values
Grating length (m)	L = 1e-3
Reflected wavelength (nm)	λ = 840e-9
Bragg grating segments	N = 500
Change in the refractive index difference	Δn_{eff}= 1e-4
Bragg Grating spatial period (m)	Λ = 2.899e-7

The simulated result of the reflection spectra as a function of wavelength is shown below in Figure 37. The multiple reflections to and from the opposite ends of the grating region are responsible for the side lobes of the resonnance.

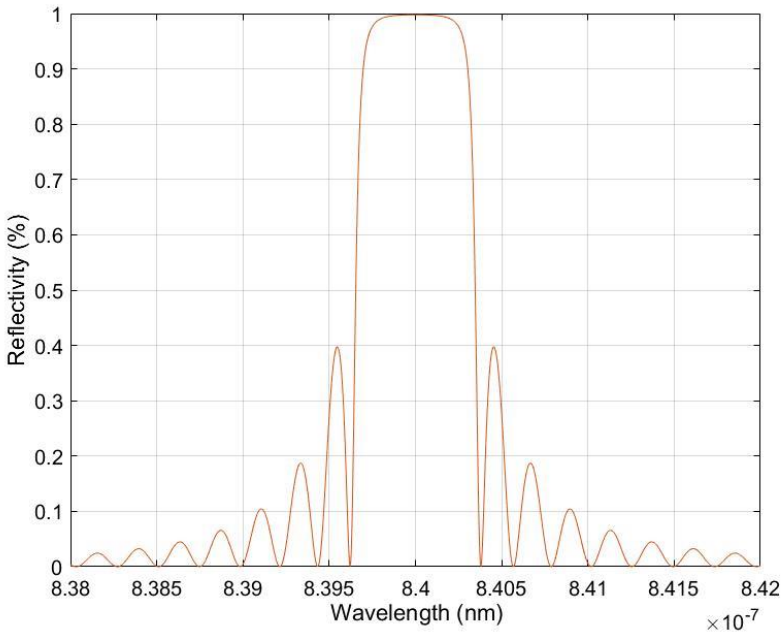

Figure 37: FBG reflection spectrum

2.5.1 Spectrum and FWHM dependence on grating length

This simulation demonstrates the spectral response of the grating due to altering the grating length. The parameters used for the simulation are listed in Table 4.

As described above the spectral response of the uniform FBG is calculated using T-matrix. The length of the grating has been varied from L= 5 mm to 40 mm. However, we assumed that the change in the index of refraction is uniform along the grating length. The reflection spectra were obtained and analysed for the different values of grating length.

Table 4: Parameters of the simulation

Parameters	Values
Grating length (m)	L = 5-40e-3
Reflected wavelength (nm)	λ = 840e-9
Change in the refractive index difference	Δn_{eff}= 1e-4
Bragg Grating spatial period (m)	Λ = 2.899e-7

From the spectra, the spectral response of a grating is altered as the length of the grating is changed. The profiles of the spectral response of a uniform FBG with different

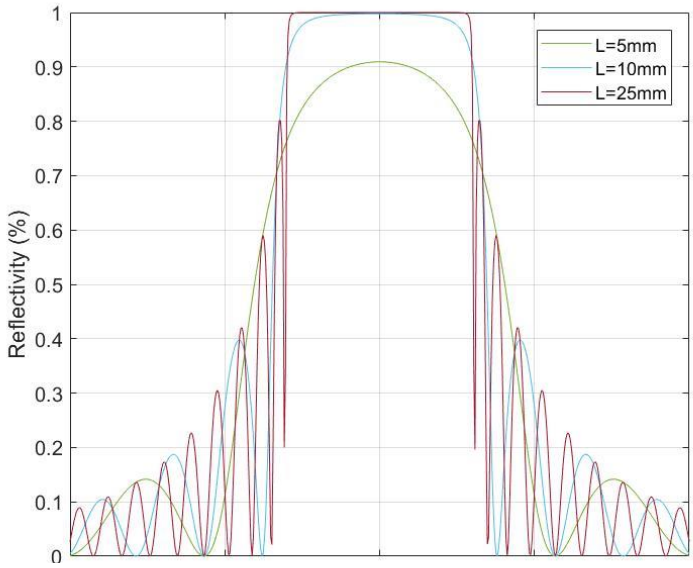

Figure 38: Spectral profile of uniform FBG with different lengths of grating

lengths 5mm, 10mm, 25mm are shown below in Figure 38. As the length of the grating increases, the bandwidth of the gratings decreased.

At L = 5mm, 10mm, 25mm, the maximum reflectivity is respectively 90.93%, 99.77%, 99.99%. The reflectivity reaches 99.99% at L=25 mm but increase in the reflectivity of side lobes. Then, if the length is incremented further, the maximum reflectivity maintains the same value of 99.99% as can be seen in Figure 39.

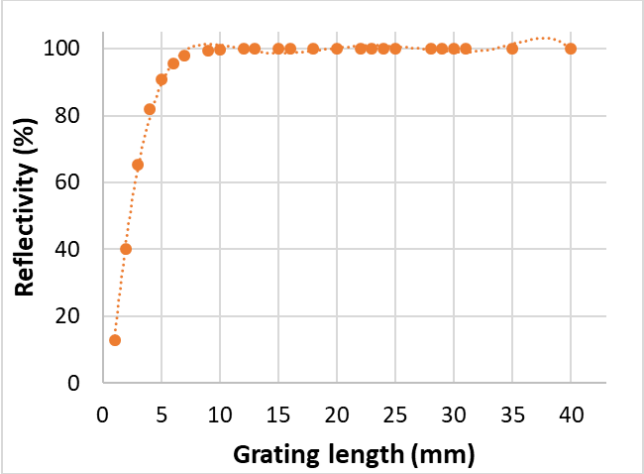

Figure 39: Relation between FWHM and grating length

In Figure 40, it can be observed that when the grating length is 1 mm with a refractive index change of 0.0001 the bandwidth is 0.188 nm. As the grating length to increases 2 mm, the bandwidth reduces to 0.128 nm. For further reduction in the index of refraction change, the bandwidth remains constant at a minimum value.

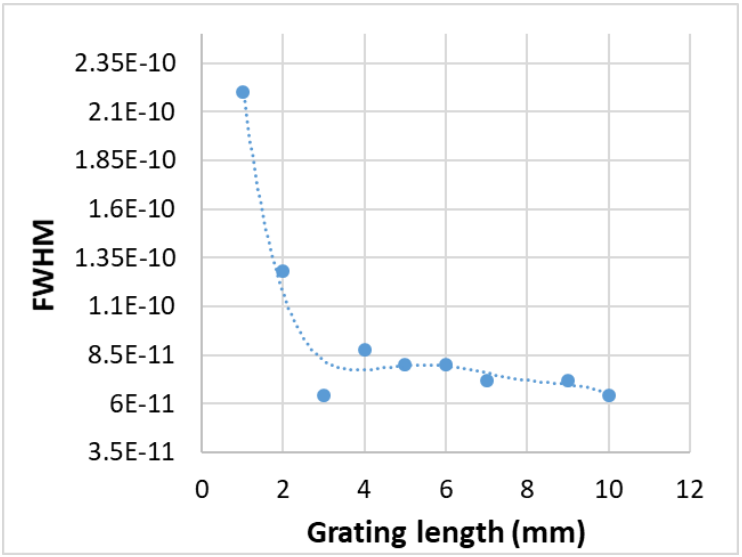

Figure 40: Relation between FWHM and grating length

2.5.2 Spectrum and FWHM dependence on refractive index change

The index of refraction changes is varied assuming a 5 mm uniform grating length in these simulations. For $\Delta n_{eff} = 5\mathrm{e}-4$ the first grating has 99.99% reflectivity and a bandwidth of 0.416 nm approximately. The parameters used for the simulation are listed in Table 5 and a set of simulations is shown in Figure 41.

Table 5: Parameters of the simulation

Parameters	Values
Grating length (m)	L = 5e-3
Reflected wavelength (nm)	λ = 840e-9
Change in the refractive index difference	Δn_{eff}= 1e-5 _2.5e-4
Bragg Grating spatial period (m)	Λ = 2.899e-7

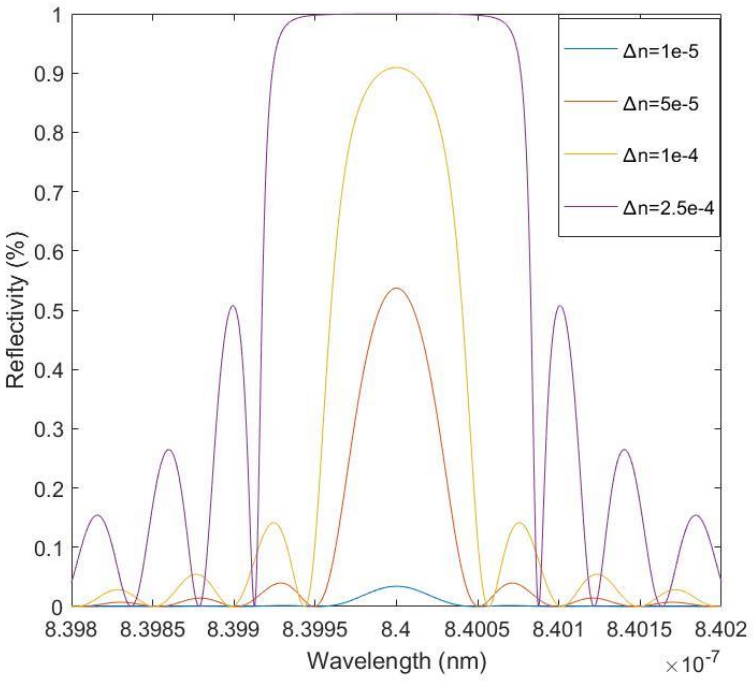

Figure 41: Variation of reflectivity due to index of refraction changes

A reflectivity of 90.93 % is obtained for an index of refraction change of $\Delta n_{eff} = 1\mathrm{e} - 4$. For $\Delta n_{eff} = 5\mathrm{e} - 5$ the reflectivity is reduced to 53.71%. The reflectivity decreased to 19.02 % by reducing the change of the index of refraction to $\Delta n_{eff} = 2.5\mathrm{e} - 5$ as shown in Figure 42.

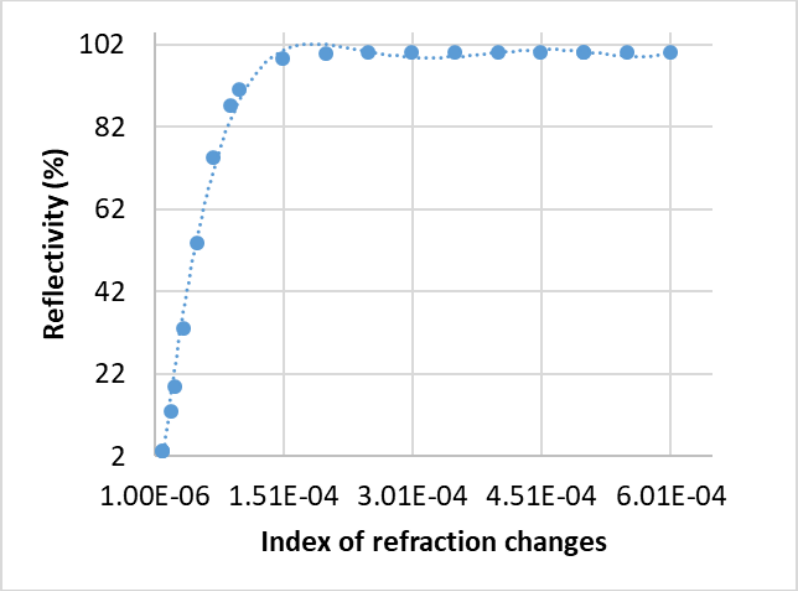

Figure 42: Variation of reflectivity due to index of refraction changes

The dependence of bandwidth on grating length and refractive index change was analysed. The parameters used for the simulation are listed in Table 6.

Table 6: Parameters of the simulation

Parameters	Values
Grating length (m)	L = 1 e-3
Reflected wavelength (nm)	λ = 840e-9
Change in the refractive index difference	Δn_{eff}= 1e-4
Average refractive index	n_{eff} = 1.447
Bragg Grating spatial period (m)	Λ = 2.899e-7

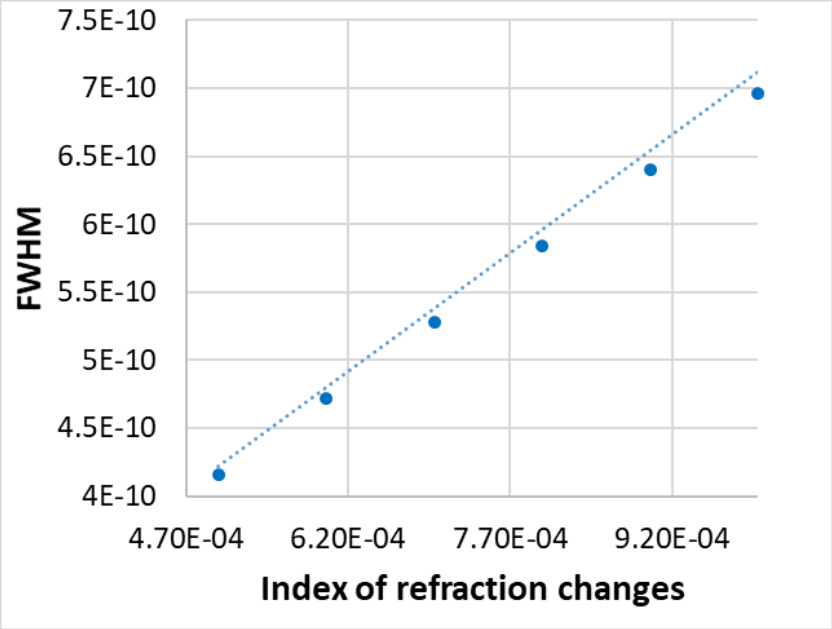

Figure 43: Relation between FWHM and index change

It can be seen that the increase in grating length reduces the bandwidth. However, the bandwidth increases with the increase in change in refractive index of the FBG. In addition, the strength of the side lobes in the reflection spectrum increases with the increase in the grating length and the change in refractive index as indicated in Figure 38 and Figure 41. The side lobes are undesirable because they could cause interference between channels. A method called apodization can be used to supress these side lobes.

2.5.3 Temperature sensing

FBGs are capable of measuring temperature and multidimensional strain fields. The measurements of these factors are critical for monitoring the rotating electrical machine. This study will focus on the temperature and strain sensing capabilities of FBGs. This part represents the analysis of FBG sensor's response under temperature and strain fields.

2.5.3.1 Thermo-optical model of the temperature effect on FBG

The changes of the index and the grating period in the FBG due to thermal effect induce a shift in the Bragg wavelength.

The new index of refraction can be written as:

$$n_{eff2} = n_{eff1} + (dn_{eff} / \mathrm{dT})\ \Delta \mathrm{T} \qquad (2\text{-}27)$$

The new period of the grating element can be expressed as:

$$\Lambda_2 = \Lambda_2(1 + \alpha\Delta T) \quad (2\text{-}28)$$

The temperature distribution obtained from equations (2-27) and (2-28) was integrated with the TMM relations. The reflectivity spectrum of the FBG due to the thermal effect was obtained.

The variation in the Bragg wavelength could be written as:

$$\Delta\lambda_b = \lambda_b(\alpha + \xi)\Delta T \quad (2\text{-}29)$$

The thermal expansion coefficient is approximately equal to 0.55e-6 °C^{-1} for the germanium doped silica core fiber and the thermo-optic coefficient is 8.6e-6 °C^{-1}.

The simulation of the spectral response of a uniform FBG is obtained by using Matlab (complete details of the code are included in Appendix B). The parameters that were chosen for the construction of FBG model and used in the simulation are listed in Table 7.

The index of refraction has a value of 1.46 and 0.0002 for the index difference. The length of the grating was fixed as 1 mm under unperturbed conditions.

Table 7: Parameters of the simulation

Parameters	**Values**
Grating length (m)	L = 1e-3
Reflected wavelength (nm)	λ = 840
Average refractive index	n_{eff} = 1.447
Change in the refractive index difference	Δn_{eff}= 1e-3
Bragg Grating spatial period (nm)	Λ = 290
Thermo-optical coefficient (1/K)	dn/dT = 8.6e-6
Coefficient of thermal expansion (1/K)	α = 4.1e-7
Temperature change (K)	ΔT = 293.15:25:373.15

2.5.3.2 *Simulated spectrum of the FBG under thermal effect*

From the thermal analysis performed on MATLAB, we were able to study the effect of the temperature changes on central wavelength of the FBG sensor. The dependence of temperature on FBG reflection spectrum was observed and analyzed. Figure 44 displays the total reflectivity spectra including combined effects of the thermal expansion and thermo-optic changes with temperature. (Complete details of the code are included in Appendix B).

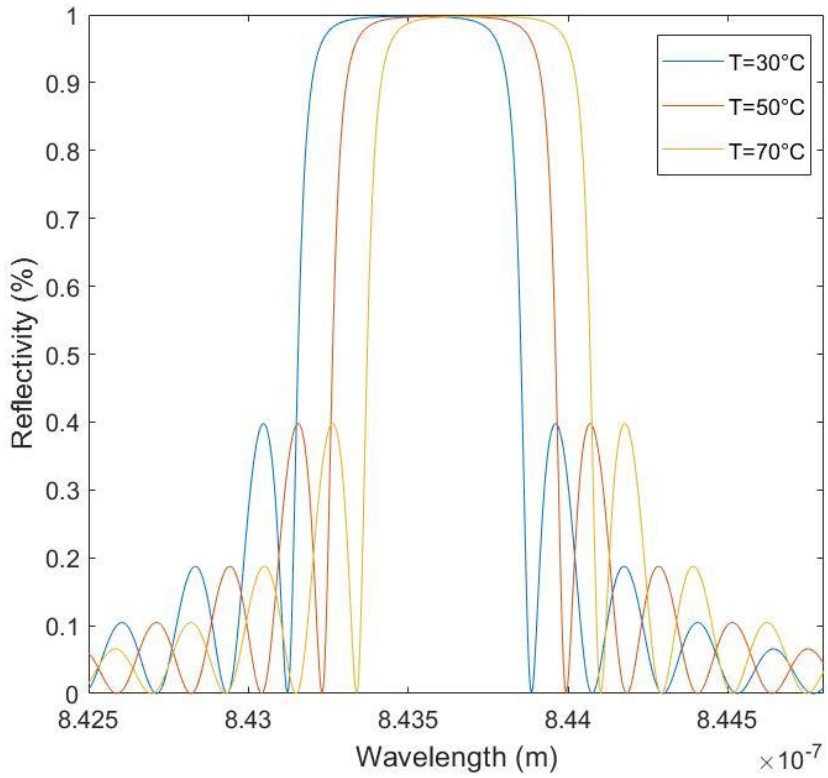

Figure 44: Thermally induced Bragg wavelength shifts in FBG

The central wavelength values of an FBG with different temperatures were calculated from Figure 44 and plotted in Figure 45. It can be seen that when the temperature increased, the Bragg grating wavelength shifted positively. The corresponding wavelength peak are plotted in Figure 45.

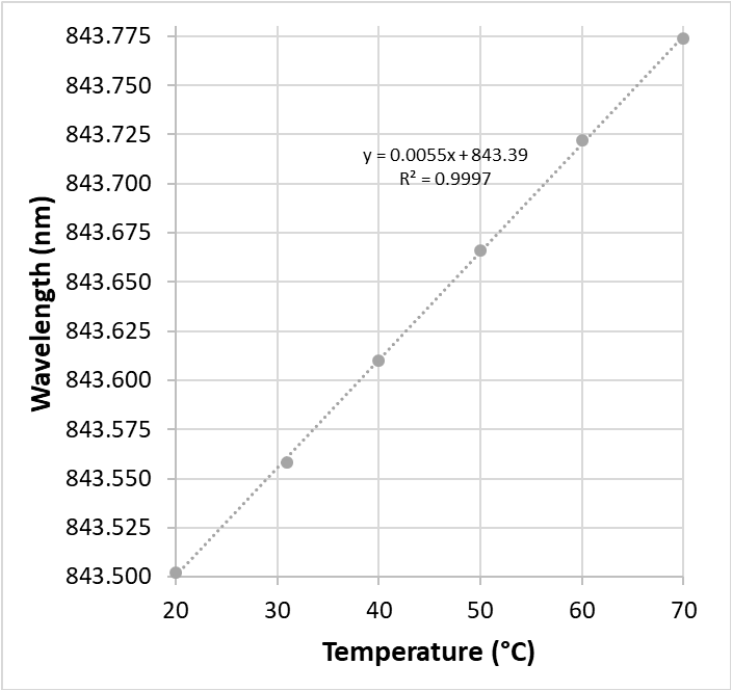

Figure 45: Shift in the Bragg wavelength as a function of temperature

The data is linear and the results of the linear regression reveal a change in Bragg grating wavelength due to a change in temperature that results in a thermal sensitivity of 5.5 pm/°C.

2.5.4 Longitudinal strain sensing

2.5.4.1 Model of the longitudinal strain effect on FBG

Strain is the ratio of the applied stress to the Young's modulus of the material. When a material is stressed, its physical length increase. This fractional increase is the strain. The wavelength shift of the FBG sensor determines the strain variation in the grating portion.

The simulation results of the FBG sensors subjected to linear or uniform strain obtained by TMM method are accurate enough [125].

Yamada et al. were the first to simulate the reflected spectrum of the FBG under a uniform strain fields [126]. After, this theory was developed to simulate the reflected spectrum under different grating forms and strain types [127],[128],[129],[130].

The Bragg wavelength is calculated as:

$$\lambda_b = 2n_{eff}\Lambda \tag{2-30}$$

Where n_{eff} is the effective index of the core mode and Λ is the spatial period of the modulation.

The core refractive index changes are related to the strain and given by:

$$n_{eff}{}' = n_{eff} - \frac{{n_{eff}}^3}{2}\varepsilon[p_{12} - \nu(p_{11} + p_{12})] \tag{2-31}$$

Where $n_{eff}{}'$ is the modified refractive index, ε is the axial strain along the fiber and ν is the Poisson's ratio and p_{11} and p_{12} are the light-elastic coefficient of the fiber

The grating period is given by:

$$\Lambda' = \Lambda[1 + (1 - P)\varepsilon] \tag{2-32}$$

Where Λ' is the modified grating period and P is the effective strain optic coefficient.

The Bragg wavelength will become:

$$\lambda_b = 2n_{eff}{}'\Lambda' \tag{2-33}$$

The variation in the Bragg wavelength is as follows:

$$\lambda_b{}' = \lambda_b(1 - P)\varepsilon \tag{2-34}$$

Where $\lambda_b{}'$ is the Bragg wavelength shift, ε is the applied strain on the longitudinal axis of the grating, P is the effective strain optic constant given by

$$P = \frac{{n_{eff}}^2}{2}[p_{12} - \nu(p_{11} + p_{12})] \tag{2-35}$$

According to this equation the wavelength shift is proportional to the axial strain of the fiber. The parameters that were and used in the simulation are listed in Table 8.

Table 8: Parameters of the simulation

Parameters	Values
Grating length (m)	L = 5e-3
Reflected wavelength (nm)	λ = 840
Average refractive index	n_{eff} = 1.447
Change in the refractive index difference	Δn_{eff} = 1e-4
Fiber diameter (cm)	D = 9e-3
Effective strain optic coefficient (ε)	P = 0.218
Strain acting on the FBG (ue)	10 _ 90e-6

2.5.4.2 Simulated spectrum of the FBG under longitudinal strain

The reflected spectrum was inspected and results in a linear relationship between the applied load and the measured strain. The dependence of the shift of the resonance wavelength of the FBG on the increasing strain was measured to be 0.7 pm/ με. Figure 46 shows the strain response of the silica FBG when strain value was applied. As illustrated in this figure, when the strain increased, the Bragg grating peak shifted to the long wavelength side. The wavelength shifts results due to applied strain for an 840 nm Bragg grating is shown in Figure 46.

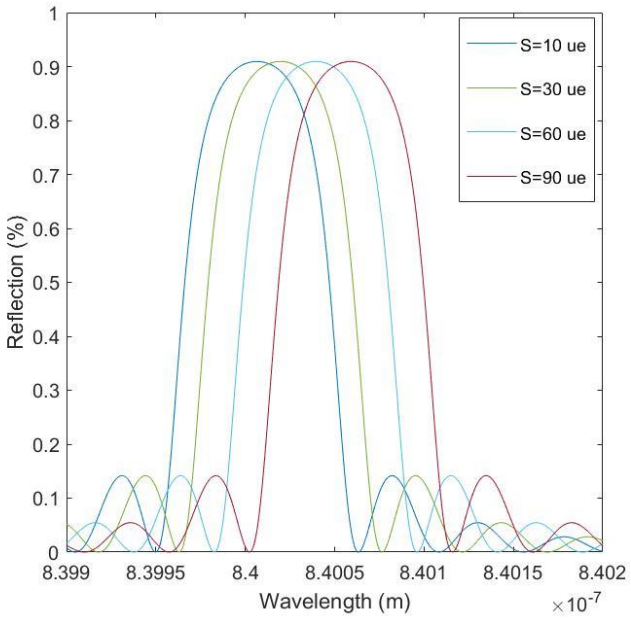

Figure 46: Bragg wavelength spectrum shift induced by axial strain in FBG

The corresponding wavelength shifts are plotted in Figure 47. The data is linear and the results of linear regression, shown in Figure 47, reveal strain sensitivity of the silica FBG to be 0.7 pm/ με. This is similar to the value for silica fibre, which is 1.15 pm/με at this wavelength [112].

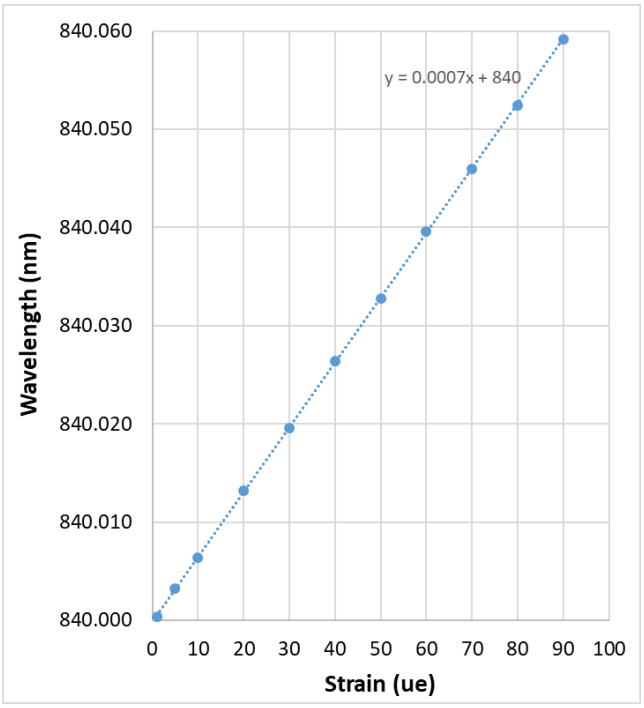

Figure 47: Bragg wavelength shifts induced by axial strain in FBG

2.5.5 Local transverse strain sensing

In this work, we investigate the polarization effect of transverse perturbation on an FBG. We studied the FBG reflection spectrum characteristics under the application of a transverse load.

2.5.5.1 Model of the transverse force effect on FBG

The Force F that acts on a local position of the grating changes the waveguide characteristics of this section and thus in the reflection spectrum.

The stress of the fiber grating is as follows in the three directions [131]:

$$\sigma_x = \frac{2\times F}{\pi\times L_2\times D} \tag{2-36}$$

$$\sigma_y = \frac{-6\times F}{\pi\times L_2\times D} \tag{2-37}$$

$$\sigma_z = \nu(\sigma_x + \sigma_y) = \frac{-4\nu\times F}{\pi\times L_2\times D} \tag{2-38}$$

Where ν is the fiber Poisson's ratio, F is the transverse force, L_2 is the grating length and D is the fiber diameter.

The Bragg grating is not isotropic if the applied strain is not isotropic. The strain field present in the fiber optic will induce a difference in the refractive index along its two transversal axes. This index difference along the two transversal axes of the fiber will form two different polarization modes of the propagating light. The axes are called the slow axis and the fast axis of the fiber since the phase velocities in both modes are different, which make one mode faster than the other one.

As the applied strain is not isotropic, the change in the refractive index is highly polarization dependent. The fiber deformation produces birefringence and changes the cross sectional refractive index because the light elastic coefficients vary.

At the presence of the disturbance, the refractive index change of x- and y-polarizations of the grating zone are as follows [131]:

$$(\Delta n_{eff})_x = \frac{-{n_{eff}}^3}{2E}[(p_{11} - 2\nu p_{12})\sigma_x + [(1-\nu)p_{12} - \nu p_{11}](\sigma_y + \sigma_z)] \tag{2-39}$$

$$(\Delta n_{eff})_y = \frac{-{n_{eff}}^3}{2E}[(p_{11} - 2\nu p_{12})\sigma_y + [(1-\nu)p_{12} - \nu p_{11}](\sigma_x + \sigma_z)] \tag{2-40}$$

Where p_{11} and p_{12} are the light-elastic coefficient of the fiber, ν is the fiber Poisson's ratio, E is the Young's modulus , σ_x, σ_y and σ_z, are the stress components acting on the FBG in x, y and z direction respectively.

The reflected light from the Bragg grating is also different for both modes. Therefore, two different conditions for two distinct modes arise as shown in the following equations:

$$(\frac{\Delta\lambda_B}{\lambda_B})_x = \varepsilon_3 - \frac{{n_{eff}}^2}{2}[p_{11}\varepsilon_1 + p_{12}(\varepsilon_2 + \varepsilon_3] \quad (2\text{-}41)$$

$$(\frac{\Delta\lambda_B}{\lambda_B})_y = \varepsilon_3 - \frac{{n_{eff}}^2}{2}[p_{11}\varepsilon_2 + p_{12}(\varepsilon_1 + \varepsilon_3)] \quad (2\text{-}42)$$

The applied transverse and non-isotropic load induces birefringence on the FBG. The reflectivity of the disturbed FBG is obtained by following the same methodology and analogy used in section 2.4.2.

$$R(L,\lambda) = R_x(L,\lambda) + R_y(L,\lambda) \quad (2\text{-}43)$$

$$R_x(L,\lambda) = \frac{{k_x}^2 \sinh^2(S_x\Delta)}{{S_x}^2\cosh^2(S_x\Delta)+i\Delta{\beta_x}^2\sinh^2(S_x\Delta)} \quad (2\text{-}44)$$

$$R_y(L,\lambda) = \frac{{k_Y}^2 \sinh^2(S_y\Delta)}{{S_y}^2\cosh^2(S_y\Delta)+i\Delta{\beta_y}^2\sinh^2(S_y\Delta)} \quad (2\text{-}45)$$

Where $\Delta\beta_x$ and $\Delta\beta_x$ are the phase mismatching for x- and y- polarizations, respectively, and are given by:

$$\Delta\beta_x = 2\pi n_{eff}(\frac{1}{\lambda} - \frac{1}{\lambda_{Bx}}) \quad (2\text{-}46)$$

$$\Delta\beta_y = 2\pi n_{eff}(\frac{1}{\lambda} - \frac{1}{\lambda_{By}}) \quad (2\text{-}47)$$

Two Bragg peaks will be visible in the reflected spectrum instead of one Bragg reflection peak. The reflection spectra of the FBG subjected to a transverse load along the y-axis is depicted in Figure 48.

In our simulation, we used the transfer matrix method to implement the spectral simulation of FBG under local transverse force model. The FBG is divided into 3 parts. The first part has the transfer matrix M_1 and its length is L_1. The second part has the transfer matrix M_2 and its length is L_2. The third part has the transfer matrix M_3 and its length is L_3.

$$\begin{bmatrix} R(L) \\ S(L) \end{bmatrix} = M_3 * M_2 * M_1 \begin{bmatrix} R(0) \\ S(0) \end{bmatrix} \quad (2\text{-}48)$$

The spectral response is a function of the affected region of the FBG and the part of FBG under transverse load is considered very small regarding the total length of the FBG.

The second transfer matrix becomes:

$$[M_2] = \begin{bmatrix} \cosh(S_x \Delta z_2) - i\frac{\Delta\beta_x}{S_x}\sinh(S_x \Delta z_2) & 0 \\ 0 & \cosh(S\Delta z_2) + i\frac{\Delta\beta_x}{S_x}\sinh(S\Delta z_2) \end{bmatrix} \quad (2\text{-}49)$$

Where

$$S_x = \sqrt{k^2 - \Delta\beta_x{}^2}\,,\ \Delta\beta_x = \frac{2\pi(\Delta n_{eff})_x}{\lambda} \text{ and } S_y = \sqrt{k^2 - \Delta\beta_Y{}^2},\ \Delta\beta_y = \frac{2\pi(\Delta n_{eff})_y}{\lambda}$$

In this case, we present results for x-polarized light. We consider that the transverse force affects a small region of the grating (l=0.1 mm) and a 4 mm long FBG was studied, see Table 9.

Table 9: Parameters of the transverse strain simulation

Parameters	**Values**
Grating length (m)	L = 14.4e-3+3e-6+15.3e-3 = 0.029703 (29 mm)
Grating length affected by transverse load (m)	dz2 = 1e-6
Reflected wavelength (nm)	λ = 840e-9
Average refractive index	n_{eff} = 1.46
Change in the refractive index difference	Δn_{eff}= 5e-4
Fiber diameter (cm)	D = 125e-3
Poeckels coefficients	p11 = 0.113 p12 = 0.252
Young's modulus (N/m^2)	E = 72e+10
Poisson's ratio	ν = 0.17

Stress components acting on the FBG	sigma_x // sigma_y // sigma_z

In this work Matlab codes are written to analyse the FBG sensor under transverse strain. FBG reflection spectrum under transverse load along the x-axis is depicted in Figure 48.

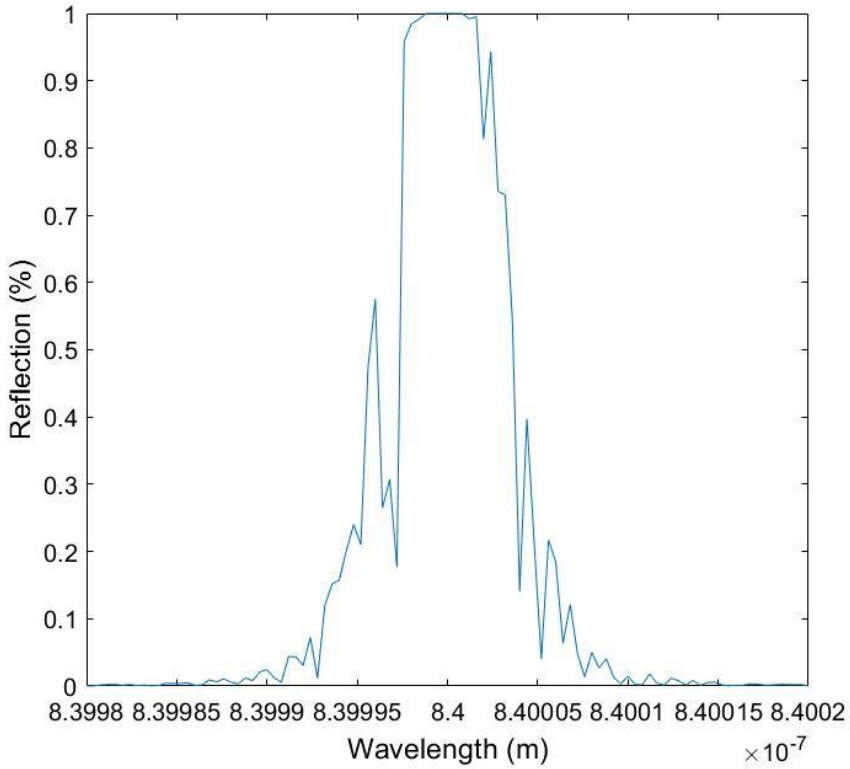

Figure 48: FBG reflection spectrum under transverse load for x-polarized light

2.5.5.2 Simulated spectrum of the FBG under transverse strain

In this simulation we assume the fiber axis is parallel to the z-direction and the force is applied in the y-axis, which yields from (2-37) $(\Delta n_{eff})_x > (\Delta n_{eff})_y$. Results for x-polarized light will be presented in this case. The affected region of the grating is small (l = 0.001 mm). The calculated spectra for various forces applied to a region of the grating is shown in Figure 49. Matlab code is written to analyse the FBG sensor under various transverse strain.

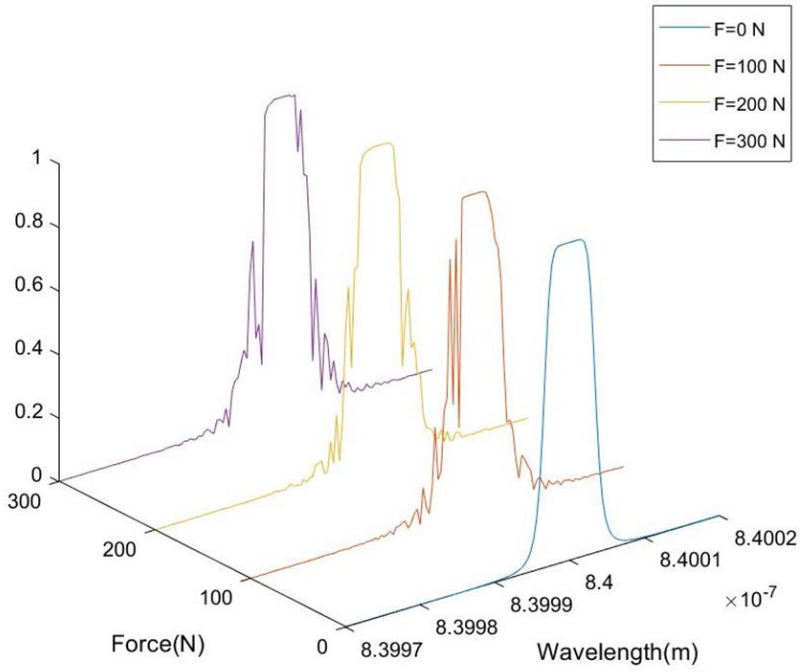

Figure 49: FBG reflection spectrum under various transverse load

The spectrum splits in two peaks at the Bragg reflection wavelength. The reflection spectrum of the FBG changes because its refraction index changes under transverse force. The pressure produces an intra-grating structure and its position is a function of the position of the applied force. When we press the grating in a position different from the center, the intra-grating structure is not very deep. The pressed grating part divides the original grating distribution into two parts that interfere, which causes a broadened reflection spectrum.

2.6 CONCLUSION

In this chapter a literature review of the different methods for grating simulation was presented. The behavior of Bragg gratings in the optical fibers have been described by using many models. Different techniques exist for simulating the Bragg grating behavior. However, each technique has a different degree of complexity. The coupled mode technique is applied to solve the wave-propagation equations by assuming weak guidance. The counter-propagating fields inside the Bragg grating structure are related by coupled differential equations. The straightforward numerical integration of the coupled mode theory is the simplest method. The FBG has a specific refractive index modulation and period. It has an analytical solution and modeling of the transfer characteristics of the FBG becomes a simple matter with the application of a fast technique called TMM. T-matrix formalism was used to solve the coupled-mode equations of the Bragg grating structure in order to obtain its spectral response. This method is capable of simulating accurately the transfer function.

Then, the simulation of uniform Fiber Bragg Grating using T-matrix formalism was presented. The T-matrix is a fast and accurate technique that calculates the input and output fields of a section of the grating. Therefore, the outputs of the first matrix were used as an input for the second matrix. The entire profile grating is modeled by continuing this process.

The uniform fiber Bragg grating was presented in this chapter. The properties of this simplest type of grating are explained using the coupled mode theory. The properties of the fiber Bragg Grating are mainly affected by the external parameters such as the strain that is applied to the grating and/or the temperature of its environment. In the context of this work, this method was capable of accurately simulating the reflectivity of the uniform FBG. However, this method is capable of simulating both strong and weak gratings with or without apodization and chirp.

The simulation showed that as the induced index of refraction increases, the reflectivity increases. Similiraly, the reflectivity also increases as the length of the grating increases. In addition, the bandwidth FWHM dependence on grating length and refractive index change was analyzed. The increase in the grating length of the FBG reduces the bandwidth. However, the increase of the refractive index of the FBG increases the bandwidth.

Using simulation, it was possible to study fiber Bragg grating sensors responses for strain and temperature measurement. The results of the simulation of the temperature and strain response were presented. The reflected spectrum was inspected and results in a linear relationship between the applied temperature and the measured wavelength. The temperature dependence of the fiber Bragg grating showed a shift towards positive wavelengths. The dependence of the shift of the wavelength of the FBG on the increasing temperature was measured to be 5.5 pm/ °C.

Additionally, From the simulation results it has been observed that perturbation such as strain (axial or transversal) applied on FBG will cause shift in the grating pitch and therefore a shift in the centre wavelength. The strain dependence of the fiber Bragg grating showed that the strain sensitivity of the silica FBG is 0.7 pm/με.

When a transverse load was applied, the spectral response showed that the FBG spectral behaviour changes. Varying the strain we observed that the reflection spectrum of the FBG splits in two peaks at the Bragg reflection wavelength. Applying any transverse load causes changes in the refraction index changes of the fibre. The pressure produces an intra-grating structure and its position is a function of the position of the applied force.

We have performed the simulation of the transverse strain in order to predict the behavior of the Bragg grating due to a transverse strain. According to the simulaiton, the splitting of the peak in the reflected spectrum of the Bragg grating during the rotation of the fiber is due to transverse strain. In the next chapter, we will measure the experimental sensitivity and compare it to the simulated one in order to validate the simulation.

CHAPTER 3

EXPERIMENTAL CHARACTERSATION AND CALIBRATION OF THE FBG TEMPERATURE SENSOR

3.1 INTRODUCTION

In chapter 3, the results of the characterization of the purchased FBG sensor are presented. First, this chapter gives a detailed description about the characteristics of the optical system components such as the optical source, the FBG and the optical spectrometer that are used in our experiments.

Secondly, the setup and procedure used in this work in order to achieve our main goals are the following: The first experimental part, which is a static experimental measurement, aims at coupling light from the super-luminescent diode (SLD) into the FBG, including the study of the injection losses in the FBG. In the second experimental part, special emphasis is given to the thermal calibration method of the FBG and its characterization.

The goal here is to experimentally characterize and validate the temperature variation measurement using the FBG sensor. We will calibrate the sensor and determine its sensitivity and finally compare the experimental results to the simulated ones as presented in the previous chapter.

3.2 OPTICAL SYSTEM COMPONENTS DESCRIPTION

3.2.1 Optical sources parameters

Factors that are related to the source choice differ widely between different types of sensors. These source factors will affect the operation of a sensor. Two basic functions of the illumination sources should be considered. Firstly, the sources must provide sufficient light intensity over the appropriate wavelength region. In addition, they must regulate light intensity over the needed period of using the device. The choice should be made taking into account the intensity, the spectral bandwidth, the degree of collimation and the monochromaticity.

A wide variety of optical sources can be utilized to illuminate optical fiber sensors devices with the association of appropriate detector. The selection of the type of illumination depends upon several constraints. For example, the nature of the signal processing, the accuracy required and the spatial constraints.

3.2.2 Super-luminescent diode source

The availability of suitable optical sources influences the price of a particular sensing device. The sensing device have to be required at an acceptable cost.

There are several factors that influence the choice of the sources. Their size, the output power, the output power stability, the spatial quality of the beam, its lifetime, the coupling of light into the optical fibers, its spectral characteristics, the associated electrical driver and the maintenance.

In addition, there is the heating problem of some light sources. This represents an obstacle for optical fiber sensor devices where a compact system is needed.

The used SLD-381-MINIBUT (SUPERLUM company) source is an edge-emitting diode that provides sufficient output power for our experimental setup. Broadband source can be used such as the amplified spontaneous emission from a fiber amplifier.

A 50:50 splitter or a circulator are necessary to get the reflected wavelength. The signal that corresponds to the wavelength reflected from the grating is detected by a spectrometer. Figure 50 shows the spectrum of the SLD source, which is used to couple light into the fiber.

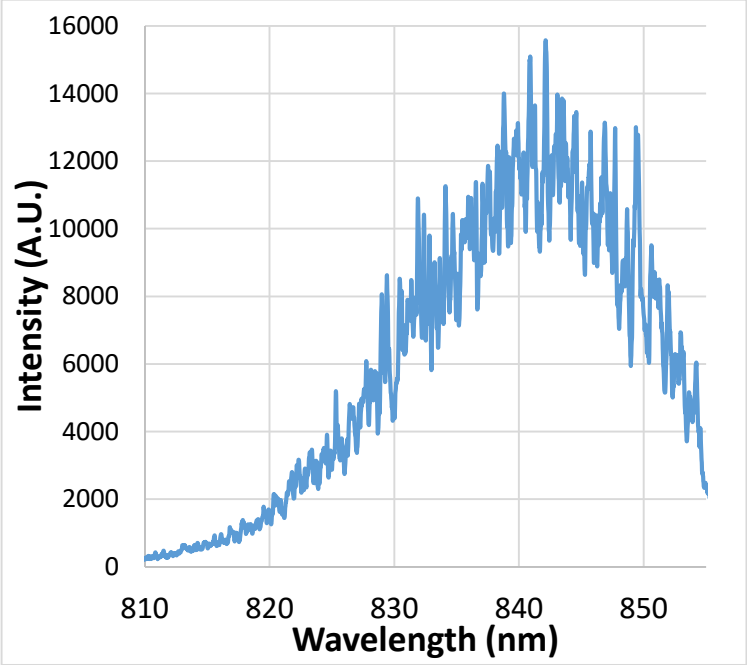

Figure 50: Spectrum of the SLD source

A zoom on the zone of interest that corresponds to the wavelengths around the central wavelength of the used FBG is shown in Figure 51.

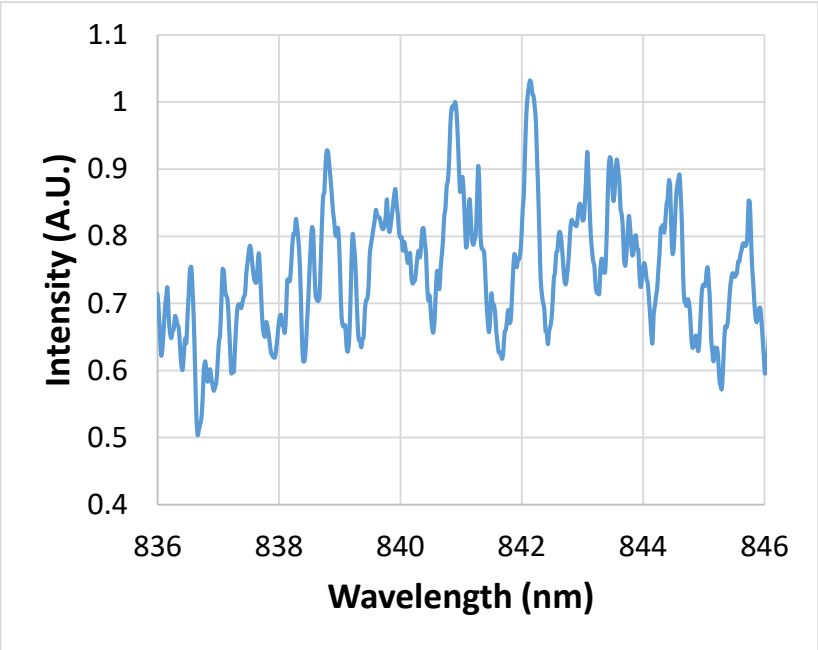

Figure 51: Zoom of the spectrum on the zone of interest

3.2.3 FBG design layout

Two Bragg Gratings are written into a single mode optical fiber that have a length of 1.5 m, which was on both ends terminated by FC/APC (angled polished connector) connectors. The fiber with two gratings per sample were fabricated by Optromix company, see Figure 52. The Bragg wavelengths were asked to be 785.06 nm and 843.51 nm with a tolerance of +/- 0.1 nm. The peak separation of the two grating is large enough in order to process data.

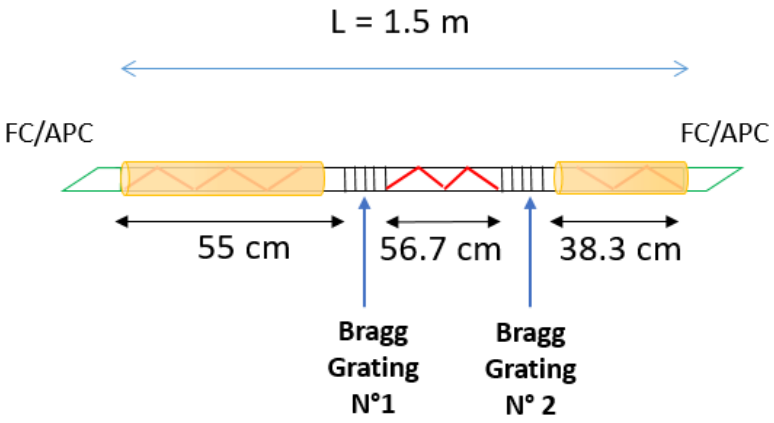

Figure 52: Two Gratings inscribed into the optical fiber of 1.5 m length

The characteristics of the fiber Bragg Grating are listed in Table 10.

Table 10: Characteristics of the customized silica fiber Bragg Grating

FBG Central wavelength	Bragg Grating #1: 785.06 nm Bragg Grating #2: 843.509 nm
FBG sensitivity	7 pm / °C
Fiber length	1.5 m
Core diameter	4.4 µm
Numerical Aperture	< 0.1
Reflectivity	50 %
Bragg Grating's position along the fiber	Positon [FBG1 , FBG 2]: 55 cm, 111.7 cm
Connectors type on both ends	FC/APC
FBG length	2-3 mm
FBG section on the fiber	Without loose tube
Acceptable radius of Curvature	1.5 cm

By using an FC/APC connector, the fiber is polished at an angle of 8 degrees, therefore the light reflection on the fiber front end does not return to the light source nor to the detector. In fact, this angle propels light into the coating of the fiber, which avoids affecting the performance of the light source and the background noise of the photodetector.

3.2.4 Spectrometer (Ocean optics HR4000)

The HR4000 is an optical spectrometer module. It performs full spectral measurement of the Bragg wavelength. This allows for precise measurement and good resolution (50 pm). Data such as the spectrum of the Bragg reflection is sampled at a rate of 10 Hz. It also comprises a software package for data acquisition. The HR4000 was connected to the computer by an Ethernet cable and results viewed in the Ocean View program. The recorded data for each measurement was saved as a .text file on the computer for further processing.

As shown in Figure 53, the light enters the optical bench through the SMA connector (1) that secures the input fiber to the spectrometer. Then it passes through the slit (2), filter (3) and then reflects off the collimating mirror (4) which focuses the light entering the optical bench towards the grating (5) of the spectrometer. The grating diffracts light from the collimating mirror and directs the diffracted light onto the focusing mirror. The focusing mirror (6) receives light reflected from the grating and focuses the light onto the CCD detector (8). The CCD detector collects the light received from the focusing mirror and converts the optical signal to a digital signal. Each pixel on the CCD detector responds to the wavelength of light that strikes it, creating a digital response. The spectrometer then transmits the digital signal to the spectrometer Ocean View application.

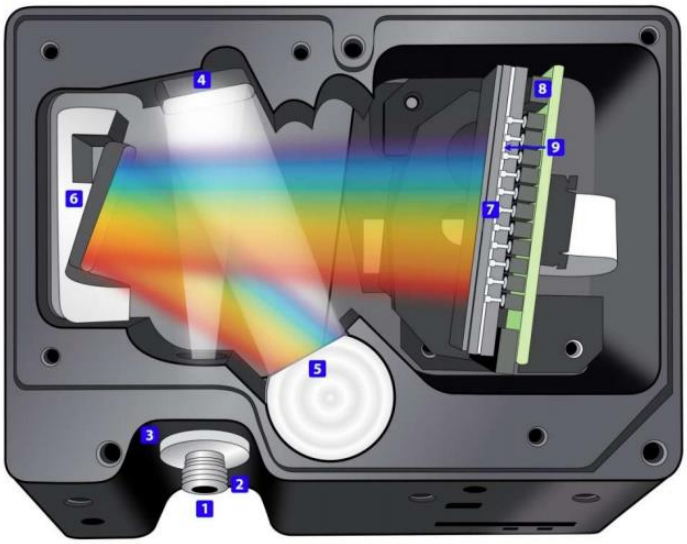

Figure 53: Diagram of how light moves through the optical bench of the spectrometer

Changing the resolution is possible if the width of the output slit is changed. The advantage of the spectrometer is the large wavelength range of 80 nm (775-852 nm), the theoretical resolution of 0.05 nm and the integration time of 3.8 ms. The spectrometer is a good option for characterizing the spectrum of the fiber Bragg grating. It takes time to do accurate measurements that depends on the wavelength range, the resolution and the averaging. It is suitable for dynamical interrogation measurements.

3.3 EXPERIMENTAL CHARACTERISATION

In this experiment, we will couple light from the super-luminescent diode (SLD) into the FBG in order to study the injection losses in the FBG. Then, we will calibrate the FBG.

3.3.1 Spectrum of the silica FBG (Measurement and characteristics)

A super-luminescent diode source was used to interrogate the Silica FBG. The output fiber was connected to a 3dB circulator with a central wavelength of 840 nm and the light was injected into the FBG. The light reflected from the silica FBG was coupled back through the 3dB circulator then to an F280APC-780 collimator (f = 18.40 mm, NA = 0.15, collimated beam diameter: 4.05 mm) and finally to the HR4000 optical spectrometer. The optical spectrometer is used for fast monitoring of the FBG. The single mode fibers are used with FC/APC connectors.

The scheme of coupling light from an SLD source is shown in Figure 54. A broadband light travels through the optical fiber then enters into the FBG. One specific wavelength, depending on the Bragg period, is reflected back by the grating.

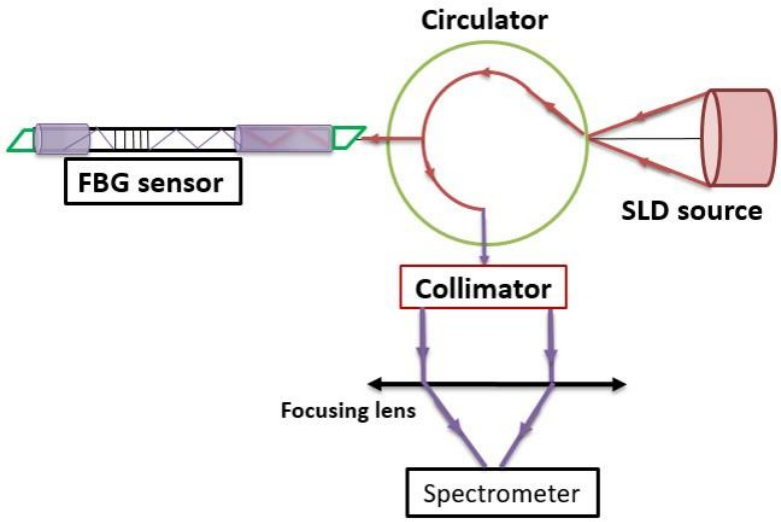

Figure 54: Schematic diagram of the measurement of the reflection spectrum of the FBG

The reflection spectrum of the silica FBG is shown in Figure 55. The bandwidth and the FWHM (Full Width at Half Maximum) at the reflected central wavelength are identified in Figure 55. The central wavelength of the reflection grating is at 843.51 nm. Full width at half maximum is an important parameter of the FBG. The bandwidth is the distance between the noise level either side of the Bragg wavelength.

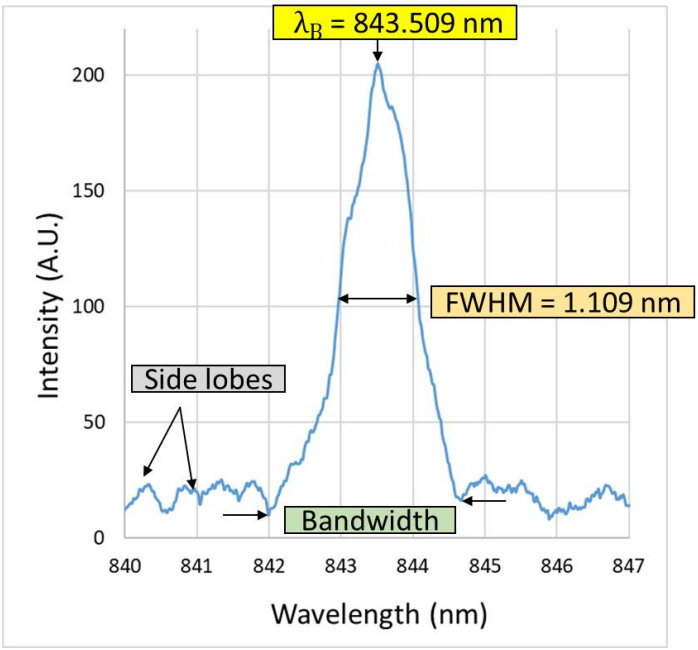

Figure 55: Spectrum of the Bragg grating

3.3.2 Power measurements

A series of experimental measurements were done in order to know the FBG losses. First, the super-luminescent diode (SLD) was connected to the FBG in order to couple the light. The light transmitted from the silica FBG was coupled directly to the photodetector. An optical power of 1 mW is measured at the output of the FBG when an optical power of 3 mW was injected, see Figure 56. The transmission loss is 4.7 dB.

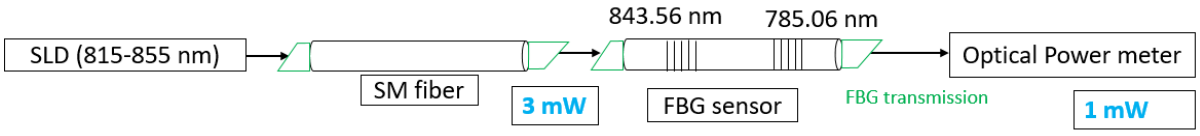

Figure 56: SLD coupling without circulator

Then, the broadband light is coupled into the optical fiber circulator and propagates from port 1 through port 2 to the FBG and the Bragg wavelength is reflected back as shown in Figure 57.

The Bragg wavelength goes from port 2 to port 3 of the fiber optic circulator and is detected using the spectrometer.

An optical power of 0.018 mW is reflected back and 0.5 mW is transmitted through the fiber for an incident optical power at the fiber input of 0.7 mW. The transmission loss is 7.78 dB and the reflection loss is 22 dB.

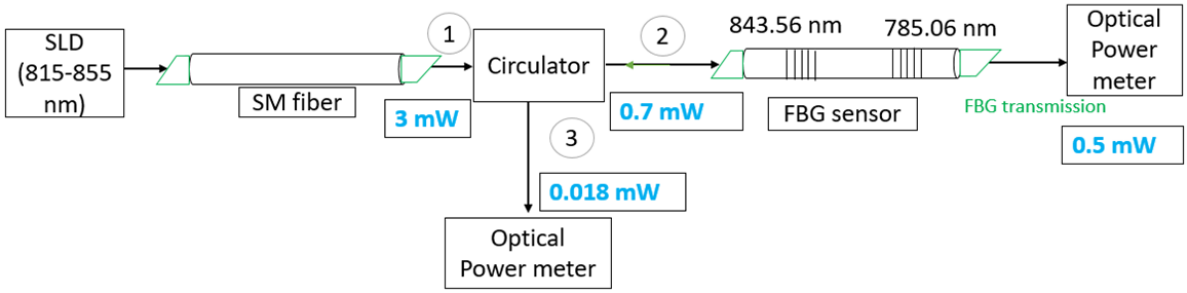

Figure 57: SLD coupling with circulator

Finally, the SLD light was injected into the FBG via an optical fiber circulator and propagates from port 1 through port 2 to the collimator, Figure 58. Light is free-space coupled into the FBG with the second collimator using a tip-tilt positioner.

The collimators should be axially aligned as much as possible for maximum coupling. The FBG is connected to the second collimator. The reflected Bragg wavelength goes from port 2 to port 3 of the circulator and is recorded using the spectrometer.

The light transmitted from the silica FBG was coupled directly to another an optical power meter.

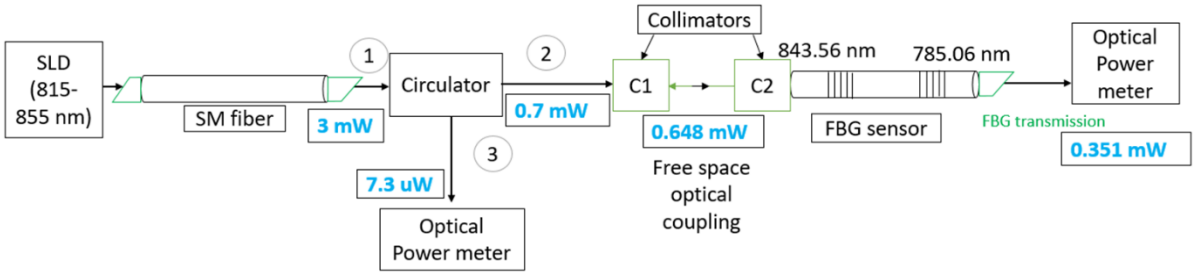

Figure 58: SLD coupling with circulator with the collimator lenses system

The collimators should be axially aligned as much as possible for maximum coupling. The FBG is connected to the second collimator. The free space coupling is very delicate and must be adjusted with extreme precautions. The reflected Bragg wavelength goes from port 2 to port 3 of the circulator and is recorded using the spectrometer.

The light transmitted from the silica FBG was coupled directly to another optical power meter. An optical power of 0.0073 mW is back reflected and 0.351 mW is transmitted. In this case the transmission loss is 9.31 dB and the reflection loss is 26.13 dB. The alignment of the coupling setup is crucial for optimal coupling of light into the fiber.

3.3.3 Thermal characterization of the FBG measurement system

This section presents the results of the temperature response of the Fiber Bragg Grating used in our work. The calibration process is crucial in order to establish a relationship between the measured wavelength and the actual temperature of the FBG over a temperature range with acceptable tolerances. This experiment will allow the calibration of the FBG sensor by calculating its sensitivity and the accuracy of the measurements.

3.3.3.1 FBG calibration setup

In this study, the temperature changes will be the applied perturbation. The broadband light that is coupled to the optical fiber circulator, propagates from port 1 through port 2 to the FBG and the Bragg wavelength is reflected back.

The Bragg wavelength goes from port 2 to port 3 of the fiber optic circulator and is detected using a spectrometer as the detection system as indicated in Figure 59.

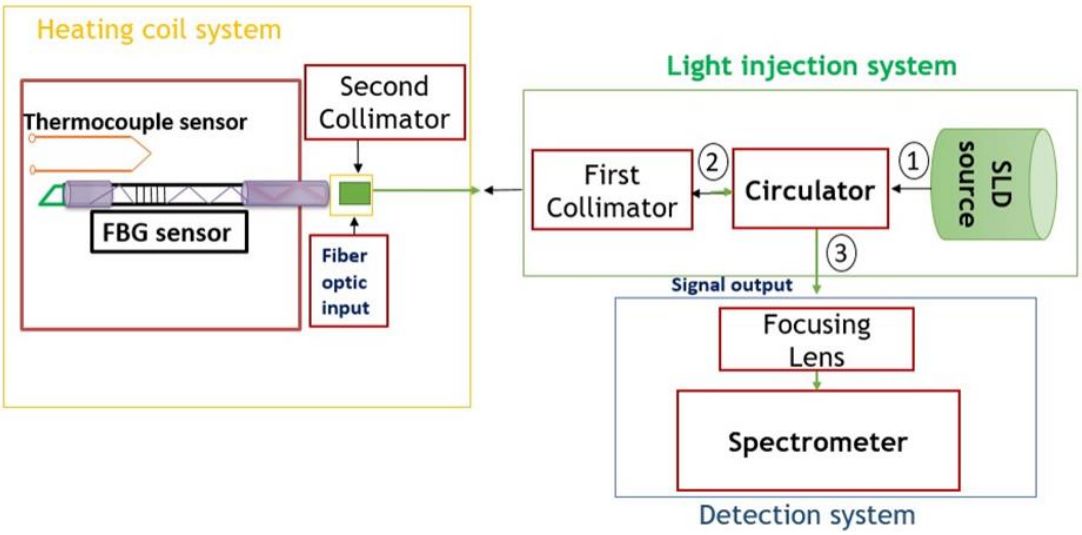

Figure 59: Block diagram of the calibration setup pf the FBG

This detection system determines essentially the spectrum of the reflected light in order to measure the shift of the Bragg wavelength as a function of the temperature changes.

In the experimental setup depicted in Figure 60, a heating furnace was fabricated at the laboratory and has been used in order to heat up the Bragg grating. The coil is placed inside a heat insulator. When an electric current flows through the coil, it converts the electrical energy into heat.

Figure 60: Heating system used for the FBG calibration

The furnace can reach 80 °C and various temperature cycle programs can be defined in order to induce temperature changes on the FBG sensor.

In order to calibrate the heating system, a T-type thermocouple (class A: +/- 1°C) which is the reference sensor has the similar size of the grating was used to measure the temperature at the site of the grating. It was used as a reference and the thermocouple has a 0.1 °C temperature resolution.

The FBG sensor was inserted inside the temperature-controlled coil and the Bragg wavelength was monitored along with the temperature. The temperature between the optical sensor and the thermocouple which is the reference temperature sensor is uniform due to the short distance between them.

3.3.3.2 Calibration method

The thermocouple tip is also placed for reference temperature measurement. The range to be calibrated is [20 °C, 70 °C], the block temperature is stabilized in a heat insulator.

The calibration technique accounts for both temperature and wavelength variations. Once the temperature is stabilized, the wavelength and temperature are recorded. This process is repeated for many temperature increments of 10 °C over the desired range. Then, the data is curve fitted.

The setup for the experimental characterization is shown Figure 61. The fiber end of the circulator is connected to the HR4000 spectrometer which measures the reflection spectrum of the Bragg grating. The FBG sensor is kept free hanging so that no strain influence affects the measurements.

Three sets of measurements were performed for the sensor in the range of [20 °C, 70 °C]. The thermocouple has been heated up to 70 °C because for now 80 °C is the temperature's limit of the FBG sensor and the heating system. Thermocouple 1 is placed at the location of the FBG as a reference temperature reading. The thermocouple 2 is placed on the coil to make sure not to exceed the maximum operating temperature of the fiber optic. Figure 61 shows a close-up view of the heating system.

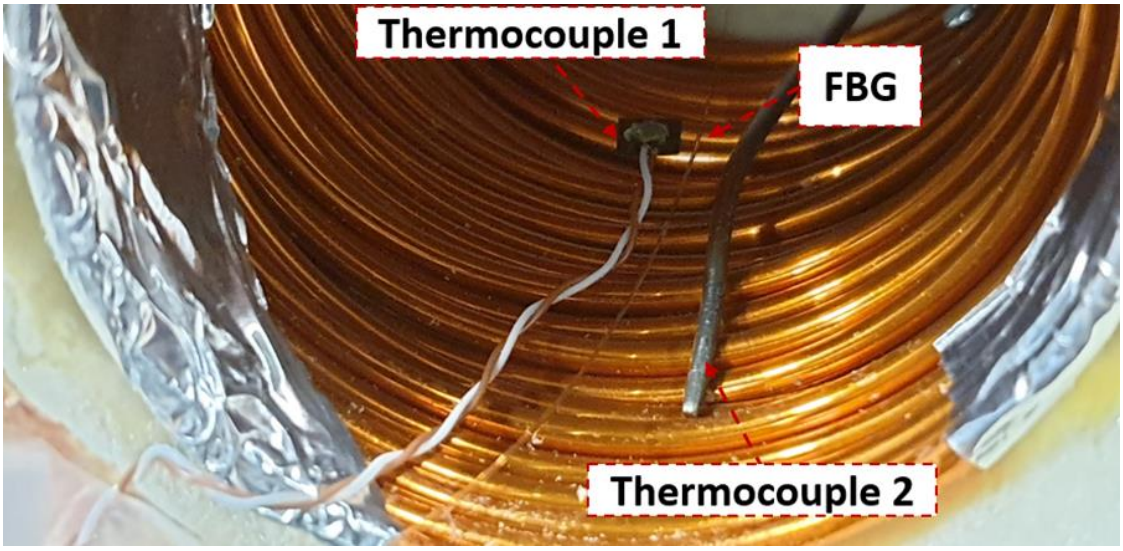

Figure 61: Close-up view of the heating system

A zoom on the setup for the experimental characterization: FBG sensor and a thermocouple tip in the furnace

We will characterize the fiber Bragg grating in order to determine its temperature sensitivity. The Bragg grating was inscribed in 4.4 microns core diameter regular silica 780-HP single-mode fiber. It was coated with a layer of acrylate material with a thickness of 245.0 ± 15.0 microns. First, we will experimentally determine the temperature sensitivity of the acrylate fiber as delivered by the company. This will allow to experimentally validate our simulations by comparing the experimental results and simulation results using TMM method as detailed in chapter 2.

Secondly, we will extract the relationship between the temperature and the measured wavelength. This relationship will be used in further experiments in the next chapter.

A section of the fiber containing a grating that has a Bragg wavelength of 840 nm is used for the calibration. The fiber is connected to the spectrometer.

3.3.3.3 Relationship between the measured wavelength and the temperature

For testing the FBG used here, the temperature of the coil was first changed from 20 °C to 70 °C with a step of 10 °C because it is the desired temperature change to be measured inside the rotor of the rotating machine. The observed reflection spectra and the change of the Bragg resonance wavelength as a function of increasing temperature are shown in Figure 62 and Figure 63, respectively.

In this experiment, the central wavelength of each Bragg reflection is calculated and a table with the Bragg shift for each temperature is produced. By performing the experiment three times we produced Table 11 in which each point is the average of the three measurements.

Table 11: Central wavelength measurement

Temperature (°C)	Average wavelength (nm)
20	843.509
30	843.568
40	843.607
50	843.646
60	843.711
70	843.743

The graph in Figure 62 shows the evolution of the measured wavelength of the FBG sensor along with the temperature variations. This spectrum shows a high signal to noise ratio, which means a low noise level. This corresponds to a high reflection from the grating.

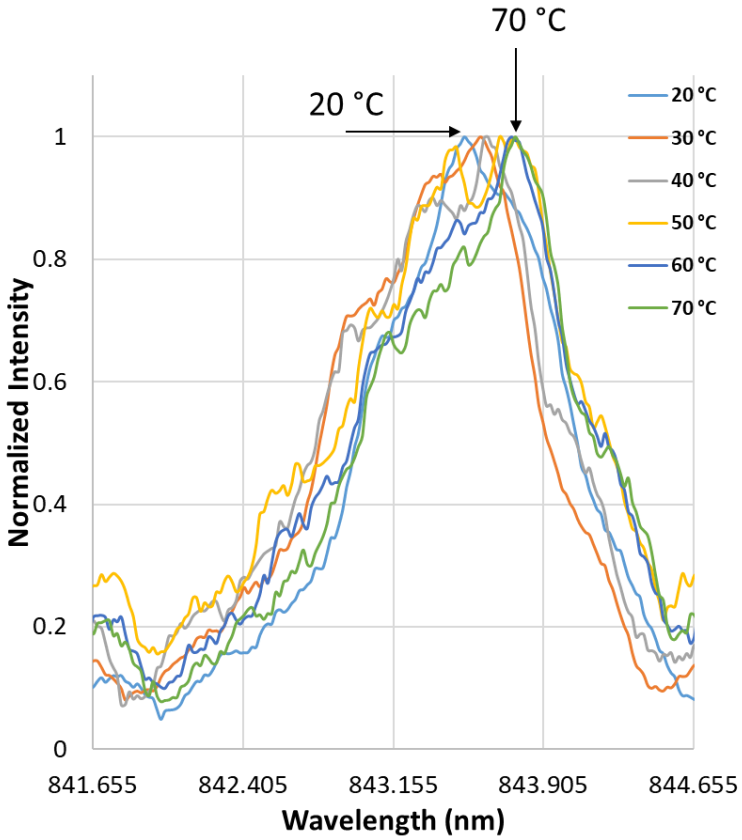

Figure 62: Spectral measurement of the FBG reflection response under different temperature values

The dependence of the shift of the resonance wavelength of the FBG due to the increasing temperature was measured to be 4.7 pm/ °C, see Figure 63. There is a good agreement between the results of the simulation and the experimental results. The theoretical value of the shift in the Bragg wavelength as a function of temperature is 5.5 pm/ °C for an FBG recoated with an acrylate coating. The difference of the temperature sensitivities between the experimental result and theoretical simulated value is mainly due to a discrepancy between different coating materials that induced thermal expansion coefficients of the cladding materials and the thermo-optic coefficients of different core materials.

The experimental results show that for the temperature range of [20 °C, 70 °C] of the FBG sensor, a linear equation will fit the data with a high correlation factor of $R^2 > 0.97$.

This experiment enables us to calculate the sensitivity and the accuracy of the measurement of the used sensor, as predicted in Chapter 2.

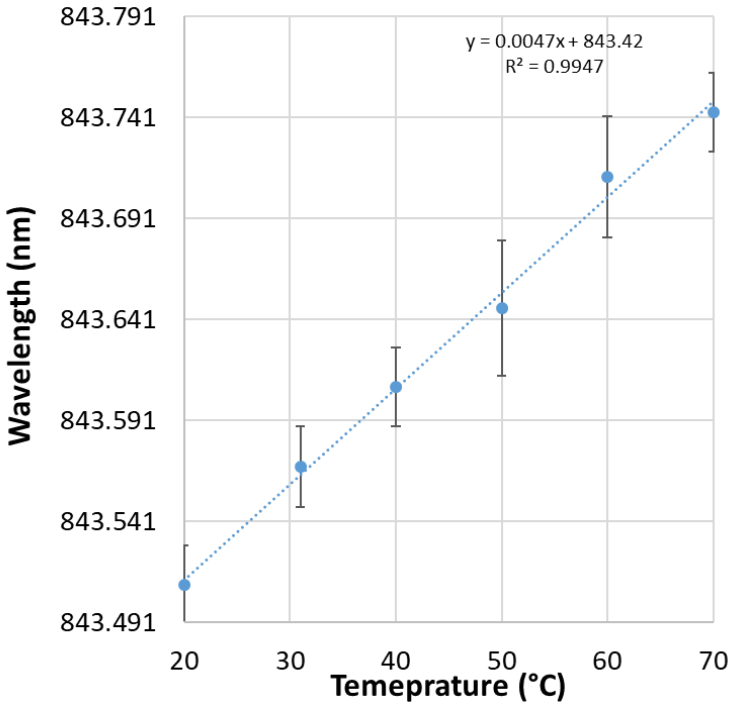

Figure 63: Relationship between the measured reflected wavelength of the FBG and the temperature

3.3.3.4 Optical performance of the sensor: measurement range, sensitivity and resolution

The calibration parameters are shown in Table 12: the theoretical and experimental sensitivities, the correlation coefficients of the curve fittings, the maximum residual errors and the root mean square errors.

Table 12: Calibration parameters

Calibration parameters	Theoretical sensitivity (pm/°C)	Measured sensitivity (pm/°C)	Correlation coefficient, R2	Maximum residual error, °C	RMSE, °C
	5.5	4.2	0.978	0.019	0.010
	5.5	5.2	0.981	0.018	0.012
	5.5	4.8	0.985	0.019	0.012

For this particular sensor, the measurement error analysis from calibration is shown in Figure 64. The maximum positive temperature measurement error for this sensor was of ~ 0.019 °C at 50 °C. The correlation coefficients are very close to unity. The temperature measurement errors are related to the errors in the interrogation system.

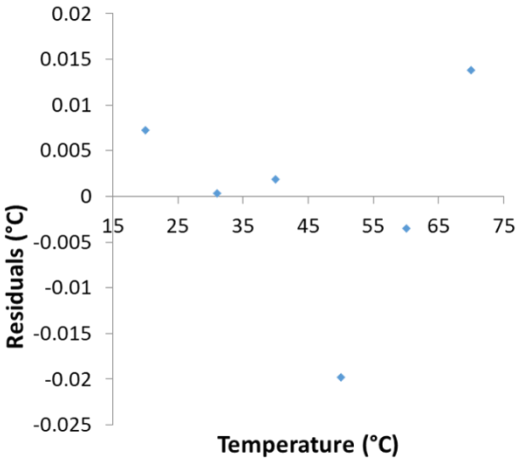

Figure 64: Typical Error from linear curve fit

In Figure 65 the measured data and the calculated relation are shown. It can be seen that the measured values of the temperature agree well with the theoretical values.

The deviation from the predicted linear dependence for temperature values are probably due to relaxation or elasticity of the glue used to fix the fiber ends.

The calculated relation Δλ/λB yields to a temperature sensitivity of 4.7 pm/°C for silica fiber FBG.

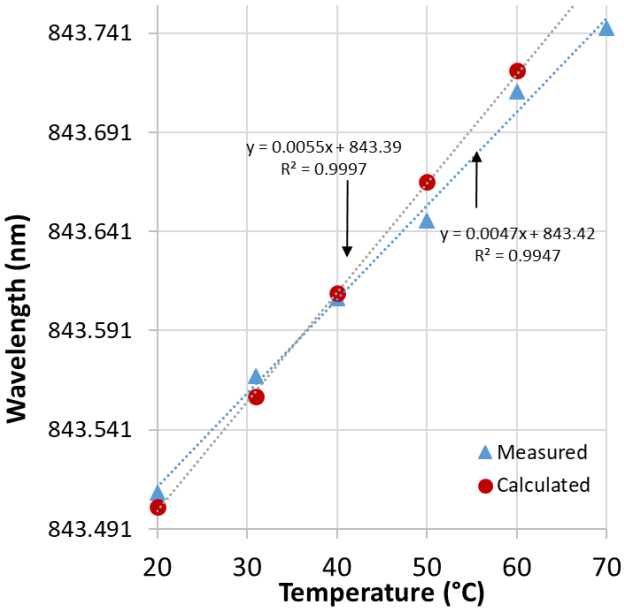

Figure 65: Measured and calculated FBG temperature sensitivity

The data produced from this experiment also allows us to calculate the linear relationship between the temperature of the FBG and the measured wavelength. We can calculate the temperature with a known wavelength, for this specific sensor, from the following equation:

$$T = C1 \times \lambda - C0 \quad (3\text{-}1)$$

Where:

T: Temperature in degrees °C

λ: Wavelength in nanometers

C1: 210.27

C0: 177343

The plot of the temperature as a function of the measured wavelength is presented in Figure 66. The correlation coefficient R^2 = 0.9947 demonstrates a good linearity of the FBG sensor for temperature measurements.

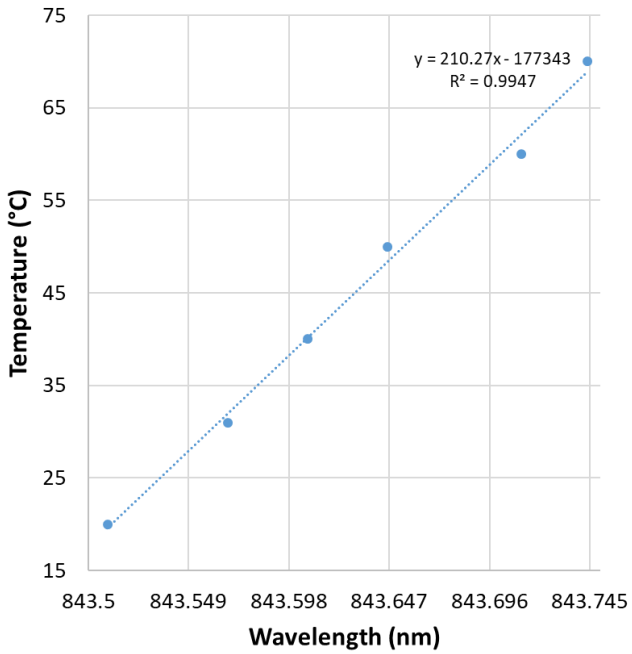

Figure 66: Linear relationship between the measured wavelength and the actual temperature of the FBG

3.4 CONCLUSION

The FBG sensor was statically calibrated in the laboratory to find its sensitivity, as detailed in section 3.3.3 in order to validate the sensitivity shown in chapter 2. The FBG sensor was characterized and the results were presented in this chapter. The characteristics of the optical system components used in the experiments such as the optical source, the FBG characteristics and the optical sensing spectrometer have been described.

Then, the setup and procedure used in this work in order to achieve our main goal was presented. In the first experiment, light was coupled from the super-luminescent diode into the FBG and the injection losses were measured in the commercial FBG. In the second experiment, the thermal calibration setup of the Acrylate coating FBG and its characterization were explained.

The temperature measurement with FBG sensor was experimentally validated. The FBG sensor was calibrated and its thermal sensitivity was determined and compared to the simulated one.

The calibration showed a linear relationship between the applied temperature and the measured wavelength. The reflected spectrum was inspected and the dependence of the shift of the wavelength of the FBG on the increasing temperature was measured. The temperature applied on the FBG caused a shift in the grating pitch and therefore a shift in the central wavelength. The Bragg peak was detected during the calibration experiments. We obtained a thermal sensitivity of 4.7 pm/°C with the FBG sensor.

The second step of the calibration procedure was the comparison between the measured temperatures and the simulated temperatures using TMM method.

These experimental results are in a good agreement the simulated one. The theoretical sensitivity differs from the sensitivity obtained in the calibration experiment. However, this could be explained by the fact that the temperature dependence of the refractive index (dn/dT) depends on the radiation time of the FBG inscription. During the FBG fabrication, the UV irradiation modifies the index of refraction of the fiber core and could possibly modifies the values of the thermo-optic coefficient in the FBG, which results in different sensitivities between the experimental and the simulated one. Additionally, from the experimental results, it has been observed that the maximum positive temperature measurement error for this sensor was of $\sim$ 0.019 °C at 50 °C.

The correlation coefficient of the linear curve fitting is very close to unity. This demonstrates a good linearity of the FBG sensor for temperature measurements. In the electric power industry, uncertainties below 10 °C are acceptable [132][133][134].

Therefore, the calibration experiment of the FBG system demonstrates that this optical sensor is appropriated for temperature measurements with a limit of resolution that satisfies the targeted application.

We will proceed to the installation of this FBG sensor in the electrical machine in the subsequent chapter in order to make dynamical temperature measurements in the rotating part of the machine. In addition, the interrogation system will consist of only one spectrometer and will interrogate the FBG sensor embedded in a rotating machine at 843 nm.

CHAPTER 4

DYNAMICAL TEMPERATURE MEASUREMENTS IN THE ROTATING MACHINE

4.1 INTRODUCTION

The aim of this chapter is to develop and characterize the integration of the optical temperature sensor in a small rotating machine when its functioning in dynamical mode.

A validation of the temperature measurement will be presented and applied for a geometrically small rotating machine. Many parameters have to be considered in order to design and assemble the instrument (shape, dimensions) and reach the targeted goal.

Consequently, we will explain the setup used in order to study the temperature variations of the rotor using the optical FBG sensor. By doing so, we simulate the FBG behavior inside the rotor of an electrical machine.

The setup and procedure used in this work in order to achieve our main goal are the following. In the first experimental study, we will give a detailed description of the mechanical system architecture and how the mechanical components were fabricated. We will detail the design assembly of the rotating machine, the fabrication of the rotor prototype, the installation of the FBG sensor in the rotating machine and the integration of the heating system around the prototype. Then, the free-space optical coupling system from the Super-luminescent diode (SLD) into the embedded FBG will be described. The concept demonstration of the realized design followed by the prototype validation with respect to design constraints and requirements will be detailed.

In the second experimental part, we will detect the FBG reflected signals and analyze the experimental measurements while rotating the motor. The sensitivity of the developed solution and temperature characterization of the rotor will be given. The calibration parameters and the optical performance of the sensor such as the measurement range, the sensitivity and the limit of the resolution will be extracted from raw measurement.

4.2 CONCEPT DEMONSTRATION OF THE REALIZED DESIGN

The main focus of this experiment is to explain the relation between the variation of the temperature of the rotating fiber Bragg Grating and the variations of the reflected wavelength of the optical signal. To demonstrate this approach, the experimental arrangement for detection of light injection with rotating fiber optic is explained. Three main parts are constituting the measuring system. The optical system (light source and the detector), the rotational system and the processing part.

4.2.1 Optical system

In this work, the optical system is based on a Super-luminescent diode (SLD-M381, Superlum), which transmits the light to the fixed collimator. The power of the used SLD was high enough to ensure that the reflected and/or transmitted light were adequate to be detected. A current controller enables tuning the wavelength over the SLD full range from 825 to 855 nm. Light is emitted from the SLD and propagates along the optical fiber circulator (PMD-Hi780). The optical coupling lenses are TC25APC Triplet Collimator from Thorlabs company. In order to widen the cross sectional area of the optical connection, triplet collimating lenses were used. It provides adequate coupling of light between the SLD and the embedded FBG sensor (core diameter of 4 µm, Numerical Aperture ≈ 0.1). The rotating collimator embedded onto the rotor is also a collimated triplet from Thorlabs. Continuous optical connection is enabled during rotation by coaxially aligning the two lenses onto the rotation axis of the rotor. Nevertheless, mechanical misalignment and optical error always remain between the stationary and rotary parts. The proposed FBG sensor system is shown in Figure 67.

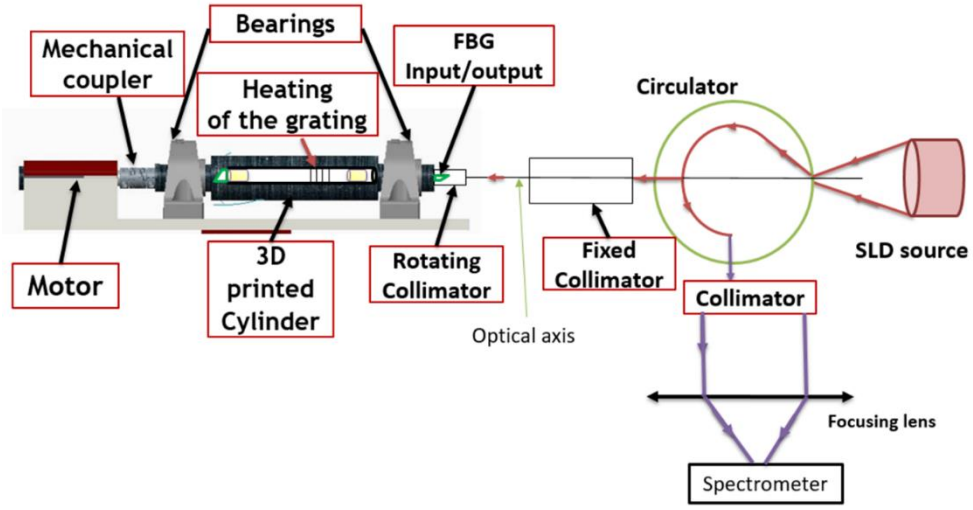

Figure 67: Non-contact sensing system with embedded FBG sensor

4.2.2 Rotational system

The rotational system, which is called academic rotor is based on 50 mm diameter 3D printed cylinder assembled with a small motor (Maxon EC 60 mm, 40 W brush and HEDL400 encoder), a mechanical metal bellow coupler (A5-260-19, Michaud Chailly) and two bearings (SY25TF, SKF). The 3D rotary cylinder was designed and printed using a 3D printer available at UTC. This cylinder is supported by two bearings, to minimize vibrations, on both ends. The assembled structure is presented in Figure 68.

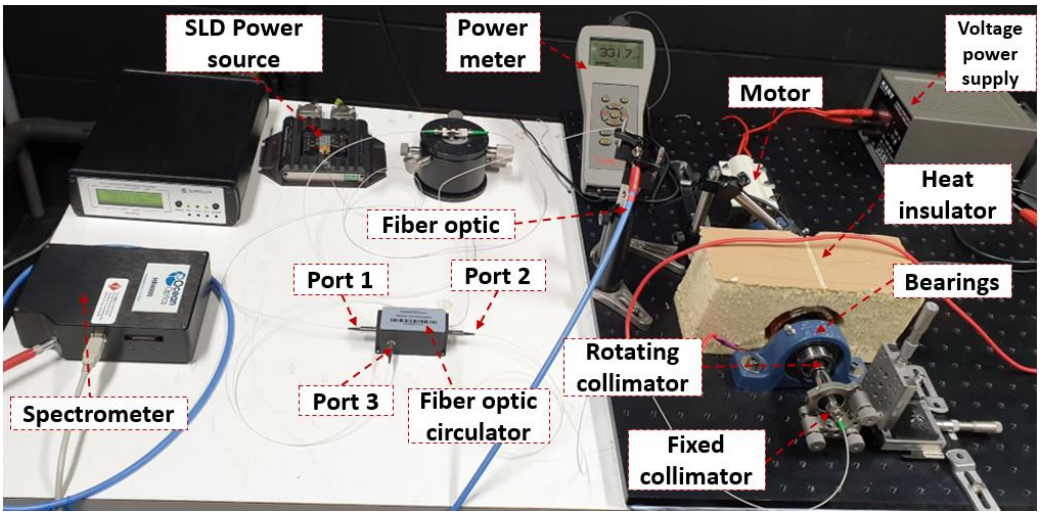

Figure 68: Sensor's architecture and rotor test-bench

In order to detect the signal, a customized spectrometer (HR 4000, Ocean optics) and the 1.5 m long customized fiber Bragg grating sensor that was purchased (Optromix company) were implemented. The FBG was inserted inside the 3D printed cylinder.

The speed of rotation of the whole set can be changed by using a tunable voltage power supply (0 V - 28 V) enabling a speed of rotation between [0 rpm, 860 rpm]. The fiber that is attached to the collimator is rotated around its axis in that way.

4.2.3 Sensor's architecture and rotor test-bench

The rotational system and the optical system are mounted on a fixed optical table. In this system, SMF-28 single mode fiber are used with FC/APC (angled polished connector) connectors. The two collimators were positioned opposite to each other for the alignment procedure. The air gap between the faces is 0.5 cm.

The fixed collimator was aligned for maximum coupling into the sensor fiber using high resolution three-adjusters' alignment mount. The fixed collimator and the rotating collimator should be parallel as much as possible in order to maximize light coupling.

Figure 69 shows a close up view of the optical connection between the stationary and the rotary parts using triplet lenses. The light source having an FWHM of 15 nm crosses the gap from right to left. The light reaches the FBG sensor fixed onto the surface of the cylinder. The Bragg grating in the FBG sensor reflects light with a specific wavelength which is 843.51 nm. The deformation of the rotating part and the temperature changes cause a physical change in the Bragg grating which leads to a wavelength shift as described in chapter 2.

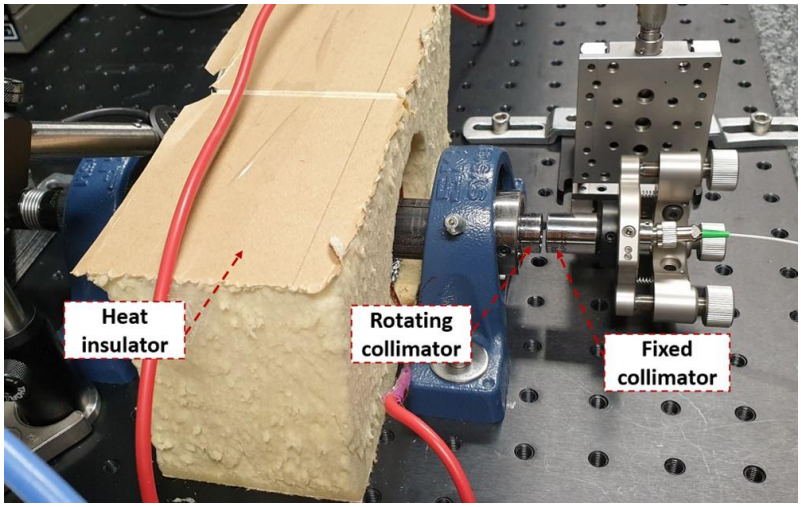

Figure 69: Close-up view on the free-space coupling system

Light from SLD source, with a maximal optical power of 90 mW operating at central wavelengths of 840 nm, was coupled to the FBG sensor using suitable optics. The light source was collimated in one direction by using a triplet collimator lens.

The light beam was injected continuously and then coupled to the rotating triplet collimator and focused into the fiber core, as shown in Figure 70. The fiber has a core diameter of 4.4 µm, an outer diameter of 900 µm and a length of 1.5 m.

The reflected light exits the rotating collimator and enter the fixed one. The light beam reflected by the Bragg grating will be directed through the circulator from port 2 to port 3 arriving at the lens that focuses the beam onto the spectrometer, as shown in Figure 70.

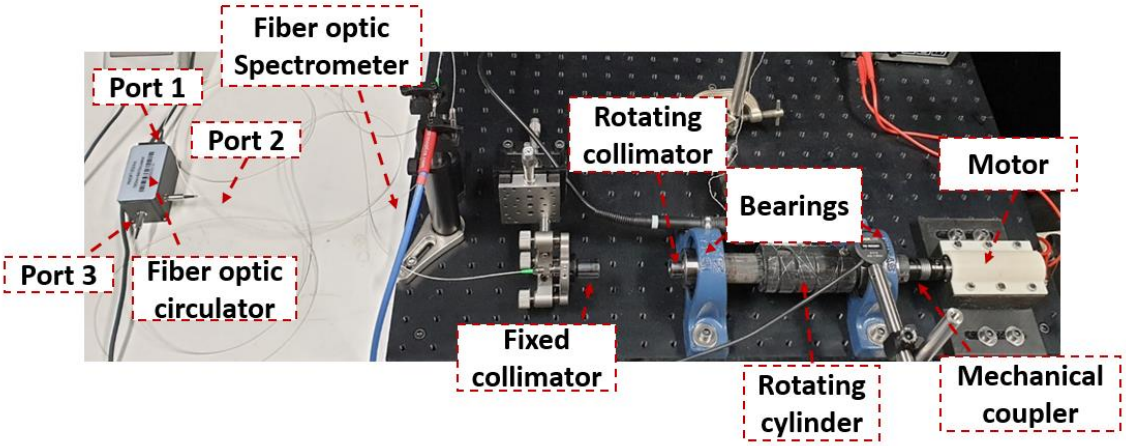

Figure 70: Free-space optical coupling system

The optical coupling consists of two collimators with a small air gap between them. The use of convenient lenses to couple and to collect light diminishes signal losses due to vibrations in the rotating cylinder. We used Triplet collimators to widen the cross sectional area of the optical connection and enabling light to travel parallel to the lens axis. In order to enable continuous optical connection during shaft rotation, the two lenses need to be coaxially aligned.

The fixed collimator and the rotating collimator have to face each other as much as possible for effective light coupling. The collimators have to be coaxially aligned. The alignment has 4 independent parameters which are the collimator positions X and Y and the collimator angles. As shown in Figure 71, the optical coupling is subjected to different insertion losses such as lateral and angular misalignments due to the rotation of the motor. To even roughly find the right collimator position is an experimental challenge.

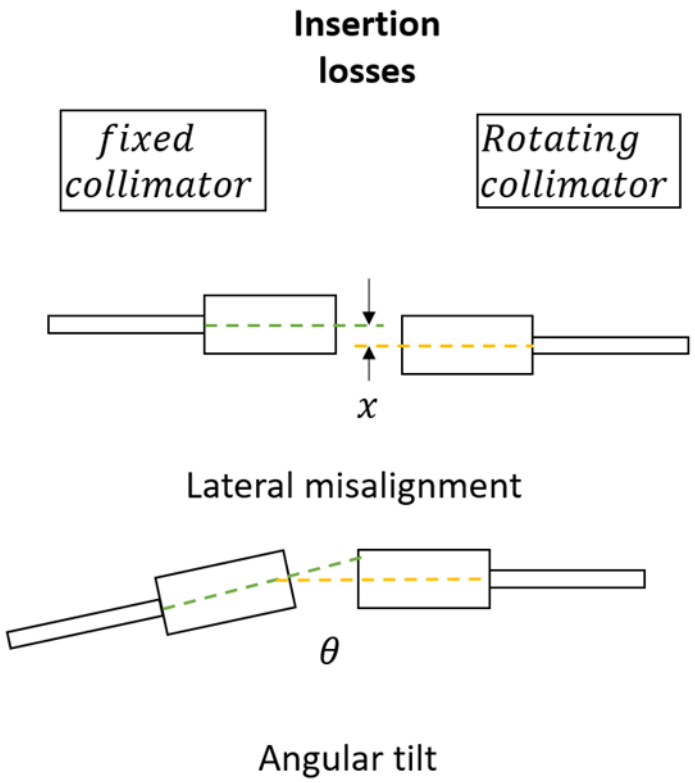

Figure 71: Insertion losses due to free-space coupling

4.3 MECHANICAL SYSTEM ARCHITECTURE

The motor rotates a secondary shaft which is connected to a primary shaft by a coupler. We will put a mechanical coupling so that the cylinder will be well positioned with respect to the axis of rotation. In addition, the mechanical coupler will be used to compensate for the misalignment while transmitting torque from the motor to the cylinder.

Misalignment will cause vibration. Therefore, two bearings and a mechanical coupler were used to reduce vibrations and ensure the light injection. The bearings will support and condition the rotation of the cylinder.

4.3.1 Rotating machine design and fabrication

First, the design of the rotating machine was drawn on creo software as shown in Figure 72.

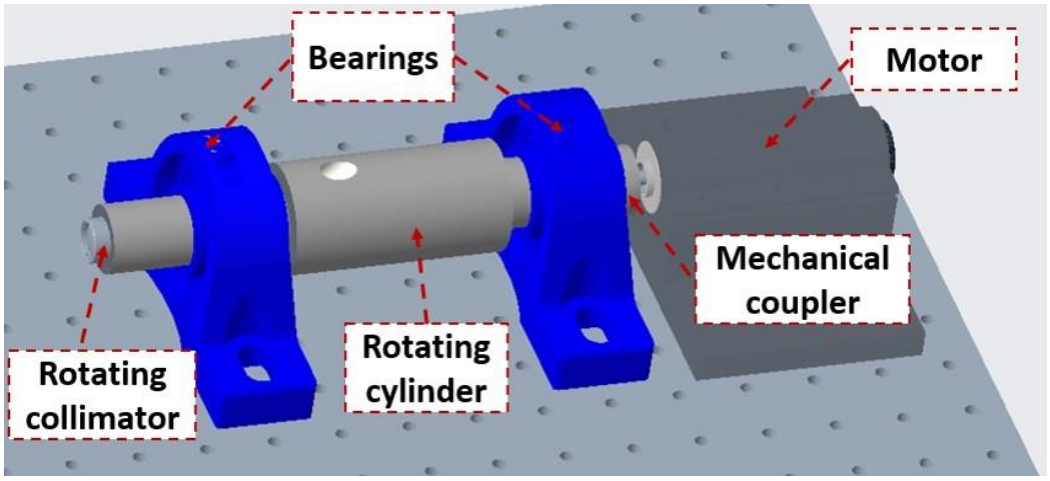

Figure 72: Cad model of the rotating machine

The FBG was inserted inside the 3D printed cylinder. The cylinder was composed of two main pieces. The fiber inside the cylinder will be enrolled by a foam in order to minimize its vibration.

In Figure 73, the cross section of the fabricated cylinder is shown. The next step after fabrication of the cylinder is the integration of the FBG sensor into the mechanical structure.

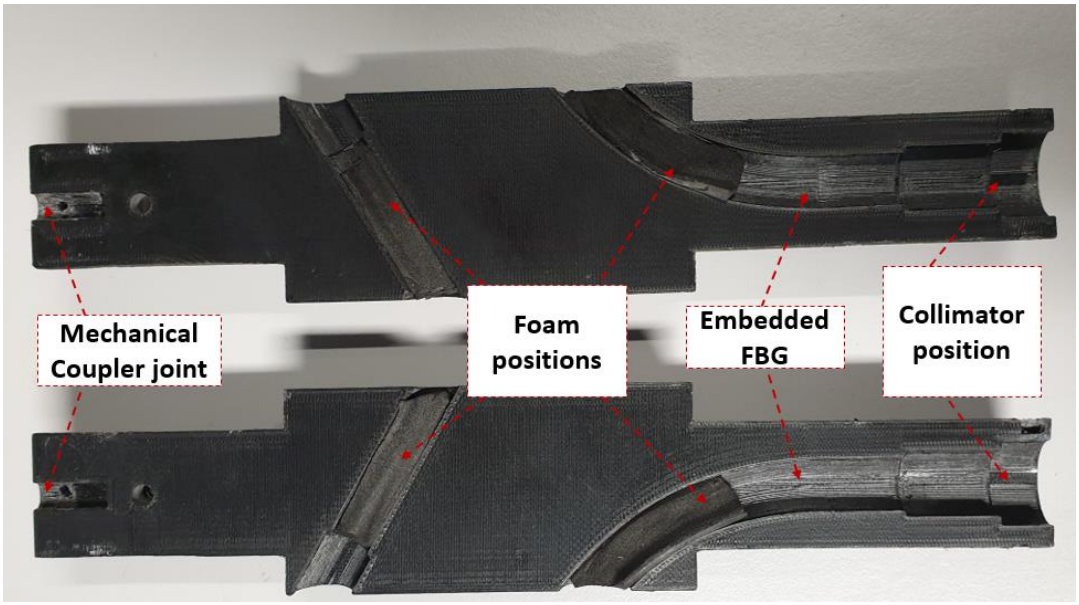

Figure 73: Cross section of the cylinder sent fabrication to the fablab

4.3.1.1 Installation of the FBG sensor in the rotating machine

The fabricated FBG needs to be embedded into the rotating cylinder in an intelligent way in order to perform dynamical temperature measurements in a safe manner.

The schematic proposal of the FBG, embedded into the cylinder can be viewed in Figure 74 and Figure 75 from a different angle. The cylinder has a 25 mm radius to fit in the dynamic rotational bearings and to respect the maximal bending radius of the fiber in order to protect the FBG from breakings. This cylinder was supported by two bearings on both ends with a gap of 10 cm to minimize vibration.

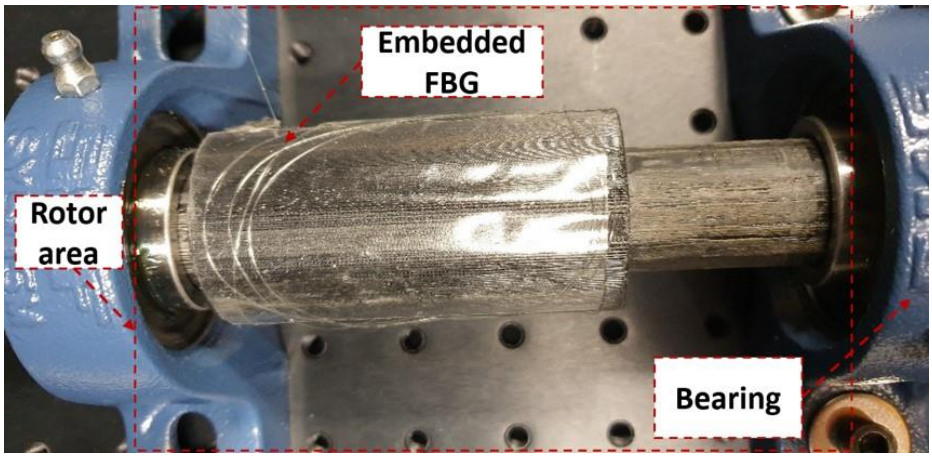

Figure 74: FBG instrumentation showing the positioning of the Bragg grating

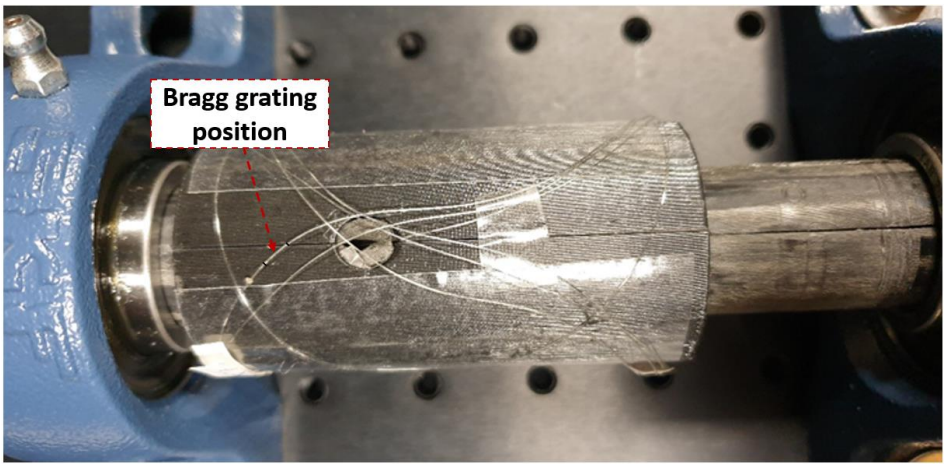

Figure 75: Embedding the FBG in the rotating machine

Next, the heating furnace will be integrated in order to cover all the rotor area.

4.3.1.2 Heating system integration

The same heating system that is developed and described in chapter 3 will be used for heating the rotor of the machine as shown in Figure 76.

The following step is to assemble the rotating machine with the embedded FBG sensor.

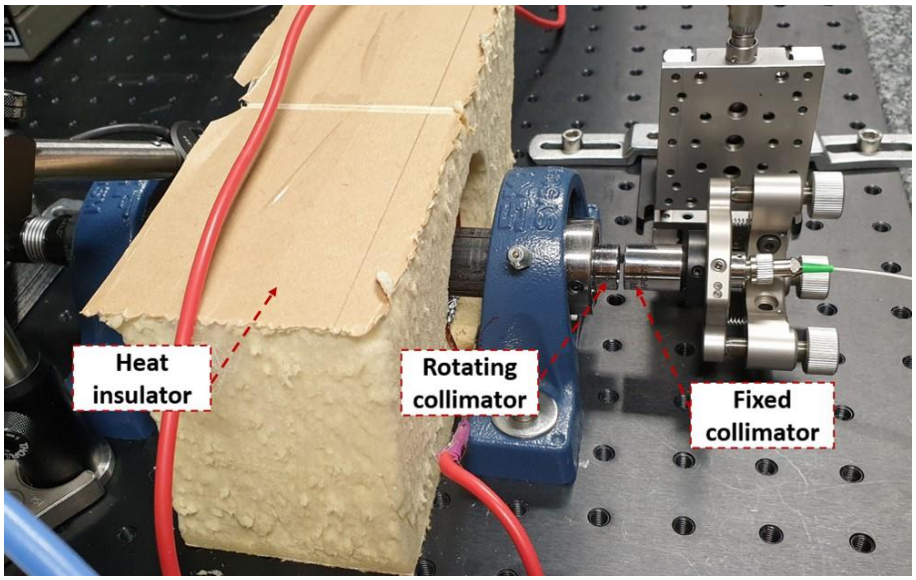

Figure 76: Heating system integration

4.3.2 Prototype assembly procedure

The setup of the rotating machine has been developed in our laboratory as shown below in Figure 77. The characterization of this rotating machine is also detailed later in this chapter.

The following procedure is used for the assembly of the final design.

- The shaft is first prepared
- The fiber Bragg grating is connected to the collimator and then is inserted into the cylinder. This is done while ensuring that the FBG goes through the two openings at both end of the cylinder. The used foam prevents the fiber from getting out.
- The shaft is then inserted and the screws are pre-tightened
- The two sides of the cylinder are joined and held together using a screw
- One side of the mechanical coupler is attached to the cylinder
- The whole cylinder is then fixed inside the two bearings
- The mechanical coupler is then attached to the electrical motor
- An alignment procedure of the assembled structure is done after this

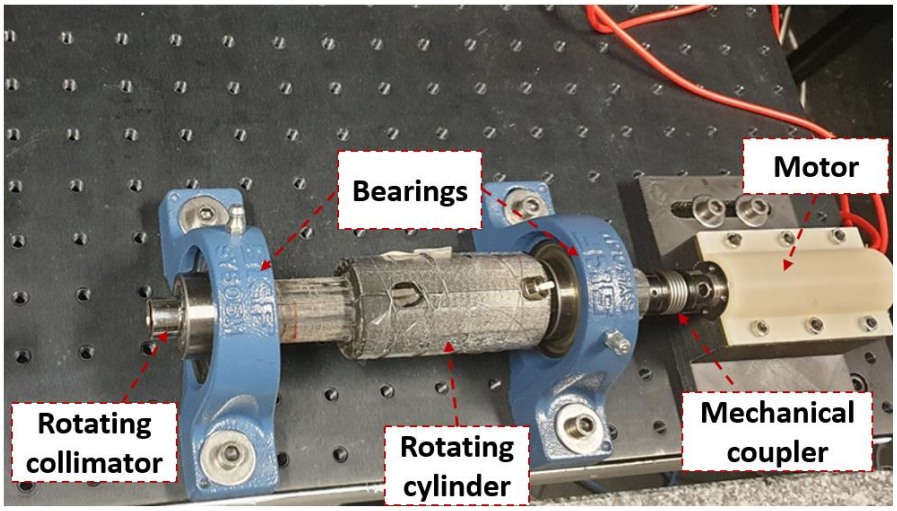

Figure 77: Setup of the rotating machine

4.4 PROTOTYPE VALIDATION (DETECTION AND PROCESSING)

4.4.1 Spectrum of the FBG signals under different rotation speed

In this setup, we performed a series of measurements in order to measure the FBG reflection spectrum at a given rotation rate while heating the system. The rotor temperature was stabilized for 30 min before rotating the machine.

Temperature measurements with the FBGs were made and recorded for eight heat run tests. For testing the rotating FBG, the temperature of the coil was first changed from 20 °C to 70 °C with a step of 10 °C.

Some representative rotation speeds show a clear shift in the reflection spectrum. Spectral measurements were performed at rotation rate intervals of approximately 120 RPM intervals up to 860 RPM. For the heating process, Figure 78 shows five superimposed reflection spectrum for each temperature measurement while rotating the machine at 177 RPM.

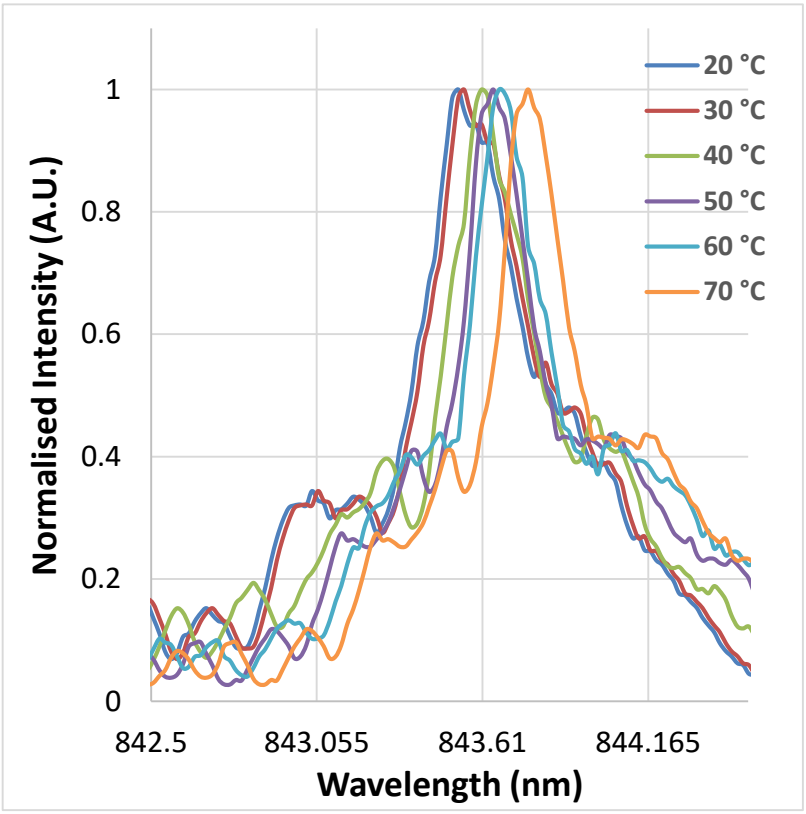

Figure 78: Spectral measurement of the heated FBG under 177 rpm

The wavelength shift result of the reflection response of the FBG as a function of the wavelength is plotted in Figure 79 for a rotating velocity of 860 RPM while increasing the temperature.

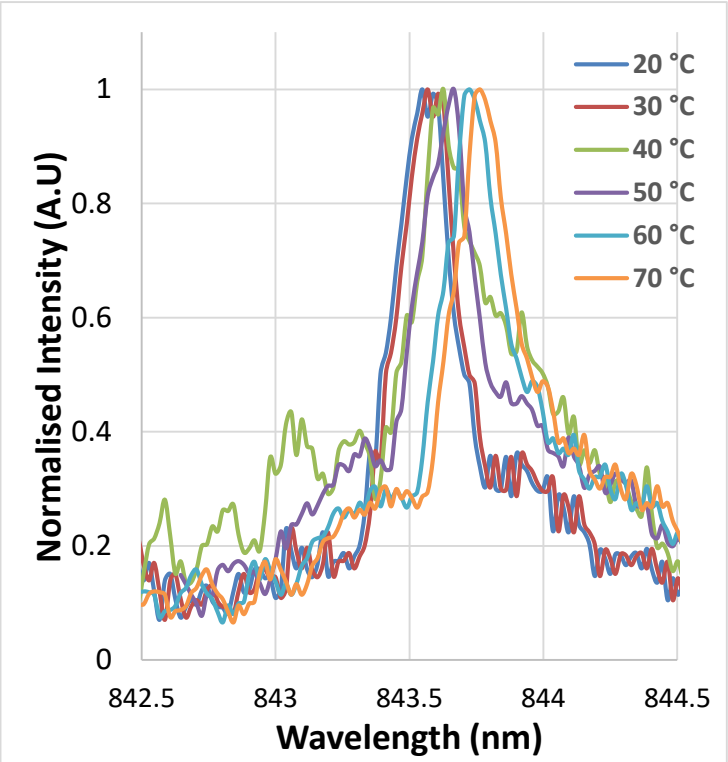

Figure 79: Spectral measurement of the heated FBG under 860 rpm

When the rotor is rotating at high speed (860 rpm), the light is coupled into the FBG sensor. A clear shift of the Bragg wavelength is shown at 860 rpm. The reflection spectrum of the FBG under high rotation rate (860 rpm) appear noisier than the spectrum at 177 rpm. Noise is an important factor that affects the FBG spectrum. In order to extract the right information from the FBG signal the intensity of the noise should be smaller than that of the signal.

Figure 80 shows at 860 rpm and under 70 °C that the noise level is low and do not affect the extraction of the optical signal that carries the temperature information.

The visible noise is mainly due to the high frequency of rotation of the machine. The noisy signal is created by the rotor of the machine that is generating vibrations. In addition, the optical return loss could cause noise in the system.

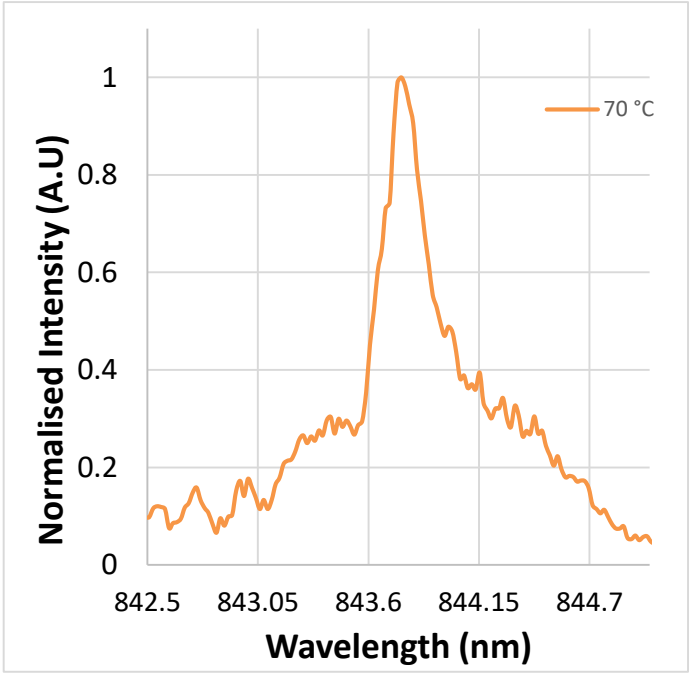

Figure 80: FBG spectrum at 860 rpm under 70 °C

In addition, the intensity of the reflected signal does not depend on the speed of rotation of the rotor. In fact, it depends on the efficiency of the light coupling between the fixed collimator and the rotating collimator. In Figure 81, it can be seen that at 42 °C for a rotation rate of 591 rpm, the reflected intensity is 4 times higher than the reflected intensity at 439 rpm and at 754 rpm it is 2 times higher than that at 439 rpm.

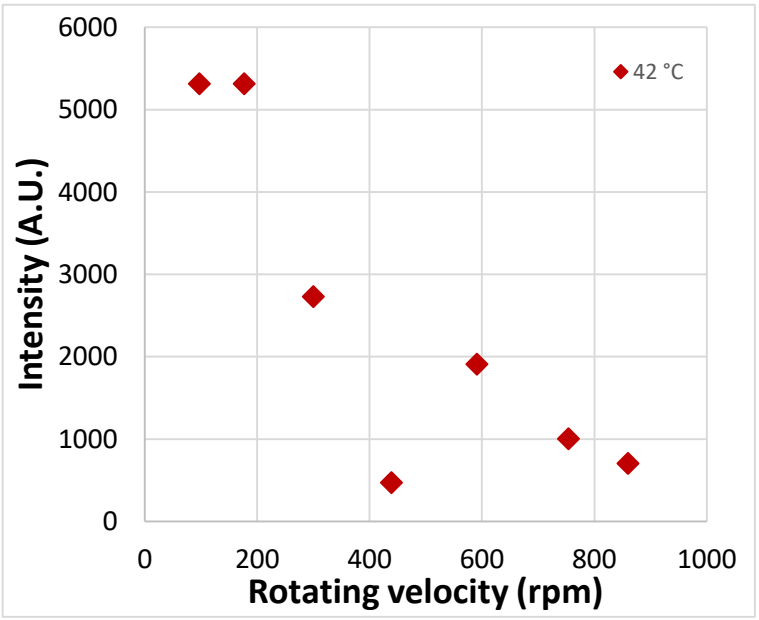

Figure 81: Reflected intensity of the FBG for different rotation rates

Therefore, for some high speed of rotation we can have a reflected intensity of light that is higher than at low speed of rotation due to a high coupling efficiency of the light. This can lead to the conclusion that the intensity of the optical signal reflected by the FBG sensor is independent of the rotation rate of the rotating machine. The coupling efficiency of the light depends on the mechanical strain in the rotating cylinder that causes the collimator to become misaligned.

4.4.2 Rotor temperature calculation

In this experiment, the central wavelength of each Bragg reflection is detected and a table with the Bragg shift for each temperature is produced. The data is recorded for performing one cycle of a heat run test and by performing the experiment three times we produced Table 13 in which each point is the average of the three measurements.

Table 13: Average wavelength of the three measurements

	Average Wavelength (nm)						
Thermocouple Temperature (°C)	97 RPM	177 RPM	300 RPM	439 RPM	591 RPM	754 RPM	860 RPM
26	843.541	843.522	843.515	843.528	843.535	843.535	843.541
32	843.554	843.555	843.561	843.568	843.554	843.568	843.561
40	843.600	843.587	843.587	843.601	843.587	843.600	843.607
48	843.639	843.639	843.646	843.620	843.646	843.646	843.626
61	843.698	843.685	843.698	843.711	843.685	843.704	843.711
77	843.770	843.776	843.776	843.789	843.776	843.783	843.789

In order to know the exact temperature of the rotor of the academic machine, we used the calibration equation calculated in chapter 3 (section 3.3.4). Assuming the wavelength readings in Table 13, we calculate the temperature as follows:

$$T = 210.27 \times \lambda - 177343 \quad (4\text{-}1)$$

Where:

T: Temperature in degrees °C

λ: Wavelength in nanometers

The temperature distribution is measured and shown in Table 14. It can be seen that both measurements at minimum speed (177 RPM) and maximum speed (860 RPM) that represent the two extreme rotating velocities shows that the temperatures changes of the rotor after thermal stabilization.

Table 14: Temperature distribution

	Average Temperature (°C)						
Thermocouple temperature (°C)	97 RPM	177 RPM	300 RPM	439 RPM	591 RPM	754 RPM	860 RPM
26	28.506	24.441	23.039	25.772	27.174	27.104	28.506
32	31.239	31.309	32.641	34.043	31.239	34.043	32.711
40	40.912	38.178	38.178	40.982	38.178	40.912	42.313
48	49.112	49.112	50.444	45.047	50.514	50.514	46.379
61	61.448	58.715	61.448	64.182	58.785	62.780	64.182
77	76.517	77.849	77.849	80.583	77.849	79.251	80.513

4.4.3 Characterization parameters

4.4.3.1 Dynamical temperature sensitivity of the developed solution

For each series of measurement, there was some differences in temperature due to the limited resolution of the detector. Each time the collimators are aligned, one spectral acquisition is captured. The time between spectral acquisition is high for low rotation velocity. However, for high rotation velocities small time intervals occur between spectral capture and more spectra are captured each minute at 860 RPM than at 177 RPM. Therefore, we have to wait more time at 177 RPM to get a reading of the temperature of the rotor than at 860 RPM.

In addition, the coincidence time in which the collimators are aligned occurs more often for high rotating velocities. Then, the calibration graph of the wavelength versus temperature is plotted in order to determine the dynamical temperature sensitivity of the FBG. In Figure 82, the graph shows the evolution of the FBG as the temperature varies for different rotating velocities. We obtained an averaged dynamical temperature sensitivity of 4.7 pm/ °C, from the calibration graph.

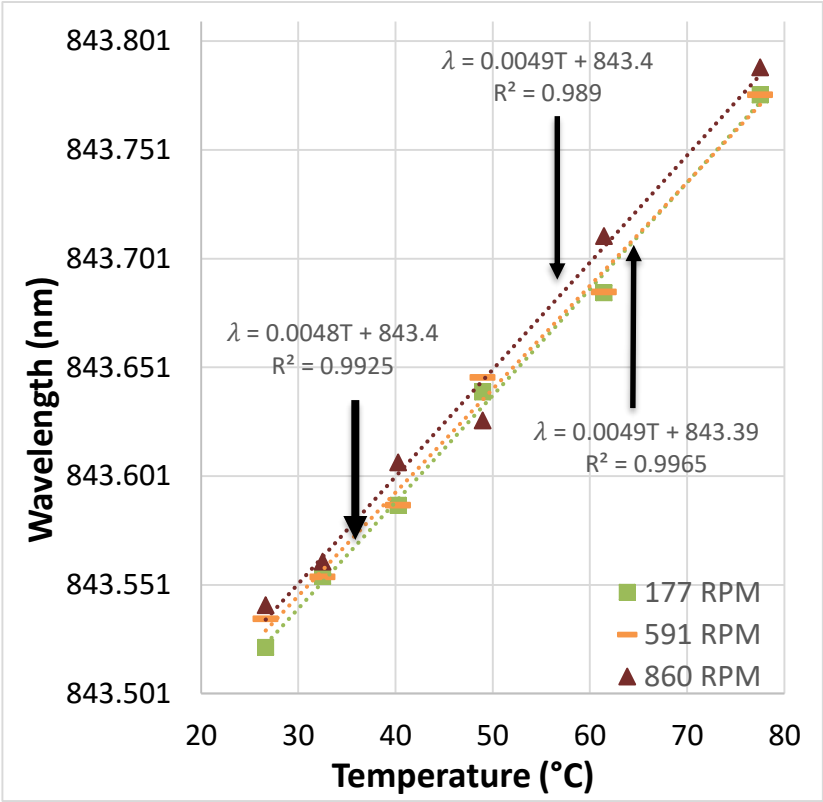

Figure 82: FBG dynamical temperature sensitivity

4.4.3.2 *Performance of the sensor: measurement range, measurement speed and sensitivity*

For this FBG sensor, the measurement error analysis from calibration is shown in Figure 83. The maximum temperature measurement error for this sensor was of ~ 0.024 °C at 50°C and 439 RPM.

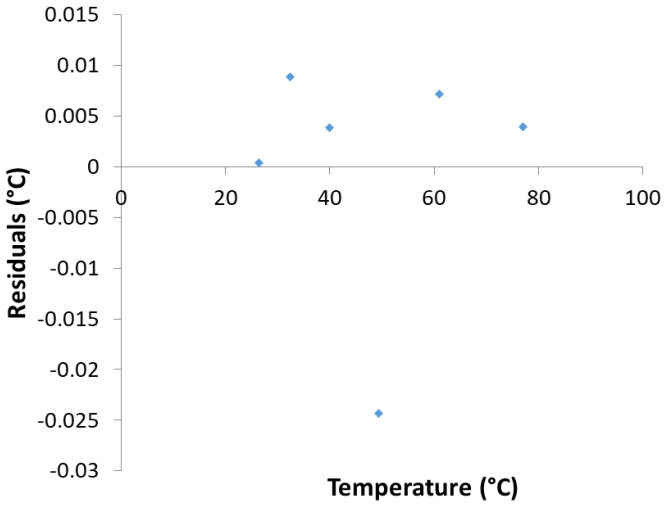

Figure 83: Typical Error from linear curve fit

Table 15 shows the calibration parameters from some rotating velocities: the experimental sensitivities, the correlation coefficients of the curve fittings, the maximum residual errors and the root mean square errors.

Table 15: Dynamical calibration parameters

	Calibration parameters			
Rotating Velocity (RPM)	Measured sensitivity (pm/°C)	Correlation coefficient, R2	Maximum residual error, (°C)	RMSE, (°C)
97	4.6	0.997	0.008	0.021
177	4.9	0.996	0.008	0.022
300	5	0.994	0.007	0.045
439	5.1	0.986	0.024	0.030
591	4.8	0.992	0.009	0.027
754	4.8	0.999	0.002	0.059
860	4.9	0.989	0.020	0.034

The correlation coefficients are very close to unity which indicates the linearity of the measurement. The value of the uncertainty error is related to the uncertainty of the interrogation system. This corresponds to a temperature uncertainty of about 10 °C

considering an average sensitivity of 4.7 pm/°C, as demonstrated in the experimental results. This can be improved by working on the dynamical interrogator.

4.5 CONCLUSION

This chapter described the dynamical test and operation of a fiber Bragg grating temperature sensor inside an operational small power rotating machine. After calibrating the FBG sensor in the previous chapter, we proceeded in this chapter to the installation of the FBG sensor into the fabricated academic rotating machine.

The calibration process was crucial in order to establish a relationship between the measured wavelength and the actual temperature of the FBG over a specific temperature range with acceptable tolerances. The calibration of the FBG sensor is a necessary feature to determine accurate temperature measurement into the rotor of machines.

The goal here is to experimentally characterize and validate the integration of the sensor. First, the rotating machine has been designed, fabricated and assembled in our laboratory. The mechanical design with integrated FBG is experimentally validated. A heating furnace was fabricated to heat up the grating while rotating the academic machine.

FBG reflected signals have been measured while rotating the motor. We have measured the temperature in the rotating machine at 120 RPM intervals up from a rotating velocity of 177 RPM to 860 RPM. Each temperature measurement took several minutes. Wavelength shifts due to temperature variations are measured up to 860 RPM, which is the maximum rotation speed that can be reached with our rotating machine.

An averaged dynamical temperature sensitivity of 4.7 pm/°C is reached. We were able to design a coupling device capable of coupling a sufficient amount of light into the FBG sensors at the rotating part. The distance between the stationary and the rotatory part was 0.5 cm. At 860 RPM, the time where the parallel beam hits the rotating collimator is just a few microseconds.

The interrogation unit must be capable in getting the sensor information within that short period. The optical connection is often broken while rotating the cylinder. Signal losses due to the vibrations in the rotating cylinder were diminished by using the convenient lenses.

The reflected light is detected using a spectrometer. These signals correspond to temperature variations on desired locations on the rotor. The study of the sensing characteristics showed a maximum error of 0.024 °C over a temperature measurement range of [20 °C - 70 °C]. These values meet the requirements for many power industry applications.

In this chapter, the presented results showed the possibility of using the FBG sensors in order to accurately monitor the temperature into the rotor of rotating machines. The temperature measurement system has been validated and the dynamical temperature variation in the rotor of the electrical machine has been measured and characterized. Our method demonstrates that the measurement of temperature on a rotating part is possible using FBG sensors. The obtained results are satisfactory and proves that the principle works.

A thermal profile of the temperature of the rotor in the rotating machine would be obtained by using a single fiber optic that includes several gratings. This technique is not

limited by the speed of rotation. We believe that temperature sensing under faster rotations should be possible if the signal processing is improved.

As the rotation speed changes, re-alignment of the stationary collimator can be useful to compensate for the misalignment. This technique can be implemented in real-world environments. In dusty environments, the faces of the collimators should be cleaned periodically.

As a conclusion, the system is capable of making accurate temperature measurements and monitoring inside the rotor of a rotating machine taking into consideration the harsh environment of the stator.

GENERAL CONCLUSION AND FUTURE WORK

The need to develop distributed temperature sensor systems for application in electrical machine drive this work. This thesis focus on the technology of Fiber Bragg Gratings (FBGs) which represents an innovative technique that can be applied to the field of electrical machines.

The main objective of this thesis is to enable the dynamical measurements of temperature variations with fiber Bragg grating (FBG) embedded into a rotating machine. We proposed a simple method, including a spectrometer in order to make temperature measurements possible. The detection system can give the temperature values at different rotor location that helps the extension of the life of the machine. It can also optimize the energy consumption of the machine.

In a literature review, temperature sensors have been reviewed. Existing methods in the literature have been researched for measuring temperature in the electrical machines. Rotating parts of electrical machines are affected by thermal strain, centrifugal force and hot spot temperatures. Engine monitoring is important to protect from thermal and mechanical overload. However, the precision of simulating the rotating parts behaviour depends on the calibration measurements and is complex. The measurement of local temperature inside the rotor offers several benefits such as protection, diagnostics and lifetime extension of the electrical machine components. However, electrical sensors used for interrogation are sensitive to electromagnetic interferences. In addition, their usefulness is limited because of some dominant problems, such as the limited number of channels because the slip ring that ensures the contact with the detection system, cannot be too big. It can be concluded, from the literature review that the Bragg wavelength temperature sensitivity is very small; thus a sensitive instrument is required to measure such a change and there is a demand to carry on research in the detection of small temperature changes of the order of 10 °C with a low cost instrument. Based on this state of art, a contactless measurement technique of the rotor temperature that uses Fiber Bragg Gratings (FBGs) sensors has been proposed in the context of small rotating machines monitoring due to its advantages.

In chapter 2, a literature review of the different methods for grating simulation has been presented. Then, the simulation of uniform Fiber Bragg Grating using T-matrix formalism has been presented. Fiber Bragg grating sensors responses have been studied for temperature measurement by using the TMM technique for the simulation of uniform Fiber Bragg Grating. The results of the simulation of the temperature and strain response has been presented. The reflected spectrum has been inspected. The results of the simulation of the temperature shows that the dependence of the shift of the wavelength of the FBG on the increasing temperature has been measured to be 5.5 pm/ °C.

In chapter 3, FBG sensor has been calibrated. This included the use of a customized heating system. The FBG sensor has then been characterized and the Bragg peak has been detected during the calibration experiments. The thermal sensitivity of the FBG sensor has determined and compared to the simulated one. A linear relationship has been showed between the applied temperature and the measured wavelength. A thermal sensitivity of 4.7 pm/°C has been obtained with the FBG sensor. The simulated temperatures using TMM method and the measured temperatures have been compared. These experimental results showed a good agreement the simulated one. It has been observed that the maximum positive temperature measurement error was of $\sim$ 0.019 °C at 50 °C for this sensor. A good linearity of the FBG sensor has been demonstrated for temperature measurements.

In chapter 4, an academic rotating machine has been developed. The FBG sensor has been integrated into this machine successfully. In this way the dynamical temperature measurements of the rotor have been interrogated. The measurements of the temperature with our FBG have been performed and showed that the sensor was able to follow the temperature variation during the heating of the rotor. The wavelength has been shifted depending on the temperature variations. The study of the sensing characteristics has showed a maximum error of 0.024 °C over a temperature range of [20 °C - 70 °C]. We have measured the temperature in the rotating machine for different rotating velocities up to a maximum rotating velocity of 860 rpm. In the electric power industry, uncertainties below 10 °C are acceptable.

It is the first time to our knowledge that FBG sensor was used to measure dynamical temperature variations inside a rotating machine at 843 nm.

The determination of heat spots in the rotor during its rotation has been investigated. This method is a compact solution that requires one interrogation unit in contrary to many bulky sensors. In this study, the main focus was on temperature measurements. However, this technique is also valid for measurement of other parameters such as strain, torque, vibration. This method is able to measure temperature while the sensor is integrated into the rotating parts of the electrical machine at different speed of rotation, without using a rotary joint. This method can be applied to different types of rotating machines.

While this thesis focuses only on the feasibility of a new non-contact temperature sensing technique with a single sensor, a multiplexing system (many gratings at different central wavelengths) would be useful in order to make a thermal mapping of the rotor. A point temperature measurement corresponds to the position of a Bragg grating, for this, positions of Bragg gratings on the rotor should be known priori to allow an accurate mapping of rotor temperatures. We believe that it is interesting to further explore the possibility of using multiplexed FBGs for determining the temperature at different points inside the rotor. The concept of using an FBG inside the rotating part of the machine could still be promising for determining the temperature of the rotor or other parameters.

In this way, the inscription of gratings is possible along the entire fiber (not only one point) and the FBGs embedded in rotating machine could determine important parameter inside the machine. We believe that it would be valuable to have a look at several gratings integrated in one optical fiber and by using a detection method such as photodiodes with

filters. A proposition of the detection technique could be the use of an edge filtering technique.

As future work, measuring wavelength shifts for several FBGs integrated into a small power rotating machine (kW) suitable for automotive applications should be investigated. Temperature variations up to 150°C could be detected while rotating the FBGs for 1500 RPM.

An interesting future prospect is embedding FBGs into a real rotor of an electrical machine fabricated in the electrical power industry. It would be interesting to investigate if an FBG can be embedded in this machine for doing temperature, strain and vibration measurements and if it can measure or even predict damage in this rotating at the anticipated locations.

The biggest challenge will be developing a simple technique or interrogation scheme that is able to measure, accurately, small wavelength shifts over a wide range. Moreover, implementing this technique out of the laboratory environment in structure located in harsh environment such as electrical machines.

In addition, embedding and multiplexing FBGs within a fiber in the electrical machine structure will lead to further advantages. In fact, this sensor needs to be embedded in the machine during manufacture and an instrumentation scheme should be planned. One should be able to determine the suitable instrumentation of FBG sensors on rotors, their installation procedure and their optimal locations in order to detect anomalous machine operation.

APPENDIX A

List of publications

The work presented in this thesis has been published and presented in the following book and international conferences.

- Abboud R., Al Hajjar H., Ospina A., Chaaya J.A., Zaatar Y., Lamarque F. (2020) Local Temperature Monitoring Method of a Rotor Using Near-Infrared Fiber Bragg Grating. In: Bhattacharya I., Otani Y., Lutz P., Cherukulappurath S. (eds) Progress in Optomechatronics. Springer Proceedings in Physics, vol 249. Springer, Singapore.

- Rita Abboud, Hani Al Hajjar, Alejandro Ospina, Jad Abou Chaaya, Youssef Zaatar, and Frédéric Lamarque "Distributed dynamical temperature measurement of the rotor of small rotating machines using Fiber Bragg Gratings (FBGs) sensors", Proc. SPIE 11739, Fiber Optic Sensors and Applications XVII, 1173908 (12 April 2021)

APPENDIX B

Spectral response of a uniform FBG

```
%% Blocks and Grating Definition
L = 1e-3; % Grating length(m)
N=500; % number of segments
dz=L/N;%BlockLength;

%% Wavelength properties
vector= zeros(1,N);
LambdaB = 840e-09 + vector; % Reflected wavelength (nm)
lambda = (836e-09:0.004e-09:844e-09);
size_lambda= size(lambda,2);
%% Parameters
Neff = 1.447; % Average refractive index
dn=(ones(1,N)*1e-3); % Refractive index difference
Lambda_n = 840e-09;

%% Parameters
v=1; % visibility assumed to be 1

k=(pi*v.*dn')./LambdaB'; %AC coupling coefficient of the
ith segment
k2=k.*k;
k2=repmat(k2,1,size_lambda);

k=repmat(k,1,size_lambda);

 for i=1:N

     beta(i,:)= 2*pi*Neff.*(1./lambda-1./LambdaB(i));
 end
beta2=beta.*beta;
gamma=sqrt(k2-beta2);

%% Transfer matrix calculation for each bloc
% Assume D =[A B ; C D]
l = gamma*dz;
D1 = cosh(l)-(1i*beta./gamma).*sinh(l);
D2 = (1i*k./gamma).*sinh(l);
```

```
D3 = conj(D2);
D4 = conj(D1);

%% Multiplication for each bloc
Y1(1,:) = D1(1,:).* D1(2,:) + D2(1,:).* D3(2,:);
Y2(1,:) = D1(1,:).* D2(2,:) + D2(1,:).* D4(2,:);
Y3(1,:) = D3(1,:).* D1(2,:) + D4(1,:).* D3(2,:);
Y4(1,:) = D3(1,:).* D2(2,:) + D4(1,:).* D4(2,:);
for i = 2 : N-1
    Y1(i,:) = Y1(i-1,:).* D1(i+1,:) + Y2(i-1,:).*
D3(i+1,:);
    Y2(i,:) = Y1(i-1,:).* D2(i+1,:) + Y2(i-1,:).*
D4(i+1,:);
    Y3(i,:) = Y3(i-1,:).* D1(i+1,:) + Y4(i-1,:).*
D3(i+1,:);
    Y4(i,:) = Y3(i-1,:).* D2(i+1,:) + Y4(i-1,:).*
D4(i+1,:);
End

%% Reflexion Calculation
 uL=1;
 vL=0;
 u0 = Y1(N-1,:)'.*uL;
 v0 = Y3(N-1,:)'.*uL;
 r = v0./u0;
 R= abs(r).^2;

    xlabel('Wavelength')
    ylabel('Reflection')
```

FBG spectral response under thermal effect

```
%% Blocks and Grating Definition
L = 1e-3; % Grating length(m)
N=500; % number of segments
dz=L/N;%BlockLength;
%% Wavelength properties
vector= zeros(1,N);
LambdaB = 840e-09 +vector ;%  Reflected wavelength (nm)
bw = 100e-09;
lambda = (836e-09:0.004e-09:844e-09);
size_lambda= size(lambda,2);
%% Parameters
Neff = 1.447; % Average refractive index
dn=(ones(1,N)*1e-3); % Refractive index difference

Lambda_n = 840e-09;
%% Temperature
deltaT = 293.15;
m=0;

dn_dT = 8.6e-6;% thermo-optical coefficient (1/k)
alpha= 4.1e-7;%coefficient of thermal expansion (1/k)
a=11.513; % absorption coefficient (m)

%% Parameters
v=1; % visibility assumed to be 1
for  deltaT = 293.15:10:343.15 %% Temperature

    k=(pi*(1+dn_dT*deltaT)*dn')./LambdaB'; %AC coupling
coefficient of the ith segment k=pi*DN./lambda;
k2=k.*k;
k2=repmat(k2,1,size_lambda);

k=repmat(k,1,size_lambda);

 for i=1:N
     beta(i,:)= ((2*pi*(Neff+dn_dT*deltaT))./lambda)-
(2*pi*Neff)./((1+alpha*deltaT).*LambdaB(i))+1i*(a/2);
%DeltaBetaconstantedecouplage

end
beta2=beta.*beta;
gamma=sqrt(k2-beta2);
```

```
%% Transfer matrix calculation for each bloc
% Assume D =[A B ; C D]
l=gamma*dz;
D1 = cosh(l)-(1i*beta./gamma).*sinh(l); %D11=
cos(gamma*dz)-1i*sin(gamma*dz);
D2 = (1i*k./gamma).*sinh(l);%D12 =
1i*k*dz.*sinc(gamma*dz);
D3 = conj(D2);
D4 = conj(D1);

Y1(1,:) = D1(1,:).* D1(2,:) + D2(1,:).* D3(2,:);
Y2(1,:) = D1(1,:).* D2(2,:) + D2(1,:).* D4(2,:);
Y3(1,:) = D3(1,:).* D1(2,:) + D4(1,:).* D3(2,:);
Y4(1,:) = D3(1,:).* D2(2,:) + D4(1,:).* D4(2,:);
for i = 2 : N-1
    Y1(i,:) = Y1(i-1,:).* D1(i+1,:) + Y2(i-1,:).*
D3(i+1,:);
    Y2(i,:) = Y1(i-1,:).* D2(i+1,:) + Y2(i-1,:).*
D4(i+1,:);
    Y3(i,:) = Y3(i-1,:).* D1(i+1,:) + Y4(i-1,:).*
D3(i+1,:);
    Y4(i,:) = Y3(i-1,:).* D2(i+1,:) + Y4(i-1,:).*
D4(i+1,:);
end
%% Reflexion Calculation
 uL=1;
 vL=0;
 u0 = Y1(N-1,:)'.*uL;
 v0 = Y3(N-1,:)'.*uL;
 r= v0./u0;
 R3= abs(r).^2;
%% Figure
    R = max(R3);
    plot(lambda,R3)
    hold on
    xlabel('Wavelength (m)')
    ylabel('Reflection')

end
```

REFERENCES

[1] "Energy and climate change — European Environment Agency." [Online]. Available: https://www.eea.europa.eu/signals/signals-2017/articles/energy-and-climate-change. [Accessed: 16-Aug-2021].

[2] OECD/IEA, "Energy efficiency policy opportunities for electric motor driven systems executive summary The global assessment," 2011.

[3] K. T. V. Grattan and T. Sun, "Fiber optic sensor technology: An overview," *Sensors Actuators, A Phys.*, 2000.

[4] Y. Wang, L. H. Negri, H. J. Kalinowski, D. S. Mattos, G. H. Negri, and A. S. Paterno, "Hardware embedded fiber sensor interrogation system using intensive digital signal processing," *J. Microwaves, Optoelectron. Electromagn. Appl.*, vol. 13, no. 2, pp. AoP29-Aop43, 2014.

[5] P. Abbott, " Optical Fiber Sensors. Applications, Analysis and Future Trends. Volume Four982Brian Culshaw Edited by, John Dakin Edited by. Optical Fiber Sensors. Applications, Analysis and Future Trends. Volume Four . Artech House, 1997. 478 pp, ISBN: 0-89006-940-9 £," *Sens. Rev.*, 1998.

[6] J. M. López-Higuera, L. R. Cobo, A. Q. Incera, and A. Cobo, "Fiber optic sensors in structural health monitoring," *J. Light. Technol.*, vol. 29, no. 4, pp. 587–608, 2011.

[7] R. Correia, S. James, S. W. Lee, S. P. Morgan, and S. Korposh, "Biomedical application of optical fibre sensors," *J. Opt. (United Kingdom)*, vol. 20, no. 7, 2018.

[8] K. de Morais Sousa, W. Probst, F. Bortolotti, C. Martelli, and J. C. C. da Silva, "Fiber bragg grating temperature sensors in a 6.5-MW generator exciter bridge and the development and simulation of its thermal model," *Sensors (Switzerland)*, vol. 14, no. 9, pp. 16651–16663, 2014.

[9] L. K. Cheng *et al.*, "Fiber Bragg grating sensors for structural health monitoring of Tsing Ma bridge: Background and experimental observation," *Eng. Struct.*, vol. 28, no. 5, pp. 648–659, 2005.

[10] “11 - Fiber Optic Sensors for Biomedical Applications | Elsevier Enhanced Reader.” [Online]. Available: https://reader.elsevier.com/reader/sd/pii/B9780128031315000118?token=348B87B27A3661ACC2C1CA896B6C0210E17FA721553AB3D3E318D650E3EA0480DF14484EFC636B94FFA79E2F09D54F04&originRegion=eu-west-1&originCreation=20210808174423. [Accessed: 08-Aug-2021].

[11] “Fiber Optic Sensor Systems — Proximion.” [Online]. Available: https://www.proximion.com/fiber-optic-sensor-systems. [Accessed: 08-Aug-2021].

[12] “Optical Fiber vs Copper Cable. Who is the clear winner for telecom communications?” [Online]. Available: https://meroli.web.cern.ch/lecture_fibre_vs_copper.html. [Accessed: 08-Aug-2021].

[13] Y. R. García, J. Jes´, J. M. Corres, and J. Goicoechea, “Vibration Detection Using Optical Fiber Sensors,” *J. Sensors*, vol. 2010, p. 12, 2010.

[14] D. Tosi, C. Molardi, W. Blanc, C. Marques, and S. Sales, “OSA Optical Sensors and Sensing Congress,” 2019.

[15] “Chapter 16 - Functional thin films and nanostructures for sensors | Elsevier Enhanced Reader.” [Online]. Available: https://reader.elsevier.com/reader/sd/pii/B9780323512558000161?token=0C34A65B2638C7841AD250F2C443B6903092ED1A1385886522C91329227CEF92EB7DAA195AFC19E6F0209E5CB5D9F0FB&originRegion=eu-west-1&originCreation=20210808180243. [Accessed: 08-Aug-2021].

[16] “What is Bimetallic Thermometer? - Definition, Working, Construction, Spiral & Helix Strip Thermometer - Circuit Globe.” [Online]. Available: https://circuitglobe.com/bimetallic-thermometer.html. [Accessed: 09-Aug-2021].

[17] “Bimetallic Thermometer - Inst Tools.” [Online]. Available: https://instrumentationtools.com/bimetallic-thermometer/. [Accessed: 08-Aug-2021].

[18] “PPT - Sensor: Infrared Thermometer.” [Online]. Available: https://www.ckkadsp.com/ProductDetail.aspx?iid=17303239&pr=35.99. [Accessed:

08-Aug-2021].

[19] Raytek, “The Principles of Noncontact Temperature Measurement Infrared Theory.”

[20] “Infrared Temperature Sensor: what is it and how does it work?” [Online]. Available: https://www.sensortips.com/temperature/infrared-temperature-sensor/. [Accessed: 08-Aug-2021].

[21] O. GmbH, “Innovative Infrared Technology Innovated Infrared technology Basic Principles Of Non-Contact Temperature Measurement Innovative Infrared Technology.”

[22] “Boilers - Google Books.” [Online]. Available: https://www.google.fr/books/edition/Boilers/ELgp4ctCzXkC?hl=en&gbpv=1&dq=pyrometer+working+principle&pg=PA257&printsec=frontcover. [Accessed: 15-Aug-2021].

[23] “Optical resolution.” [Online]. Available: https://www.optris.co.uk/optical-resolution. [Accessed: 08-Aug-2021].

[24] “Applications | Sensortherm GmbH.” [Online]. Available: https://www.sensortherm.de/en/applications. [Accessed: 15-Aug-2021].

[25] R. Gade and T. B. Moeslund, “Thermal cameras and applications: a survey,” *Mach. Vis. Appl.*, vol. 25, pp. 245–262, 2014.

[26] “IEEE Xplore Full-Text PDF:” [Online]. Available: https://ieeexplore.ieee.org/stamp/stamp.jsp?tp=&arnumber=8341361. [Accessed: 15-Dec-2021].

[27] “Infrared guide to electrical troubleshooting, and R&D.” [Online]. Available: https://www.windpowerengineering.com/infrared-guide-electrical-troubleshooting-rd/. [Accessed: 08-Aug-2021].

[28] C. Fu *et al.*, “Design and Implementation of 2.45 GHz Passive SAW Temperature Sensors with BPSK Coded RFID Configuration,” 2017.

[29] “IEEE Xplore Full-Text PDF:” [Online]. Available: https://ieeexplore.ieee.org/stamp/stamp.jsp?tp=&arnumber=717961. [Accessed: 15-Aug-2021].

[30] “AlN/6H-SiC SAW resonator for high temperature wireless SAW sensor | Semantic Scholar.” [Online]. Available: https://www.semanticscholar.org/paper/AlN%2F6H-SiC-SAW-resonator-for-high-temperature-SAW-Wang-Ruan/bb2aa14a6453ca81abf87524d675ad729f22d940. [Accessed: 08-Aug-2021].

[31] “Resistance Temperature Detector (RTD): Construction, Working Principle, Types And Advantages - Sensors And Transducers - Teachics.” [Online]. Available: https://teachics.org/sensors-and-transducers/resistance-temperature-detector-rtd-working/. [Accessed: 08-Aug-2021].

[32] A. S. Morris, “Measurement and Instrumentation Principles,” *Meas. Sci. Technol.*, 2001.

[33] “Basics of Resistance Temperature Detectors (RTDs) ~ Learning Instrumentation And Control Engineering.” [Online]. Available: https://www.instrumentationtoolbox.com/2011/01/sensors-used-in-industrial_23.html. [Accessed: 08-Aug-2021].

[34] “Pt100 temperature sensor – useful things to know.” [Online]. Available: https://blog.beamex.com/pt100-temperature-sensor. [Accessed: 23-Aug-2021].

[35] “Temperature Sensor Types for Temperature Measurement.” [Online]. Available: https://www.electronics-tutorials.ws/io/io_3.html. [Accessed: 08-Aug-2021].

[36] E. Andrich, “PTC thermistors as self-regulating heating elements.”

[37] “Types of Thermistors differences, NTC vs PTC thermistors.” [Online]. Available: https://enercorp.com/types-of-thermistors/. [Accessed: 08-Aug-2021].

[38] “Capgo - Semiconductor Temperature Sensors.” [Online]. Available: https://www.capgo.com/Resources/Temperature/Semiconductor/Semi.html. [Accessed: 08-Aug-2021].

[39] “Semiconductor Temperature Sensors | Chipkin Automation Systems.” [Online]. Available: http://www.chipkin.com/semiconductor-temperature-sensors/. [Accessed: 08-Aug-2021].

[40] “The Seven Basic Types of Temperature Sensors | Roads & Bridges.” [Online]. Available: https://www.roadsbridges.com/seven-basic-types-temperature-sensors. [Accessed:

15-Aug-2021].

[41] P. Horowitz, W. Hill, and V. Elings, “ The Art of Electronics ,” *Phys. Today*, 1981.

[42] “How Do Thermocouples Work? Working Principles Of Thermocouples.” [Online]. Available: https://www.omega.com/en-us/resources/how-thermocouples-work. [Accessed: 08-Aug-2021].

[43] “Thermocouples and How to Test Them – Johnstone Supply Support.” [Online]. Available: https://johnstone.zendesk.com/hc/en-us/articles/360020068334-Thermocouples-and-How-to-Test-Them. [Accessed: 08-Aug-2021].

[44] D. Marcuse, “Loss Analysis of Single-Mode Fiber Splices,” *Bell Syst. Tech. J.*, 1977.

[45] P. K. Sekhar and V. Uwizeye, “Review of sensor and actuator mechanisms for bioMEMS,” *MEMS Biomed. Appl.*, pp. 46–77, Jan. 2012.

[46] L. Cognolato, “Chemical Vapour Deposition for Optical Fibre Technology,” *J. Phys. IV Proc.*, vol. 11, no. C5, p. 5, 1995.

[47] “FOCS-Fiber-Optic Current Sensor Make light work of DC current measurement.”

[48] K. O. Hill, Y. Fujii, D. C. Johnson, and B. S. Kawasaki, “Photosensitivity in optical fiber waveguides: Application to reflection filter fabrication,” *Appl. Phys. Lett.*, 1978.

[49] I.-L. Bundalo, K. Nielsen, C. Markos, and O. Bang, “Bragg grating writing in PMMA microstructured polymer optical fibers in less than 7 minutes,” *Opt. Express*, 2014.

[50] O. V. Ivanov, “Near-field effects in fabrication of fiber Bragg gratings using phase masks,” *Opt. Commun.*, 2004.

[51] K. O. Hill and G. Meltz, “Fiber Bragg grating technology fundamentals and overview,” *J. Light. Technol.*, 1997.

[52] J. Canning, “Fibre gratings and devices for sensors and laser,” *Laser and Photonics Reviews*. 2008.

[53] C. Chojetzki, E. Lindner, H. Bartelt, M. Rothhardt, and M. Becker, “Fabrication and applications of Draw Tower Gratings,” *Photonics Fiber Technol. 2016 (ACOFT, BGPP,*

NP) (2016), Pap. BTh1B.1, p. BTh1B.1, Sep. 2016.

[54] G. D. Marshall *et al.*, “Point-by-point written fiber-Bragg gratings and their application in complex grating designs References and Links,” 2010.

[55] “FBGS - Draw Tower Gratings in low bend loss fiber.” [Online]. Available: https://fbgs.com/components/draw-tower-gratings-dtgs/. [Accessed: 31-Mar-2020].

[56] A. Othonos, K. Kalli, D. Pureur, and A. Mugnier, “5 Fibre Bragg Gratings.”

[57] “IEEE Xplore Full-Text PDF:” [Online]. Available: https://ieeexplore.ieee.org/stamp/stamp.jsp?tp=&arnumber=8539990. [Accessed: 19-Aug-2021].

[58] A. Martinez, M. Dubov, I. Khrushchev, and I. Bennion, “Direct writing of fibre Bragg gratings by femtosecond laser,” *Electron. Lett.*, 2004.

[59] A. Stefani, M. Stecher, G. E. Town, and O. Bang, “Direct writing of fiber bragg grating in microstructured polymer optical fiber,” *IEEE Photonics Technol. Lett.*, 2012.

[60] “(8) (PDF) Analysis of Different Writing Techniques for Chirped Fibre Bragg Gratings.” [Online]. Available: https://www.researchgate.net/publication/254963574_Analysis_of_Different_Writing_Techniques_for_Chirped_Fibre_Bragg_Gratings. [Accessed: 09-Aug-2021].

[61] D. Tosi, “Review of Chirped Fiber Bragg Grating (CFBG) Fiber-Optic Sensors and Their Applications.”

[62] X. Dong, H. Zhang, B. Liu, and Y. Miao, “Photonic Sensors Review Tilted Fiber Bragg Gratings: Principle and Sensing Applications,” *Photonic Sensors*, vol. 1, no. 1, pp. 6–30, 2011.

[63] H. Patrick and S. L. Gilbert, “Growth of Bragg gratings produced by continuous-wave ultraviolet light in optical fiber,” *Opt. Lett.*, 1993.

[64] Y. Liu, J. A. R. Williams, L. Zhang, and I. Bennion, “Abnormal spectral evolution of fiber Bragg gratings in hydrogenated fibers,” *Opt. Lett.*, 2002.

[65] J. L. Archambault, L. Reekie, and P. S. T. J. Russell, “High reflectivity and narrow

bandwidth fibre gratings written by single excimer pulse," *Electron. Lett.*, 1993.

[66] I. Riant and F. Haller, "Study of the photosensitivity at 193 nm and comparison with photosensitivity at 240 nm influence of fiber tension: Type IIa aging," *J. Light. Technol.*, 1997.

[67] D. J. Webb, "Fibre Bragg grating sensors in polymer optical fibres," *Meas. Sci. Technol.*, vol. 26, no. 9, p. 92004, 2015.

[68] E. Udd and W. B. Spillman, *Fiber Optic Sensors: An Introduction for Engineers and Scientists: Second Edition*. 2011.

[69] J. U. Kang, *Fiber optic sensing and imaging*. 2014.

[70] T. Analysis, "Fiber Bragg Gratings Sensors for Aircraft Wing Shape Measurement : Recent Applications and Technical Analysis," 2018.

[71] "Superconducting Rotating Machines."

[72] T. Burress, "Electrical Performance, Reliability Analysis, and Characterization," 2017.

[73] M. Olszewski and S. A. Rogers, "EVALUATION OF THE 2010 TOYOTA PRIUS HYBRID SYNERGY DRIVE SYSTEM Oak Ridge National Laboratory Energy Efficiency and Renewable Energy FreedomCAR and Vehicle Technologies Vehicle Systems Team," 2011.

[74] S. Selmaˇ, S. Selmačorovi´c, and D. Miljavec, "Modal Analysis and Rotor-Dynamics of an Interior Permanent Magnet Synchronous Motor: An Experimental and Theoretical Study."

[75] G. C. Stone, "Condition Monitoring and Diagnostics of Motor and Stator Windings-A Review," *IEEE Trans. Dielectr. Electr. Insul.*, vol. 20, no. 6, 2013.

[76] "IEEE Xplore Full-Text PDF:" [Online]. Available: https://ieeexplore.ieee.org/stamp/stamp.jsp?tp=&arnumber=8580539. [Accessed: 13-Aug-2021].

[77] A. Miyazaki *et al.*, "Long-distance 275-kV GIL monitoring system using fiber-optic technology," *IEEE Trans. Power Deliv.*, 2003.

[78] A. A. Boiarski, G. Pilate, T. Fink, and N. Nilsson, “Temperature Measurements in Power Plant Equipment Using Distributed Fiber Optic Sensing,” *IEEE Trans. Power Deliv.*, 1995.

[79] B. J. Chalmers, “Book Review: Electric Motor Handbook,” *Int. J. Electr. Eng. Educ.*, 1979.

[80] A. Rogers, “Distributed optical-fibre sensing,” *Measurement Science and Technology*. 1999.

[81] “IEEE Xplore Full-Text PDF:” [Online]. Available: https://ieeexplore.ieee.org/stamp/stamp.jsp?tp=&arnumber=5778980. [Accessed: 10-Aug-2021].

[82] S. E. Zocholl, “Motor analysis and thermal protection,” *IEEE Trans. Power Deliv.*, 1990.

[83] P. Milanfar and J. H. Lang, “Monitoring the thermal condition of permanent-magnet synchronous motors,” *IEEE Trans. Aerosp. Electron. Syst.*, 1996.

[84] P. H. Mellor, D. Roberts, and D. R. Turner, “Lumped parameter thermal model for electrical machines of TEFC design,” *IEE Proc. B Electr. Power Appl.*, 1991.

[85] M. Gottlieb and G. B. Brandt, “HOT SPOT DETECTION IN GENERATORS WITH OPTICAL FIBERS.,” in *American Society of Mechanical Engineers (Paper)*, 1981.

[86] M. Gottlieb and G. B. Brandt, “HOT SPOT DETECTION IN TURBINE-GENERATORS WITH OPTICAL FIBERS.,” in *Electric Power Research Institute, Coal Combustion Systems Division, (Report) EPRI CS*, 1983.

[87] C. P. Lawson and P. C. Ivey, “Tubomachinery blade vibration amplitude measurement through tip timing with capacitance tip clearance probes,” *Sensors Actuators A Phys.*, 2005.

[88] “HELL ON WHEELS.”

[89] M. Fabian, D. M. Hind, C. Gerada, T. Sun, and K. T. V. Grattan, “Comprehensive Monitoring of Electrical Machine Parameters Using an Integrated Fiber Bragg Grating-Based Sensor System,” *J. Light. Technol.*, vol. 36, no. 4, pp. 1046–1051, 2018.

[90] “IEEE Xplore Full-Text PDF:” [Online]. Available: https://ieeexplore.ieee.org/stamp/stamp.jsp?tp=&arnumber=9829. [Accessed: 06-

Sep-2021].

[91] L. Mannik, S. K. Brown, and S. R. Campbell, “Phosphor-based thermometry of rotating surfaces,” *Appl. Opt. Vol. 26, Issue 18, pp. 4014-4017*, vol. 26, no. 18, pp. 4014–4017, Sep. 1987.

[92] D. A. Staton and A. Cavagnino, “Convection heat transfer and flow calculations suitable for electric machines thermal models,” *IEEE Trans. Ind. Electron.*, 2008.

[93] C. Hudon, C. Guddemi, S. Gingras, R. C. Leite, and L. Mydlarski, “Rotor temperature monitoring using fiber Bragg gratings,” in *IEEE Electrical Insulation Conference (EIC), 2016*, 2016, pp. 456–459.

[94] M. M. Werneck, R. C. da S. B. Allil, and B. A. Ribeiro, “Calibration and operation of a fibre Bragg grating temperature sensing system in a grid-connected hydrogenerator,” *IET Sci. Meas. Technol.*, vol. 7, no. 1, pp. 59–68, 2013.

[95] R. C. Leite *et al.*, “Analysis of thermo-mechanical stress in fiber bragg grating used for hydro-generator rotor temperature monitoring,” *J. Microwaves, Optoelectron. Electromagn. Appl.*, vol. 16, no. 2, pp. 445–459, 2017.

[96] D. Hind *et al.*, “Use of optical fibres for multi-parameter monitoring in electrical AC machines,” in *Diagnostics for Electrical Machines, Power Electronics and Drives (SDEMPED), 2017 IEEE 11th International Symposium on*, 2017, pp. 208–212.

[97] H. E. Meissner and D. P. Shepherd, “W TmYAG,” vol. 37, no. 14, pp. 898–899, 2001.

[98] A. D. Kersey, T. A. Berkoff, and W. W. Morey, “R 1.128 1.014,” vol. 28, no. 3, pp. 236–238, 1992.

[99] M. A. Davis and A. D. Kersey, “All-fibre Bragg grating strain-sensor demodulation technique using a wavelength division coupler,” *Electron. Lett.*, vol. 30, no. 1, pp. 75–77, 1994.

[100] S. Chung, J. Kim, B.-A. Yu, and B. Lee, “A fiber Bragg grating sensor demodulation technique using a polarization maintaining fiber loop mirror,” *IEEE Photonics Technol. Lett.*, vol. 13, no. 12, pp. 1343–1345, 2001.

[101] F. M. Araujo, L. A. Ferreira, J. L. Santos, and F. Farahi, “Demodulation scheme for fiber

Bragg grating sensors based on active control of the spectral response of a wavelength division multiplexer," *Appl. Opt.*, vol. 37, no. 34, pp. 7940–7946, 1998.

[102] S. C. Kang, S. Y. Kim, S. B. Lee, S. W. Kwon, S. S. Choi, and B. Lee, "Temperature-independent strain sensor system using a tilted fiber Bragg grating demodulator," *IEEE Photonics Technol. Lett.*, vol. 10, no. 10, pp. 1461–1463, 1998.

[103] M. A. Davis and A. D. Kersey, "Matched-filter interrogation technique for fibre Bragg grating arrays," *Electron. Lett.*, vol. 31, no. 10, pp. 822–823, 1995.

[104] D. Zhao, X. Shu, L. Zhang, and I. Bennion, "Sensor interrogation technique using chirped fibre grating based Sagnac loop," *Electron. Lett.*, vol. 38, no. 7, p. 1, 2002.

[105] A. D. Kersey, T. A. Berkoff, and W. W. Morey, "High-resolution fibre-grating based strain sensor with interferometric wavelength-shift detection," *Electron. Lett.*, vol. 28, no. 3, pp. 236–238, 1992.

[106] T. A. Berkoff and A. D. Kersey, "Fiber Bragg grating array sensor system using a bandpass wavelength division multiplexer and interferometric detection," *IEEE photonics Technol. Lett.*, vol. 8, no. 11, pp. 1522–1524, 1996.

[107] "Spectrometers, monochrometers and spectrographs." [Online]. Available: https://www.horiba.com/en_en/technology/spectroscopy/spectrometers-and-monochromators/spectrometer-monochromator/. [Accessed: 19-Aug-2021].

[108] V. Saptari, *Fourier-Transform Spectroscopy Instrumentation Engineering*. 2009.

[109] W. David, *Spectroscopy*. .

[110] P. Lecoy, "Les fibres optiques en capteurs et en instrumentation," *La Rev. 3E. I*, no. 85, 2016.

[111] M. M. Werneck, R. C. S. B. Allil, B. A. Ribeiro, and F. V. B. de Nazaré, "A guide to fiber Bragg grating sensors," in *Current Trends in Short-and Long-period Fiber Gratings*, InTech, 2013.

[112] A. Bertholds and R. Dändliker, "Deterination of the Individual Strain-Optic Coefficients in Single-mode Optical Fibers," *J. Light. Technol.*, 1988.

[113] Z. Xiong, G. D. Peng, B. Wu, and P. L. Chu, “Highly tunable Bragg gratings in single-mode polymer optical fibers,” *IEEE Photonics Technol. Lett.*, vol. 11, no. 3, pp. 352–354, 1999.

[114] W. Zhang and D. J. Webb, “Humidity responsivity of poly (methyl methacrylate)-based optical fiber Bragg grating sensors,” *Opt. Lett.*, vol. 39, no. 10, pp. 3026–3029, 2014.

[115] E. M. J. Weber, A. V Dotsenko, L. B. Glebov, and V. A. Tsekhomsky, *HANDBOOK OF OPTICAL Laser and Optical Science and Technology Series Physics and Chemistry of Photochromic Glasses*. .

[116] The Engineering Toolbox, “Coefficients of Linear Thermal Expansion,” *The Engineering Toolbox*, 2015. [Online]. Available: https://www.engineeringtoolbox.com/linear-expansion-coefficients-d_95.html. [Accessed: 09-Mar-2019].

[117] L. P. M. A. v. E. M. Large G. W. Barton, “Microstructured Polymer Optical Fiber,” *Springer Sci.*, 2008.

[118] L. A. Weller-Brophy and D. G. Hall, “Analysis of waveguide gratings: application of Rouard’s method,” *J. Opt. Soc. Am. A*, vol. 2, no. 6, p. 863, Jun. 1985.

[119] L. Poladian, “Variational technique for nonuniform gratings and distributed-feedback lasers,” *J. Opt. Soc. Am. A*, vol. 11, no. 6, p. 1846, 2008.

[120] K. A. Winick, “Effective-index method and coupled-mode theory for almost-periodic waveguide gratings: a comparison,” 1992.

[121] H. Kogelnik and C. V. Shank, “Coupled-Wave Theory of Distributed Feedback Lasers,” *J. Appl. Phys.*, vol. 43, no. 5, pp. 2327–2335, May 1972.

[122] M. Matsuhara and A. Watanabe, “B=-(643+6d),” vol. 65, no. July, 1975.

[123] S. Udoh, J. Njuguma, and R. Prabhu, “Modelling and simulation of fiber Bragg grating characterization for oil and gas sensing applications,” *First Int. Conf. Syst. Informatics, Model. Simul.*, pp. 213–218, 2014.

[124] P. Lecoy, “Les fibres optiques en capteurs et en instrumentation,” *La Rev. 3EI*, vol. 85, 2016.

[125] C. R. Giles, “Lightwave applications of fiber bragg gratings,” *J. Light. Technol.*, 1997.

[126] M. Yamada and K. Sakuda, “Analysis of almost-periodic distributed feedback slab waveguides via a fundamental matrix approach,” *Appl. Opt.*, 2009.

[127] K. Peters, M. Studer, J. Botsis, A. Iocco, H. Limberger, and R. Salathé, “Embeded optical fiber bragg grating sensor in a nonuniform strain field: Measurements and simulations,” *Exp. Mech.*, 2001.

[128] H. Y. Ling, K. T. Lau, W. Jin, and K. C. Chan, “Characterization of dynamic strain measurement using reflection spectrum from a fiber Bragg grating,” *Opt. Commun.*, 2007.

[129] Y. Chen, J. Li, Y. Yang, M. Chen, J. Li, and H. Luo, “Numerical modeling and design of mid-infrared FBG with high reflectivity,” *Optik (Stuttg).*, 2013.

[130] A. Ikhlef, R. Hedara, and M. Chikh-Bled, “Uniform Fiber Bragg Grating modeling and simulation used matrix transfer method,” *IJCSI Int. J. Comput. Sci. Issues*, 2012.

[131] R. J. Espejo and S. D. Dyer, “Transverse-Stress Fiber Bragg Grating Sensor With High Spatial Resolution and Temperature Stability,” vol. 25, no. 7, pp. 1777–1785, 2007.

[132] DANIELLE COLLINS, “What does motor insulation class specify and why is it important?” [Online]. Available: https://www.motioncontroltips.com/what-does-motor-insulation-class-specify-and-why-is-it-important/. [Accessed: 16-Jul-2021].

[133] Steve Mazziotta, “Electric Motor Insulation Class - What is It?” [Online]. Available: https://www.hecoinc.com/blog/electric-motor-insulation-class-what-is-it. [Accessed: 16-Jul-2021].

[134] G. BR, “Electric motor insulation class: learn more - Geartech Br.” [Online]. Available: https://geartechbr.com.br/en/electric-motor-insulation-class-learn-more/. [Accessed: 16-Jul-2021].